Hydrogen-Bonding Liquids at Mineral Surfaces: From Fundamentals to Applications

ANH THI VAN PHAN

A dissertation submitted in partial fulfilment of the requirements for the degree of

Doctor of Philosophy

of the

University College London

Department of Chemical Engineering

UCL

Primary Supervisor

Prof. Alberto Striolo

January 2016

Declaration

I, Anh Thi Van Phan confirm that the work presented in this thesis is my own. Where information has been derived from other sources, I confirm that this has been indicated in the thesis.

Abstract

Molecular-level understanding of properties of hydrogen-bonding liquids and their mixtures at solid-liquid interfaces plays a significant role in several applications including membrane-based separations, shale gas production, etc. Liquid water and ethanol are common hydrogen-bonding fluids. All-atom equilibrium molecular dynamics simulations were employed to gain insights regarding the structure and dynamics of these hydrogen-bonding liquids on various free-standing solid surfaces. Models for silica, alumina, and magnesium oxide were used in these works. The results show a highly well-ordered layer of the hydrogen-bonding liquids near solid substrates and a pronounced dipolar orientation of the hydrogen-bonding molecules found in this layer, which is dependent on the surface chemistry of the substrate. Our simulated results are in good agreement with the experimental data. Many studies have paid attention to mixtures of hydrogen-bonding fluids such as liquid water-ethanol mixtures due to their critical roles in industrial applications. We have conducted simulations to examine the sorptivity, structure and dynamics of liquid water-ethanol mixtures confined in alumina pores. Analysis of the structure and dynamics suggests the possibility of using alumina as perm-selective membranes to produce anhydrous ethanol from liquid water-ethanol solutions. In addition, it is important to understand properties of mixtures of water and volatile hydrocarbons under confinement as recently water is used as fracturing-fluid to stimulate subsurface formations in the practice of hydraulic fracturing. We have investigated the behaviour of aqueous methane confined in 1 nm-wide pores obtained from materials such as silica, alumina, and magnesium oxide. Our results show that methane solubility in confined water strongly depends on the confining material, with silica yielding the highest solubility. Studying dynamical properties of confined

aqueous methane suggests a direct proportional coupling between methane and water dynamics. These results help refer to multiple possible applications for fluid transport.

Contents

Contents 5

Chapter 1 Introduction 10

Chapter 2 Simulation Methodology 15

2.1 Molecular Dynamics Simulations 15

2.1.1 Introduction 15

2.1.2 Atomic Force Fields 15

2.1.3 Algorithms 17

2.1.4 Force Calculation and Long-Range Interactions 19

2.1.5 Periodic Boundary Conditions 20

2.1.6 Thermostat 20

2.2 Umbrella Sampling Technique 21

Chapter 3 Molecular Structure and Dynamics in Thin Water Films at Metal Oxide Surfaces: Magnesium, Aluminum, and Silicon Oxide Surfaces 24

3.1 Abstract 24

3.2 Introduction 25

3.3 Simulation Methodology and Details 26

3.4 Results and Discussion 29

3.4.1 Contact Angle 29

3.4.2 Atomic Density Profiles 32

3.4.3 In-plane Radial Distribution Functions 36

3.4.4 Hydrogen Bond Network 38

3.4.5 In-plane Density Distributions 39

3.4.6 Residence Times and Hydrogen Bond Network 41

3.4.7 Orientation Distribution of Interfacial Water 42

3.4.8 Comparison with Other Substrates 44

3.5 Summary and Conclusions 51

Chapter 4 Liquid Ethanol Simulated on Crystalline Alpha Alumina 53

4.1 Abstract 53

4.2 Introduction 54

4.3 Simulation Methods and Algorithms 55

4.4 Results and Discussion 59

4.4.1 Atomic Density Profiles 59

4.4.2 In-plane Radial Distribution Functions 63

4.4.3 In-plane Density Distributions 65

4.4.4 Hydrogen Bond Network 67

4.4.5 Ethanol Orientation 70

4.4.6 Dynamical Properties 74

4.5 Conclusions 77

Chapter 5 Preferential Adsorption from Liquid Water-Ethanol Mixtures in Alumina Pores 79

5.1 Abstract 79

5.2 Introduction 79

5.3 Simulation Methodology 82

5.4 Results and Discussion 85

5.4.1 Liquid Mixtures in Contact with Freestanding Alumina 85

5.4.2 Liquid Mixtures in Contact with Narrow Alumina Pores 87

5.4.3 Bulk Liquid Mixtures – Dynamical Properties 104

5.5 Conclusions 105

Chapter 6 Aqueous Methane in Slit-Shaped Silica Nanopores: High Solubility and Traces of Hydrates 107

6.1 Abstract 107

6.2 Introduction 108

6.3 Methods and Algorithms 110
6.4 Results and Discussion 113
6.4.1 Methane Density Profiles 115
6.4.2 Structure of Confined Aqueous Methane 117
6.4.3 Methane Solubility 122
6.4.4 Probability of Hydrate Formation inside the Pore 125
6.5 Concluding Remarks 128
Chapter 7 Factors Governing the Behaviour of Aqueous Methane in Narrow Pores 129
7.1 Abstract 129
7.2 Introduction 129
7.3 Simulation Methodology 130
7.4 Results and Discussion 134
7.4.1 Methane Solubility 134
7.4.2 Structure of Confined Fluids - Methane and Water 137
7.4.3 Water Density Fluctuations under Confinement - Degree of Hydrophobicity 141
7.4.4 Coupling of Methane Dynamics to Hydration Fluctuations 143
7.5 Conclusions 145
Chapter 8 Summary and Outlook 147
Appendices 151
A. Supporting Information for Chapter 4 151
A.1. Force Field Parameters 151
A.2. Simulation Snapshots 151
A.3. Free Energy Landscapes 153
A.4. Structural Properties 154
A.5. Calculation Methods for Ethanol Orientation 157

B. Supporting Information for Chapter 5 157
B.1. Algorithms 157
B.2. Results 158
C. Supporting Information for Chapter 6 164
C.1. Algorithms 164
C.2. Results 168
Bibliography 171

Acknowledgements

First of all, I truly thank the Almighty God and the Lord for loving, protecting and giving me the strength to complete this study.

I would like to express my sincere thanks to my advisor Prof. Alberto Striolo for his help, guidance, encouragement, and support in the course of my PhD. His mentorship, creative thoughts, experiences and expertise in the field of my research helped me to achieve the research goals as well as grow gradually to be more confident in my abilities.

I also thank Prof. Angelos Michaelides for giving me advices as my secondary advisor and Prof. David Cole in The Ohio State University for the collaborations during my PhD study. I take this time to record my sincere thanks to my former advisor Dr. Luong Huu Nguyen, Prof. Hai Duong, and Prof. Dimitrios Papavassiliou for introducing me to Prof. Striolo so that I can have the great opportunity to study abroad and pursue the higher level education that I have never dreamed of.

Thanks to all my officemates, colleagues and friends, especially Dr. Ngoc Pham, Dr. Tuan Ho and Dr. Cuong Luu for helping me during my first years as a graduate student and Minh Vo for exchanging research ideas.

Finally, I am truly thankful to my parents, my sisters and brothers and my lovely friends who always love, encourage and support me in behind. No words can express my deepest gratitude for everything they have done for me in the course of my life. And the last one whom I truly give thanks to is my beloved SSN. If I did not meet Him, I would live an empty life without knowing its true meaning.

Chapter 1 Introduction

Much attention has been focused on hydrogen-bonding fluids and their mixtures over past decade due to their involvement in many geological, chemical and biological processes [1-8]. Liquid water is an exceptional hydrogen-bonding fluid. Interfacial water properties govern a variety of phenomena in engineered and natural systems. Understanding the behaviour of water at solid−liquid interfaces is crucial for developing and improving multiple applications, for example, ion adsorption/desorption processes on solid substrates, diffusion of ions in nanopores, biological membranes, and ion channels [1-3, 9, 10]. Particular attention was paid to the interface between liquid water and metal oxides, which is essential for various industrial and environmental processes. Many oxide surfaces receive significant research interests as their roles of catalysts or catalyst supports [11, 12]. The presence of thin water films on metal oxide surfaces somehow enhances the catalytic activities of those materials. Additionally, water – mineral oxide chemistry is considered to dictate properties of hydrodynamic and reactivity at Earth's subsurface [13-16]. Many theoretical [17-21] and experimental [21-24] efforts have been carried out to gain insight into water – metal oxide interfacial behaviour. The experimental data confirm a significant different behaviour of interfacial water compared to that of bulk water [25-29]. Catalano recently reported specular X-ray reflectivity data for the sapphire – water interface and show one dense layer of adsorbed water with density perturbations that extend for ∼1 nm into the bulk [30]. Fenn et al. investigated orientational dynamics of water at neutral and ionic interfaces using ultrafast infrared spectroscopy and reported a slower orientational relaxation of interfacial water than that found for bulk water [29]. Interpreting experimental data often requires high-level theoretical approaches. Monte Carlo and molecular dynamics (MD) simulations

techniques are considered as highly efficient tools for providing molecular-level insights into properties of interfacial water on solid surfaces. Mamontov et al. [25] investigated the properties of interfacial water on rutile using MD simulations as well as neutron scattering techniques and show that the structure and dynamics of water is governed by the chemistry of rutile substrate. Argyris et al. [17-19, 31] have intensively studied the structural and dynamical properties of interfacial water on various materials such as silica, alumina, and graphite employing MD simulation techniques. Our contribution attempts to build on recent progress in this field. In Chapter 3 we conducted MD simulations to compare the properties of interfacial water predicted on magnesium oxide when it is treated as rigid versus when its atoms are allowed to vibrate. We also compare with those reported earlier for water on alumina, and on silicon dioxide surfaces.

While numerous research efforts in the field of liquid water at solid-liquid interfaces are available [26, 29, 32-36], only a few investigations have been carried out for other hydrogen-bonding liquids, including alcohols. A variety of applications in industry, geology, petroleum, and environment employ amphiphilic molecules in contact with solid substrates [5-7]. These molecules could act as lubricants, or could dislocate other adsorbed fluids. In an attempt to document the behaviour of hydrogen-bonding and amphiphilic fluids at interfaces, in Chapter 4 we have examined the structural and dynamical properties of ethanol within thin liquid films formed on two alumina surfaces – C-plane (0001) and R-plane $(1\bar{1}02)$ terminations of the hydroxylated α-Al_2O_3 – at ambient conditions using equilibrium MD simulations. Comparing to experimental data reported by Shen et al. [37] who studied ethanol on the R-plane alumina surface using sum frequency vibrational spectroscopy, our simulation results show good agreement.

Hydrogen-bonding fluid mixtures are ubiquitous in chemistry, biology, and physics [8, 38-41]. Of particular interest is liquid water – ethanol mixture. Since ethanol has become a promising oil alternative fuel or biofuel additive to gasoline [42, 43], an increasing number of approaches toward producing anhydrous ethanol from liquid water – ethanol solutions are studied. Water that is always present in ethanol even at very small concentrations during biomass productions must be removed in order for ethanol to be a usable fuel. As a consequence, the separation of water from water – ethanol solutions becomes challenging, particularly, the production of anhydrous ethanol beyond the azeotrope because traditional distillation processes could not surpass this azeotropic point [44]. Azeotropic distillation has been proposed but still requires tremendous energy [45]. Recent alternative methods such as employing molecular sieves as membrane materials are possible for splitting water from liquid water – ethanol solutions [46]. To complement the developed membrane-based materials implemented for water – ethanol separations (e.g. zeolites 3A, silicalite crystal, polymers, etc. [47-52]), we have investigated the opportunity of using porous alumina as membrane materials for manufacturing anhydrous ethanol by analysing the preferential adsorption of liquid water – ethanol mixture confined in the C-plane (0001) hydroxylated α-Al_2O_3 pores in Chapter 5. We also studied the structure and dynamics of water – ethanol solutions under confinement and compare to those found in the bulk.

In a recently developed important application, high-pressure water is used to stimulate subsurface formations in the practice of hydraulic fracturing. In this process the rock is fractured to increase gas and oil permeation [53]. Recent investigations [54] reported the low recovery of hydraulic fracture water during well clean-up and flow back operations, suggesting that large amounts of water remain

trapped within the sub-surface formations. King [54] suggested that hydraulic fracturing water may also be trapped in micro-fractures and small pores caused by pressure release. Because water entrapment in the shale may affect the well productivity, understanding systems composed of water and volatile hydrocarbons under confinement could play a significant role in the design of hydraulic fracturing processes toward enhancing well performance and hydrocarbon recovery, and more in general could help rationalize the geochemical processes at Earth's subsurface as well as deep within the crust and mantle [55, 56], which affect technologies such as carbon sequestration [57, 58]. In addition, the association of volatile hydrocarbon in water under pertinent conditions could initiate the gas hydrate information. Inspired by the fact that a few experimental and computational efforts focused on the effect of solid surfaces or porous matrices on the gas hydrate formation [59-62], in Chapter 6 we carried out equilibrium MD simulations for methane – water mixtures confined within 1 nm slit-shaped silica pores in equilibrium with bulk methane at moderate conditions. Our aim is to not only study the significance of confinement in the behaviour of confined aqueous methane but try to answer whether hydrates can be found inside the small silica pore at modest conditions and what could induce the hydration formation in confined phase. Finally, in an effort to quantify the effect of surface chemistry and heterogeneity on the structural and dynamical properties of confined hydrocarbon fluid mixtures, in Chapter 7 we performed equilibrium MD simulations for aqueous methane confined within 1 nm slit-shaped nanopores from various materials at same conditions with the previous work reported in Chapter 6. Silica, alumina and magnesium oxide (MgO) were used as solid substrates in this work because they are fundamental components of many minerals found in the subsurface. We have investigated methane solubility in water confined in the pores,

the structural properties and the mobility of aqueous methane confined within the three pores of interest. Analysis of the methane solubility in water inside the pores suggests the large increase of methane solubility in confined water compared to that observed in the bulk water. This could help improve some technological processes including hydraulic fracturing, shale gas exploration, wastewater treatment, etc.

Chapter 2 Simulation Methodology

2.1 Molecular Dynamics Simulations

2.1.1 Introduction

Developed by Alder and Wainwright in the late 1950s and Rahman in the early 1960s [63], MD is considered as a useful approach for computer simulation of multiple-body systems modelled at the atomistic level. Atoms in systems interact via forces and potential energies, giving a picture of their motion for a period of time. The trajectories of atoms are obtained by solving numerically Newton's equations of motion. Forces between interacting atoms and potential energy are defined by atomic force fields for systems.

2.1.2 Atomic Force Fields

Atomic force field models are built with empirical potentials with a particular functional form, showing the physical and chemical properties of the systems of interest. A common force field employed in the simulation of systems of N interacting atoms is expressed in the following form:

$$U(r_1, \dots, r_N) = \sum_{bonds} \frac{a_i}{2}(l_i - l_{i0})^2 + \sum_{angles} \frac{b_i}{2}(\theta_i - \theta_{i0})^2 + \sum_{torsions} \frac{c_i}{2}[1 + \cos(n\omega_i - \gamma_i] + \sum_{atom\ pairs} 4\varepsilon_{ij}\left[\left(\frac{\sigma_{ij}}{r_{ij}}\right)^{12} - \left(\frac{\sigma_{ij}}{r_{ij}}\right)^{6}\right] + \sum_{atom\ pairs} f\frac{q_i q_j}{\varepsilon_r r_{ij}} \quad (2.1)$$

The first three terms represent the bonded interactions. The summation indices run over all the bonds, angles and torsion angles determined by the covalent structure of the system. Specifically, the first two terms describe energies of deformations of the bond length l_i and bond angle θ_i from the equilibrium values l_{i0} and θ_{i0}, respectively. The harmonic form of these terms (with force constants a_i and b_i) provides the correct chemical structure, but avoids modelling chemical changes (e.g.

bond breaking). The third term describes rotations around the chemical bond, which are expressed by periodic energy terms (with periodicity determined by n and heights of rotational barriers defined by c_i). The last two terms represent the non-bonded interactions. The fourth term illustrates the van der Waals repulsive and attractive (dispersion) interactions between atoms i and j separated by a distance r_{ij} in the form of the Lennard-Jones 12-6 potential with the diameter σ and the well depth ε. The last term is the Coulomb electrostatic potential where q_i, q_j are the partial atomic charges for atoms i and j, $f = \frac{1}{4\pi\epsilon_0}$ is Coulomb's constant with the permittivity of free space ϵ_0 and ε_r is the relative dielectric constant. The cross Lennard-Jones term between unlike species is defined by the Lorentz-Berthelot combining rules [64]: $\sigma_{ij} = \frac{\sigma_{ii} + \sigma_{ij}}{2}$ and $\varepsilon_{ij} = \sqrt{\varepsilon_{ii}\varepsilon_{jj}}$ for ideal mixtures. For non-ideal mixtures, for example, methane – water mixtures, this cross Lennard-Jones term is obtained from $\sigma_{ij} = \frac{\sigma_{ii} + \sigma_{ij}}{2}$ and $\varepsilon_{ij} = (1 - k_{ij})\sqrt{\varepsilon_{ii}\varepsilon_{jj}}$ with k_{ij} being the solid – fluid binary interaction parameter.

Based on the potential energy $U(r_1, \ldots, r_N)$ as a function of their positions $\vec{r}_i = (x_i, y_i, z_i)$, the force acting upon *i*th atom is computed by the gradient regarding to atomic displacements as shown:

$$\vec{F}_i = -\nabla_{r_i} U(r_1, \ldots, r_N) = -\left(\frac{\partial U}{\partial x_i}, \frac{\partial U}{\partial y_i}, \frac{\partial U}{\partial z_i}\right) \quad (2.2)$$

In these works, we used the CLAYFF force field [65] to describe solid substrates such as silica, alumina, and MgO; the Optimized Potential for Liquid Simulation in the United Atom form [66] to describe ethanol and methane; and finally rigid SPC/E model [67] to simulate water.

2.1.3 Algorithms

2.1.3.1 Leap-frog algorithm

Solving Newton's equations of motion for a system of N interacting atoms $\sum_j \vec{F}_{ij} = m_i \frac{d^2\vec{r}_i(t)}{dt^2}$, where $\vec{r}_i(t) = (x_i(t), y_i(t), z_i(t))$ is the position vector of *i*th atom and $\overrightarrow{F_i}$ is the force acting upon *i*th atom at time t determined by the potential energy and m_i is the mass of the atom, the position and velocity of each atom in the system is updated by a stepwise progression. To integrate the above equations of motion, the random initial positions and velocities calculated from Boltzmann distribution are needed [68].

Due to a tremendous number of atoms in the system, it is impractical to solve the equations of motion analytically. Instead, MD simulations use numerical methods to avoid this problem. Many numerical solutions for integrating the equations of motion are proposed, for example, the Verlet and leap-frog algorithm [68]. In these studies, we applied the leap-frog algorithm to solve Newton's equations of motion. This algorithm gives positions and velocities at time t in the following forms:

$$\vec{r}(t + \delta t) = \vec{r}(t) + \vec{v}(t + \tfrac{1}{2}\delta t)\delta t \qquad (2.3)$$

$$\vec{v}\left(t + \tfrac{1}{2}\delta t\right) = \vec{v}\left(t - \tfrac{1}{2}\delta t\right) + \frac{\vec{F}(t)}{m}\delta t \qquad (2.4)$$

In this algorithm, initially the velocities are calculated at time $t + 1/2\delta t$; and then they are used to calculate the positions, *r*, at time $t + \delta t$. Thus, the velocities leap over the positions, and then the positions leap over the velocities. The velocities at time *t* can be calculated approximately by equation:

$$\vec{v}(t) = \tfrac{1}{2}\left[\vec{v}\left(t + \tfrac{1}{2}\delta t\right) + \vec{v}\left(t - \tfrac{1}{2}\delta t\right)\right] \qquad (2.5)$$

2.1.3.2 Constraint algorithms

Constraints for bond lengths and angles can be imposed by using LINCS. The LINCS algorithm is capable of resetting bonds and angles to their correct values after an unconstrained update [69]. The algorithm operates in two steps (see Figure 2.1). In the first step, the real bond lengths are not set to the recommended lengths, but the projections of the new bonds on the old bonds. These projections are set to zero. In the second step, a correction is implemented for the extending of the bonds due to rotation. In order to correct for the rotation of bond, the projection of the bond on the old direction is set to $p = \sqrt{2d^2 - l^2}$ where d is the old bond length and l is the bond length after the first projection. The corrected positons are expressed as [69]:

$$\vec{\boldsymbol{r}}^{*}_{n+1} = (\boldsymbol{I} - \boldsymbol{T_n B_n})\vec{\boldsymbol{r}}_{n+1} + \boldsymbol{T_n}\vec{\boldsymbol{p}} \qquad (2.6)$$

where ($\boldsymbol{I}$ - $\boldsymbol{T_n B_n}$) is projection matrix which sets the constrained coordinates to zero, $\boldsymbol{T}$ transforms motions in the constrained coordinates into motions in Cartesian coordinates $\boldsymbol{T} = \boldsymbol{M}^{-1}\boldsymbol{B}^{T}(\boldsymbol{B}\boldsymbol{M}^{-1}\boldsymbol{B}^{T})^{-1}$, $\boldsymbol{M}$ is a diagonal matrix consisting of the masses of the particles and $\boldsymbol{B}$ is matrix containing the directions of the constraints.

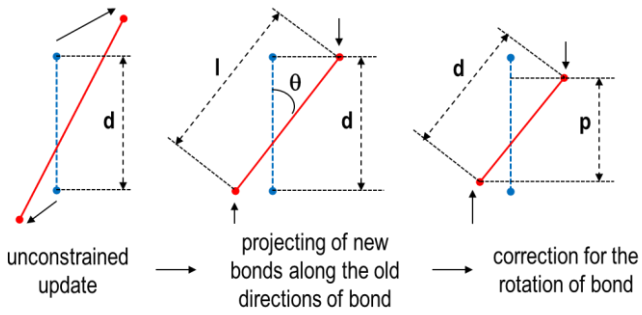

Figure 2.1. The three position updates in the LINCS algorithm. The blue dashed line is the old bond of length d, and the red solid lines are the new bonds $l = d\cos\theta$ and $p = (2d^2 - l^2)^{1/2}$.

For the specific case of rigid water models (TIP3P, SPC, SPC/E), another algorithm, called SETTLE, is introduced for resetting the positions and velocities to satisfy constraints on the rigid water model. In this case, three bonds are constrained,

for example, two real O-H bonds with the same lengths and one fictitious H-H bonds [70]. More details about the SETTLE algorithm are discussed in ref. [70]. The SETTLE algorithm is quite precise, fast and easily applied in standard MD packages.

2.1.4 Force Calculation and Long-Range Interactions

In order to update the positions and velocities in the stepwise numerical integration method, the forces acting upon the atoms have to be recalculated at each step. A summation for non-bonded interactions including van der Waal and electrostatic interactions has to be computed for all non-bonded pairs. Therefore, the non-bonded interaction calculation step costs tremendous simulation time. To speed up the calculation, the cutoff distance is introduced. This indicates that the non-bonded pair forces for two atoms separated by a distance larger than the given cutoff distance are excluded. This method handles well for the van der Waal interactions; however, it is not applicable for the systems with charged atoms due to the importance of the long-range electrostatic interactions. Many efficient techniques have been developed to deal with the electrostatic interactions such as the one which is to divide the electrostatic interactions into a long-range and short-range component. While the short-range component is computed in real space, the long-range one is calculated in Fourier space using different approaches, for example, Ewald, particle-mesh Ewald (PME), and Particle-Particle Particle-Mesh methods [68]. These approaches help reduce the computational time compared to the direct summation using the equation. In our simulations, we employ the PME algorithm to account for the long-range electrostatic interactions.

2.1.5 Periodic Boundary Conditions

Due to the limited computational resource and to speed up the simulations, only a finite sample of an extended system with an atomically detailed representation can be described explicitly in a computer model. Thus, the periodic boundary condition method is developed and implemented to allow a large system to be simulated. The MD algorithm is built up in such a way that the central box is surrounded by its images in all directions as shown in Figure 2.1. One atom in the central box interacts with other atoms in the same box as well as the atoms in the image box. Consequently, the atoms in the simulated box encounter the forces in the same way as in a large system. We build the simulation box with a cubic form in our studies and applied periodic boundary conditions in all directions.

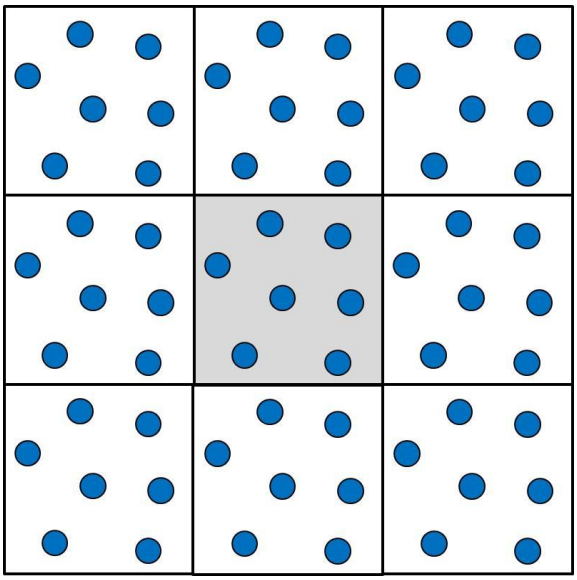

Figure 2.2. Illustration for periodic boundary conditions in MD simulations.

2.1.6 Thermostat

All of our simulations were conducted in the canonical ensemble NVT where the number of atoms N, volume V, and temperature T are taken to be constant. Using thermostat not only controls the temperature of the system but also prevents the

steady energy drift from the equilibrium state. Multiple thermostat approaches are introduced such as Andersen, Berendsen, Nosé-Hoover [68]. Among these methods, Nosé-Hoover thermostat is considered to be the most appropriate method that produces a correct canonical ensemble for studying the structure as well as the dynamics of systems of interest [68]. In the Nosé-Hoover thermostat the equation of motion is modified as $\frac{d^2\vec{r}_i}{dt^2} = \frac{\vec{F}_i}{m_i} - \frac{p_\xi}{Q}\frac{d\vec{r}_i}{dt}$, where the friction parameter ξ is a dynamic quantity which impedes or accelerates particles until the temperature T approaches the desired value T_0, Q determines the relaxation of the dynamics of the friction and its own momentum p_ξ is expressed as $\frac{dp_\xi}{dt} = (T - T_0)$.

The results from the equilibrium MD simulations are evaluated after approaching the equilibrium state. To ensure that the simulated systems reach equilibrium, the temperature, structural and dynamical properties which are recorded as a function of time are checked. The equilibrium state is obtained only when these properties do not change with the simulation time.

2.2 Umbrella Sampling Technique

The calculation of free energy landscape or potential of mean force (PMF) is essential for understanding many industrial and engineered processes such as chemical reactions, biochemistry, and rational drug design.

The free energy or PMF along a particular reaction coordinate $\mathcal{R}$, $A(\mathcal{R})$, is defined as $A(\mathcal{R}) = -\frac{1}{\beta}\log Q(\mathcal{R})$, where $Q(\mathcal{R})$ is the probability of the system at a specific reaction coordinate and β is equal to $1/(k_BT)$ with k_B being the Boltzmann's constant, T being the absolute temperature. In our studies, the reaction coordinate is defined as the absolute position of the centers of mass of the group of interested in the system. The output trajectories of atoms versus time from the simulations allow

us to calculate the probability of the system at a specific reaction coordinate $Q(\mathcal{R})$. Then by reversing the Boltzmann distribution function, we are able to compute the state of energy at this configuration.

The probability distribution $Q(\mathcal{R})$ of the system along the reaction coordinate is defined as followed [71]:

$$Q(\mathcal{R}) = \frac{\int \delta[\mathcal{R}(r) - \mathcal{R}] e^{-\beta E(r)} d^N r}{\int e^{-\beta E(r)} d^N r} \tag{2.7}$$

where $E(r)$ is the potential energy, and N is the number of degrees of freedom of the system.

In MD simulations, $Q(\mathcal{R})$ can be determined as the time average $P(\mathcal{R})$ in an ergodic system. The time average $P(\mathcal{R})$ is computed by equation $P(\mathcal{R}) = \lim_{t\to\infty} \frac{1}{t} \int_0^t \rho[\mathcal{R}(t')] dt'$, where t, ρ stand for the time and the frequency of $\mathcal{R}$ in a specific interval, respectively.

However, the problem is that the time average $P(\mathcal{R})$ converges slowly because of barriers along reaction coordinate $\mathcal{R}$. Therefore, in order to accelerate the barrier crossings, the umbrella sampling technique is implemented. In umbrella sampling, bias potentials along a reaction coordinate are introduced to move a system from one thermodynamic state to another. The intermediate steps are filled by a series of windows, at each of which an MD simulation is conducted. At each window a bias potential $w_i(\mathcal{R})$ is implemented to pull the reaction coordinate to the target value. Thus, the simulation of each window is biased with the potential energy $E^b(r) = E(r) + w_i(\mathcal{R})$. Then the biased distribution $P^b(\mathcal{R})$ is calculated using the equation with the biased potential energy E^b instead of E. To obtain the unbiased PMF $A_i(\mathcal{R})$, first we have to compute the unbiased distribution $P_i(\mathcal{R})$ from the biased distribution $P_i^b(\mathcal{R})$ [71]:

$$P_i(\mathfrak{R}) = P_i^b(\mathfrak{R})e^{\beta w_i(\mathfrak{R})}\langle e^{-\beta w_i(\mathfrak{R})}\rangle \quad (2.8)$$

and then the PMF of the window i, $A_i(\mathfrak{R})$, is computed as:

$$A_i(\mathfrak{R}) = -w_i(\mathfrak{R}) - \frac{1}{\beta}\log P_i^b(\mathfrak{R}) + F_i \quad (2.9)$$

where the bias potential often takes a quadratic form: $w_i(\mathfrak{R}) = \frac{k}{2}(\mathfrak{R} - \mathfrak{R}_i)^2$; the biased distribution $P_i^b(\mathfrak{R})$ is calculated from MD simulations and the constant F_i is computed using Weighted Histogram Analysis Method (WHAM) [72, 73].

In Chapter 5 we employed the umbrella sampling technique to calculate the PMF profiles for water and ethanol molecules as they approach the α-Al_2O_3 (0001) surface from the bulk solutions. In Chapter 7 we used this technique to obtain the umbrella sampling trajectories for the calculations of the diffusion profile for methane across the hydrated pores.

Chapter 3 Molecular Structure and Dynamics in Thin Water Films at Metal Oxide Surfaces: Magnesium, Aluminum, and Silicon Oxide Surfaces

The material presented in this section was published in 2012 in volume 116, pages 15962-15973 of The Journal of Physical Chemistry C.

3.1 Abstract

All-atom equilibrium molecular dynamics simulations were employed to investigate the structural and dynamical properties of interfacial water on the magnesium oxide surface. The solid support was modelled utilizing two different formalisms, both based on the CLAYFF force field. In one case, the atoms in the MgO substrate are allowed to vibrate, whereas in the other they are maintained rigid. The properties of water within the thin film are assessed in terms of density profiles in the direction perpendicular to the substrate as well as along planes parallel to the substrate, in-plane radial distribution functions, density of hydrogen bonds, residence times in contact with the substrate, and orientation distribution of interfacial water molecules. The contact angle for a small droplet on various substrates (MgO, SiO_2, Al_2O_3) was also calculated and compared with experimental observations. On MgO, the substrate in which the atoms are maintained fixed is the one that most closely reproduces experimental contact angles. This contrasts with results on other substrates, for example, silicon dioxide, on which the vibrations of the solid atoms were found to be useful for better predicting experimental observations. These differences suggest that proper force-field validation is necessary before investigating the structure of interfacial water on solid substrates. In the case of MgO, our analysis suggests that the vibrations of the solid atoms yield atomic-scale

roughness. This, in turn, causes water molecules to spread on the substrate. A brief comparison of water properties on MgO, alumina, and silica is provided.

3.2 Introduction

Magnesium oxide is used as support for metal catalysts and high temperature superconductors. It also provides a catalyst in its own right, occurs as the mineral periclase in a number of geological systems, and is a fundamental component of many minerals found in the subsurface. Because the MgO surface is well-characterized both by computational [74-76] and experimental efforts [77], it is a widely used model system for investigating interfacial processes. Several experimental [78-83] and theoretical studies [84-87] have investigated the properties of the water/MgO interface. Scamehorn et al. [88] studied water adsorption on a three-layer (001) MgO film using density functional theory (DFT) at the Hartree-Fock level. Minot et al. [89] employed DFT to study ice filling the inter-space between MgO (100) layers. It was found that water molecules close to the interface can dissociate under high pressure.

McCarthy et al. [90] studied the structure and dynamics of an isolated water molecule as well as those of water multilayers on a perfect MgO (001) surface, identifying the most favourable adsorbate/surface geometry. Ab initio potential energy results were then used to parameterize atomistic simulations, implemented to determine the density profiles and the probability distributions of angular orientation for interfacial water molecules in a thin supported film.

To complement these early results, we employ here extensive all-atom equilibrium MD simulations to investigate the structure of water molecules within thin films supported on MgO. In the case of SiO_2, it was found that accounting for atomic vibrations in the solid substrate is essential for capturing correctly the

dynamics of interfacial water [20, 21, 36], thereby supporting the contention that considering a substrate as completely immobile might lead to distortions in the predicted structure and dynamics of interfacial water [65]. Here we compare the results obtained when MgO is treated as rigid versus when its atoms are allowed to vibrate, finding better reproduction of experimental contact angles when the MgO atoms are maintained rigid. The resultant properties of interfacial water are compared to those reported earlier for water on alumina and silica dioxide [19, 20].

3.3 Simulation Methodology and Details

The MgO surface was represented as a solid film of thickness 10.51 Å. A theoretical study indicates that this is the thinnest film in which the charge density of the atoms in the center layer is similar to those found in the bulk material [75, 88]. Previous studies, both experimental [77, 91-93] and theoretical [75], have suggested that no significant surface reconstruction or relaxation occurs upon cleavage of a MgO crystal along the (001) plane. Therefore, the symmetry of the bulk is retained in the solid substrate. The plane group used to describe the (001) surface is derived from the space group Fm3m. The solid MgO substrate is aligned parallel to the XY plane of the simulation box, and a thin water film is prepared along the Z direction, following the procedures of prior investigations [18-20, 31]. The simulations were carried out in orthorhombic simulation boxes of constant volume. The X and Y dimensions of the simulation boxes reflect the periodicity of the solid crystalline substrate with values of 10.5 nm. The Z dimension was set to 16.27 nm.

The CLAYFF force field was implemented to simulate MgO [65]. To prevent vibrations of the solid atoms (non-vibrating MgO), we froze all atoms in the substrate. To allow vibrations of the atoms in the substrate (vibrating MgO), we kept the Mg and O atoms within the atomic layer furthest from the interface frozen,

whereas all other atoms were allowed to move as prescribed by CLAYFF. In Figure 3.1, the top view of the MgO surface (left panel), studied here, is compared with the fully hydroxylated alumina (middle panel) and silica surfaces (right panel) used in previous studies [19, 20]. The crystal structure of MgO (001) is cubic with octahedral Mg and O ions. By comparison, the oxygen ions on the (0001) crystallographic face of corundum α-Al_2O_3 surface yield a hexagonal close-packed structure with aluminum ions filling two-thirds of the octahedral interstices. The silica surface shown in Figure 3.1 is obtained from the β-cristobalite SiO_2 crystal [20, 31].

The rigid SPC/E model was used to simulate water [67]. The model is known to reproduce reasonably well the structure and dynamics of the bulk liquid at ambient conditions. Although CLAYFF was derived for solid substrates interacting with the SPC model of water, using either the SPC/E or the SPC models was found to yield no difference at the water-silica interface [20]. In the present work the SPC/E water bonds and angles were kept fixed by employing the SETTLE algorithm [70]. We simulated ~15,000 water molecules to create a thin water film of 45 Å thickness on MgO. As the Z dimension of the simulation box was 16.27 nm, and as the solid substrate thickness was 10.51 Å, an empty gap remains between the thin film and the periodic image of the solid substrate, as in prior studies [19, 20, 31].

Non-bonded interactions were modelled by means of dispersive and electrostatic forces. The electrostatic interactions were modelled by the Coulombic potential. Dispersive interactions were modelled with a 12-6 Lennard-Jones potential. The Lennard-Jones parameters for unlike interactions were determined by Lorentz-Berthelot combining rules [64] from the values of like components. The cutoff distance for all interactions was set to 9 Å. Long range corrections to electrostatic interactions were treated using the PME method [94].

All simulations were performed in the canonical ensemble (NVT), where the number of particles (N), the simulation volume (V), and the temperature (T) were held constant. T was fixed at 300 K and controlled by a Nosé-Hoover thermostat [95, 96] with a relaxation time of 100 fs. Periodic boundary conditions were applied in the three directions. The equations of motion were solved using the simulation package GROMACS [68, 69] by implementing the leapfrog algorithm [97] with time step of 1.0 fs. Total simulation time is 3ns. Data analysis was conducted over the last 2ns of the simulations, after 1 ns of equilibration were completed.

Additional simulations were carried out for computing contact angles, in which case 1000 water molecules were supported on the solid substrates for 5 ns.

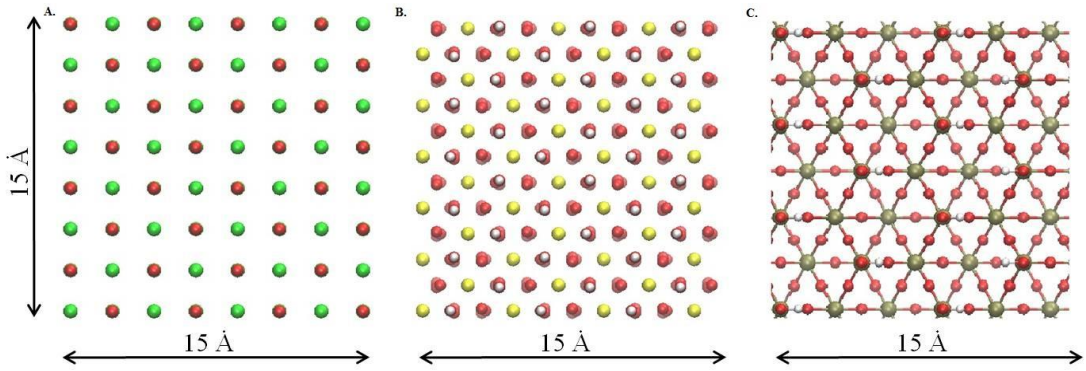

Figure 3.1. Top view of the magnesium oxide substrate used for the simulations reported here (left panel), of the fully hydroxylated alumina (middle panel) and of the low-OH-density hydroxylated silica (right panel) used in the prior works [12, 19, 20, 98]. Green, yellow, tan, red and white spheres represent magnesium, aluminum, silicon, oxygen and hydrogen atoms, respectively. The crystal structure of MgO is described as face-centered-cubic with six coordinated oxygen and magnesium atoms. The crystal structure of hydrated α-Al_2O_3 (0001) consists of aluminum atoms surrounded by six oxygen atoms, which yield a dense hexagonal packing. Hydrogen atoms are located at three specific positions bonding with oxygen atoms. For silica, all the silicon atoms which are parts of an incomplete tetrahedral were removed, and one silicon atom is bonded to non-bridging oxygen atoms, which were saturated with hydrogen atoms [31].

3.4 Results and Discussion

3.4.1 Contact Angle

It remains difficult to characterize the properties of a solid-water interface, in particular, when appropriate comparisons to experimental observations are attempted. Garde and coworkers [99] found that water density fluctuations near a substrate are related to a number of macroscopic phenomena, including the adsorption free energy of several compounds on hydrophilic versus hydrophobic surfaces. In general, however, the contact angle is one of the quantities that yields a straightforward comparison between experimental and simulation studies, despite a few known limitations (e.g., the simulated contact angle depends on the droplet size [100], experimental data suggest that the dynamic contact angle is a more reliable quantification of surface hydrophobicity in some applications than the static contact angle [101]. The atomic-level morphology of a surface strongly affects the contact angle in heterogeneous surfaces [102], and the static contact angle alone is not sufficient to characterize a surface toward macroscopic quantities such as hydrodynamic boundary conditions [103]).

We carried out simulations with 1000 water molecules placed on the substrates to quantify the contact angle for water on the model MgO surfaces considered. The snapshots obtained after 5ns of simulation are shown in Figure 3.2 for a non-vibrating (top) and a vibrating MgO surface (bottom panel). In both cases, the water-MgO interactions are described by the CLAYFF force field.

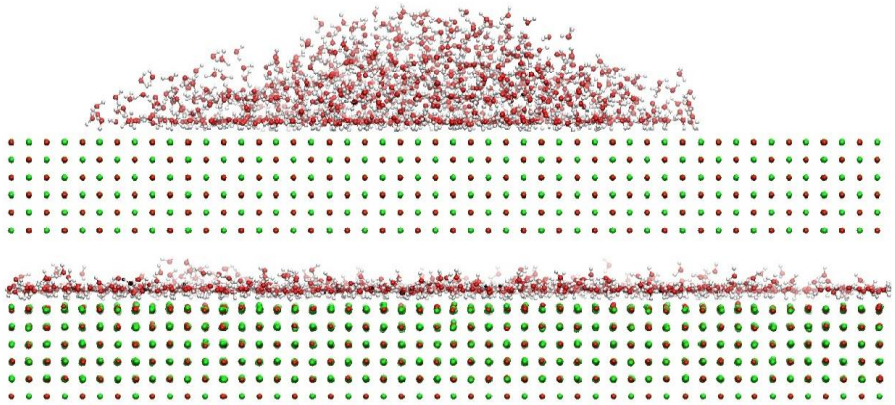

Figure 3.2. Representative simulation snapshots of a droplet of 1000 water molecules on a non-vibrating (top panel) and a vibrating MgO surface (bottom panel). Red, white and green spheres represent oxygen, hydrogen and magnesium atoms, respectively.

When the atoms in the MgO surface are maintained rigid, the nanodroplet yields a well-defined shape. The simulated contact angle, obtained following the method proposed by Giovambattista et al. [104], is of ~ 47° at 300K and ~ 56° at 293K, which is in reasonable agreement with the experimental value of 58.1° [105]. Surprisingly, when the MgO surface atoms vibrate, water molecules spread, yielding a monolayer and suggesting that the surface is much more 'hydrophilic' than reported by experiments. Because of the better agreement with experiments, the results in Figure 3.2 suggest that the CLAYFF force field could be used to simulate the water-MgO interface provided the solid atoms are not allowed to vibrate.

It remains to be understood why the vibration of the MgO atoms has such an important effect on the simulated water contact angle. It should be noted that the simulation started with a thin film of 1000 water molecules on the non-vibrating MgO surface yields a water droplet (i.e., the water molecules de-wet the surface). It should also be pointed out that when simulations are conducted in the NVE ensemble (the energy is maintained constant while the temperature fluctuates) the contact angle observed on the rigid MgO substrate is comparable to the one obtained conducting

the simulations in the NVT ensemble, provided that results obtained when the system is maintained at the same temperature.

In the force field implemented here, the atoms in the solid substrate are not bound to each other, and their vibrations are due to thermal fluctuations coupled to interactions with other atoms in the solid and in the interfacial liquid water. Although these modes of vibration are expected to be realistic, it is possible that describing the solid atoms as charged Lennard-Jones spheres does not fully capture the properties of the solid. However, it should be pointed out that the CLAYFF force field has been successful in reproducing experimental observations for a number of mineral substrates – water interfaces. An alternative explanation for the different contact angle might be related to effective temperature effects. (Preventing the solid atoms vibrations might effectively lower the temperature of the interfacial system). However, in the NVT ensemble, all the water molecules are maintained at the desired temperature.

To better understand the molecular reasons beyond the observed differences between the simulated contact angles when the MgO support is allowed to vibrate or not we conducted additional simulations in the NVT ensemble. For these simulations we used as the initial configuration for the solid substrate the final configuration obtained simulating water on the vibrating MgO substrate (Figure 3.2, bottom). The simulations were then conducted maintaining the MgO atoms frozen. This substrate is characterized by atomic-scale roughness as the atoms move by less than ~0.2 nm from their crystal positions. The 1000 water molecules simulated on this substrate were found to spread on it whether they were initially in a thin film or in a 3-D rectangular arrangement. Therefore, we conclude that allowing for the MgO atoms to vibrate induces atomic-scale roughness. It is this roughness that causes the water

molecules to spread on the substrate yielding a contact angle larger than that observed experimentally.

Although the contact angle differed on non-vibrating versus vibrating surfaces, other interfacial water properties, such as density profiles away from the solid, radial distribution functions (RDFs), planar density distributions, hydrogen bond (HB) network, and residence times are similar within thin water films supported on the two surfaces, as discussed below. The orientation of water molecules within the first hydration layer, however, is found to depend on whether the solid substrate vibrates.

3.4.2 Atomic Density Profiles

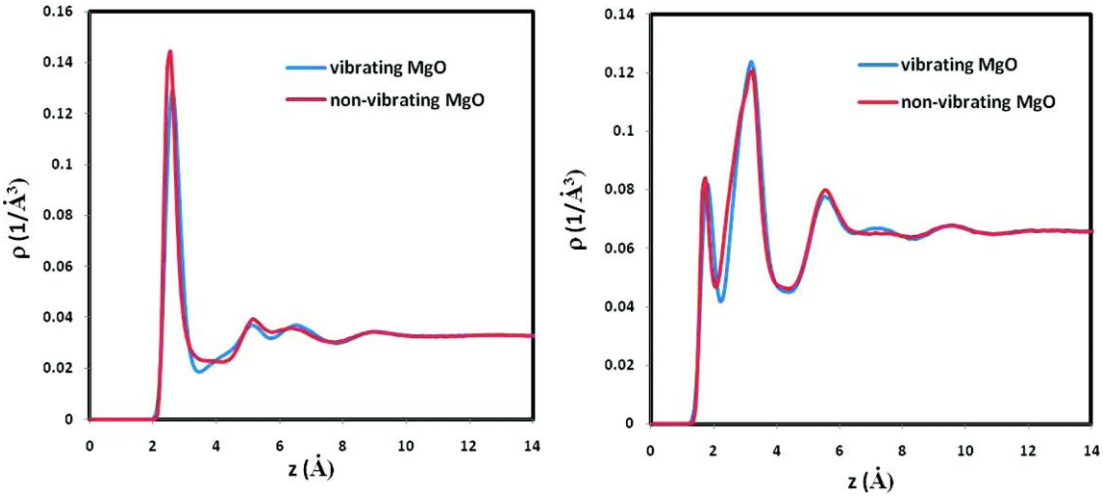

Figure 3.3. Oxygen (left panel) and hydrogen (right panel) atomic density profiles of water as a function of the vertical distance z from a vibrating (blue curve) and a non-vibrating (red curve) MgO surface.

In Figure 3.3, atomic density profiles of water oxygen (left panel) and hydrogen atoms (right panel) are reported as a function of the distance from a non-vibrating (red curve) and a vibrating MgO surface (blue curve). For the rigid MgO surface, the reference (z = 0) corresponds to the top plane of magnesium and oxygen atoms in the solid substrate. For the vibrating surface, because surface atoms oscillate around their

equilibrium positions, the averaged location of top layer atoms is considered as the reference.

The oxygen atomic density profiles (left panel) indicate the formation of a well-defined hydration layer at z=2.55 Å on the non-vibrating as well as on the vibrating surface. The comparable intensity of these peaks and the similar profiles suggest that surface atom vibrations do not affect the water structure.

The results obtained for the hydrogen atomic density profiles presented in the right panel support the observation summarized in the previous paragraph. By comparing the density profiles of oxygen and hydrogen atoms, the orientation of water molecules can be also studied, as discussed in detail elsewhere [18-20, 103]. Our results suggest that ~60% of the water molecules found in the first hydration layer near MgO project one of their hydrogen atoms toward the solid substrate, whereas the remaining waters tend to maintain both OH bonds pointing away from the surface.

In Figure 3.4 the density profile for oxygen atoms of water obtained from our simulations on the non-vibrating MgO surface is compared to that reported by McCarthy et al. [90], who also considered a non-vibrating MgO surface. McCarthy et al. [90] used the correlation-corrected periodic Hartree-Fock (PHF) theory to compute ab initio electronic structure energy data. They then used the results to fit the parameters A, B, and C of a pairwise additive potential energy expression:

$$V = \sum_{i<j} \left[\frac{q_i q_j}{r_{ij}} + A_{ij} \exp(-B_{ij} r_{ij}) - \frac{C_{ij}}{r_{ij}^6} \right] \tag{3.1}$$

The particle charges on the MgO ions were obtained by implementing a Mulliken population analysis of the PHF charge density results. The partial charges q obtained were +1.966 |e| and -1.966 |e| on magnesium and oxygen atoms,

respectively. In eq (3.1), *r* is the distance and subscripts *i* and *j* denote different atoms.

In CLAYFF, the Lennard-Jones (12-6) potential is chosen to describe van der Waals interactions, which are augmented by electrostatic forces as described by the following expression:

$$V = \sum_{i<j} \left\{ \frac{q_i q_j}{r_{ij}} + D_{o,ij} \left[\left(\frac{R_{o,ij}}{r_{ij}} \right)^{12} - 2 \left(\frac{R_{o,ij}}{r_{ij}} \right)^{6} \right] \right\} \quad . \qquad (3.2)$$

In CLAYFF, the particle charges on MgO are +1.05 |e| and -1.05 |e| on magnesium and oxygen, respectively. R_o and D_o are interaction parameters. The force field parameters implemented by McCarthy et al. and those used in the present work are summarized in Table 3.1.

McCarthy et al. [90] simulated either 64 or 128 water molecules and reported the density profiles in terms of the number of water molecules per MgO unit cell (n). They found a well-pronounced first hydration layer at z ≈ 2.25 Å from the substrate, which is in good agreement with our results. The intensity they reported for this first hydration layer, ~2.8 water molecules per MgO unit cell, corresponds to an atomic density of ~0.1524 ($1/Å^3$), which is slightly larger than that obtained from our simulations. This slight difference could be due to the larger number of water molecules considered in our simulations and to differences in the force fields implemented, but, in general our results show good agreement with those reported by McCarthy et al.

Table 3.1. Force field parameters implemented by McCarthy et al. and those implemented herein (CLAYFF).

	Force fields implemented by McCarthy et al. [90]				This work		
	A (kcal/mol)	B ($\dot{A}^{-1}$)	C(kcal/mol) $\dot{A}^6$	q	D_o (kcal/mol)	R_o ($\dot{A}$)	q(e)
O_{water}	331568	4.35	154	-0.82	0.1554	3.55	-0.82
H_{water}	700	3.37	18	0.41	0	0	0.41
Mg_{surf}	22645	4.24	1224	1.97	9.0298×10^{-7}	5.90	1.05
O_{surf}	95810	4.36	252	-1.97	0.1554	3.55	-1.05

More significant differences include a pronounced gap evidenced by the density profile proposed by McCarthy et al. in between the first and the second hydration layers, which is not present in our results, and a much more pronounced ratio between the density of the first hydration layer and the density far from the surface (at ~1 nm) observed by McCarthy et al. than in our results. These details suggest that the force fields implemented by McCarthy et al. yield a slightly more structured hydration layer, which could affect the prediction of macroscopic phenomena such as hydrodynamic slip and macromolecular adsorption. Experimental scattering results are necessary for discriminating which of the results shown in Figure 3.4 is the most realistic.

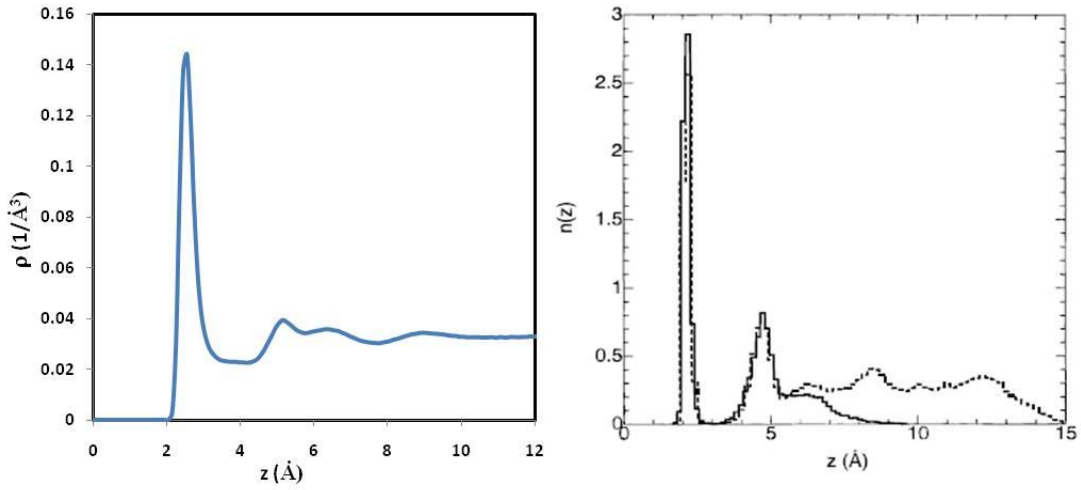

Figure 3.4. Oxygen atomic density profile as a function of distance z from the rigid MgO surface obtained in our simulation (left panel) and that reported by McCarthy et al. [90] (right panel). In the right panel, the number of water molecules simulated is either 64 (solid curve) or 128 (dotted curve). In the y axis, n (z) is the number of water molecules per MgO unit cell. The right panel is reproduced from Ref 88.

3.4.3 In-plane Radial Distribution Functions

In-plane RDFs for oxygen-oxygen, hydrogen-hydrogen, and oxygen-hydrogen pairs are calculated to quantify the different structural properties within the first hydration layer compared with those observed for water molecules in the second hydration layer or in the bulk. For these calculations, water molecules within a thin water slab parallel to the surface are considered. The thickness (δz) of the slab is 1 Å in all cases, and the center of a slab corresponds to one of the peaks in the density profiles shown in Figure 3.3. The bulk is identified as the center of the thin interfacial water film (z > 14 Å).

In Figure 3.5, results of oxygen-oxygen (left), hydrogen-hydrogen (middle) and oxygen-hydrogen (right) RDFs are shown for water in the first layer, second layer, and in the bulk (data obtained on the non-vibrating MgO). The results for $g_{OO}(r)$ and $g_{OH}(r)$ obtained for different hydration layers do not show significant differences,

although the data obtained in the first hydration layer suggest a slightly more pronounced structuring of water within the first layer (see left panel). More pronounced differences are observed for g_{HH}. In particular, several pronounced peaks are observed in the $g_{HH}(r)$ data obtained within the first hydration layer, suggesting significant water orientational ordering. The results obtained for the second hydration layer are very similar to those obtained for bulk water, indicating that MgO surface perturbs the water structure only at short distances, in qualitative agreement with the density profiles in Figure 3.3. Data for g_{OH} do not seem to depend much on the layer position, although the water molecules in the first hydration layer show slightly more ordered structure than those further away from the substrate.

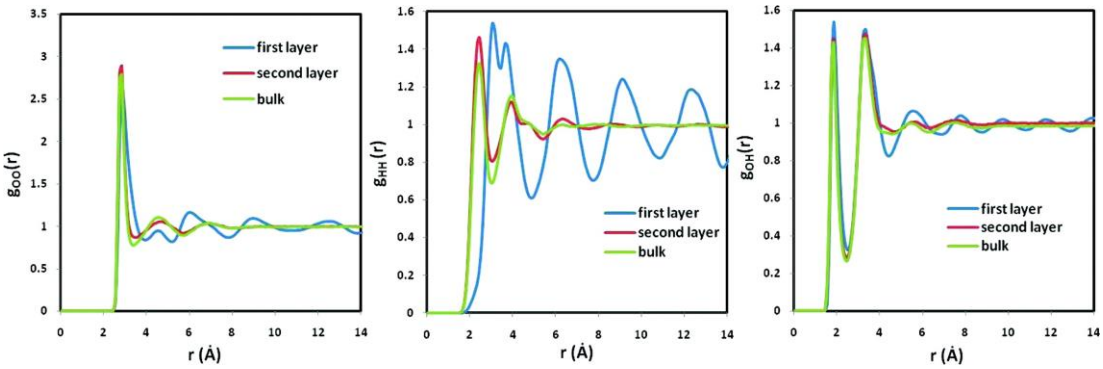

Figure 3.5. In plane oxygen-oxygen radial distribution functions $g_{OO}(r)$ (a), hydrogen-hydrogen radial distribution functions $g_{HH}(r)$ (b) and oxygen-hydrogen radial distribution functions $g_{OH}(r)$ (c) within first and second layers at the non-vibrating MgO surface. For comparison, data obtained for 'bulk' water are also shown. For 'bulk' water simulation results obtained in the center of the thin films simulated herein were used.

To determine how surface atom vibrations affect the configuration of the first hydration layer, we computed the in-plane $g_{OO}(r)$, $g_{HH}(r)$, and $g_{OH}(r)$ (RDFs) obtained within the first hydration layer for vibrating and non-vibrating MgO surfaces. The results are compared in Figure 3.6. The position and intensity of peaks in all RDFs are the same for both surfaces, suggesting that the vibrations of surface atoms

produce minimal differences in the structure of water within the first hydration layer compared with a rigid surface.

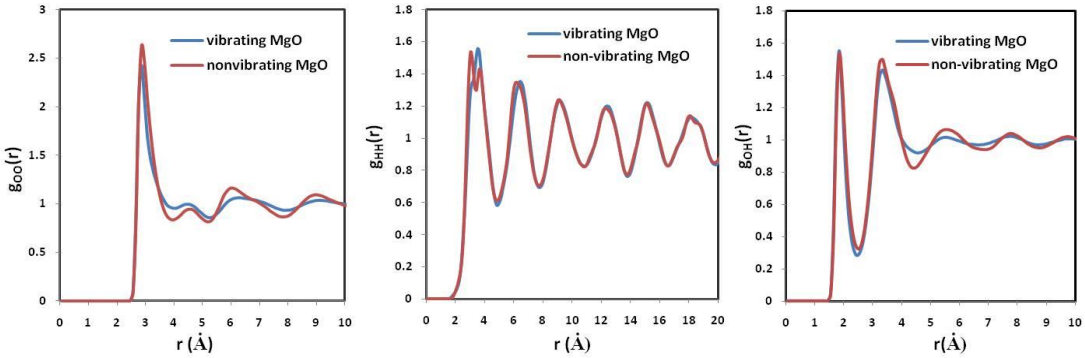

Figure 3.6. In plane oxygen-oxygen $g_{OO}(r)$ (a), hydrogen-hydrogen $g_{HH}(r)$ (b) and oxygen-hydrogen radial distribution functions $g_{OH}(r)$ (c) for water molecules within the first hydration layer on the vibrating and non-vibrating MgO surfaces.

3.4.4 Hydrogen Bond Network

In Figure 3.7, we report the density profiles of water-water HBs as a function of the distance z from non-vibrating (red curve) and vibrating (blue curve) MgO surfaces. We employed the geometric criterion proposed by Marti [106] to identify a pair of hydrogen-bonded water molecules. The position of one HB is then defined as the midpoint between acceptor oxygen and donor hydrogen atoms. No significant differences are found among the results obtained when vibrating and non-vibrating MgO surfaces are compared. In both cases, our results indicate a high density of water-water HBs at z = 2.65 Å, corresponding to the position of the first hydration layer (Figure 3.3). This suggests that water molecules in the first hydration layer have a strong tendency of forming HBs among themselves. A second peak is also observed for water – water HBs at ~0.6 nm from the substrate. This position corresponds to one pronounced density peak in the oxygen density profile (admittedly, the O peak is wide, see Figure 3.3). The correspondence of high density

of water – water HBs and the density peaks in the direction perpendicular to the substrate suggests that many HBs are formed between water molecules belonging to the same hydration layer. This contrasts with results reported for example for water on silica [31]. At larger distances from the surface, bulk-like properties are quickly restored, again suggesting that MgO has a short-ranged effect on interfacial water.

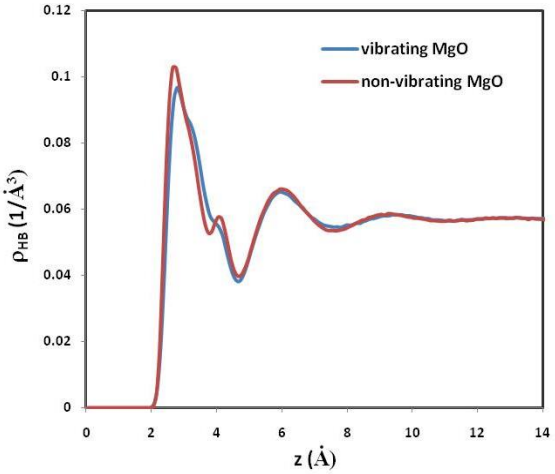

Figure 3.7. Density profiles of water-water hydrogen bonds as a function of distance from the vibrating (blue solid curve) and the non-vibrating (red solid curve) MgO surfaces.

3.4.5 In-plane Density Distributions

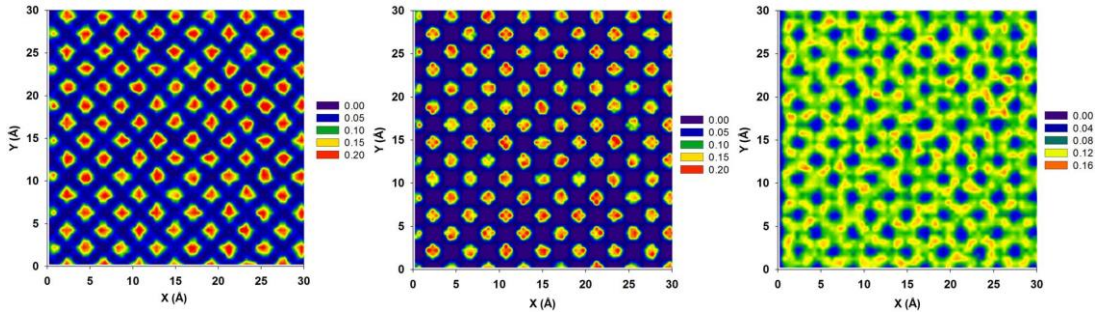

Figure 3.8. Surface density distributions of water oxygen atoms found in the first oxygen peak (left) and water hydrogen atoms found in the first (center) and the second hydrogen peaks (right) on the non-vibrating MgO surface. See Figure 3.3 for peak positions away from the surface. Densities are expressed in 1/Å^3.

To document the molecular structure of hydration water, we calculated the in-plane density distributions of oxygen and hydrogen atoms. In Figure 3.8, left panel, we present the in-plane density distribution of water oxygen atoms belonging to first oxygen peak. (See Figure 3.3 for peak position). The high-density areas (green-orange spots) of the contour plot indicate the positions where the water oxygen atoms preferentially reside. These positions are on top of the magnesium atoms on the solid substrate. (See left panel in Figure 3.1). The in-plane density distribution of the hydrogen atoms of water closest to the surface is shown in Figure 3.8, center panel. The positions of the high-density spots correspond to the position of oxygen atoms in the solid substrate, possibly a result of an attempt to form HBs. This water-solid interaction determines a preferential orientation of water molecules within the first hydration layer, reflected in the density profiles of Figure 3.3. The in-plane density distribution of hydrogen atoms in the second layer away from the substrate is shown in Figure 3.8, right panel. The contour plot shows a pattern of green-orange circular-like areas distributed around blue spots regularly distributed on the surface. The positions of the blue areas (low hydrogen density) correspond to the position of the high-density locations observed for hydrogen atoms in the first layer (center panel). The distribution of water molecules in the first hydration layer (left panel), coupled to the water orientation dictated by the interaction with the surface (center panel), is responsible for the patterned distribution of hydrogen atoms shown in the right panel. The results just discussed were obtained on the non-vibrating MgO substrate. They are analogous to those obtained on the vibrating substrate (results not shown for brevity).

3.4.6 Residence Times and Hydrogen Bond Network

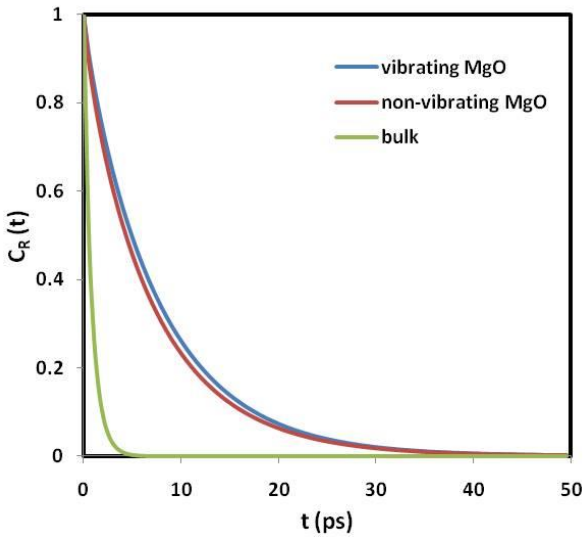

Figure 3.9. Residence autocorrelation functions $C_R(t)$ for water molecules within the first hydration layer on the vibrating (blue curve) and on the non-vibrating MgO surface (red curve). For comparison, the residence autocorrelation function for water molecules in a thin bulk layer is also shown (green curve).

In Figure 3.9, we report the residence autocorrelation functions $C_R(t)$ for water molecules within the first hydration layer on the vibrating (blue curve) and non-vibrating (red curve) MgO surfaces. The residence autocorrelation function obtained for water molecules within a thin layer in the bulk region far from the surface (green curve) is also shown for comparison. Following the prior procedures, the hydration layer was assigned a 1 Å thickness. The residence autocorrelation function can be used to quantify how long one water molecule remains in a specific layer. (For a discussion, see ref. [17, 20]). The faster the autocorrelation function decays, the shorter water molecules stay in a specific hydration layer.

Comparing the residence autocorrelation functions $C_R(t)$ for water molecules within the first hydration layer with that of bulk water suggests that the closer water molecules are to the substrate, the longer they remain within a given layer. This result is consistent with data observed for many other substrates, especially when

water molecules are attracted to the solid surface. The nearly identical features of $C_R(t)$ obtained for water molecules within the first hydration layer on both vibrating and nonvibrating surfaces suggest that the surface atom vibrations do not significantly affect the dynamical properties of interfacial water. This is surprising because in prior studies [20], it was found that surface atom vibrations significantly affect the dynamic properties of hydration water. In the case of silica, the effect was a function of the duration of surface water HBs. It is possible that on MgO the HBs between surface oxygen and water hydrogen atoms are not strongly affected by the vibrations of the solid atoms. It is also surprising that the residence autocorrelation functions $C_R(t)$ in Figure 3.9 decay faster for the non-vibrating compared to the vibrating MgO surface, although these differences are minimal and possibly due to statistical uncertainty. It is however possible that because the atomic-scale roughness induced by the vibration of the solid atoms promotes wetting, the individual water molecules are more strongly attached to the vibrating surface, yielding slower decays in the residence autocorrelation function.

3.4.7 Orientation Distribution of Interfacial Water

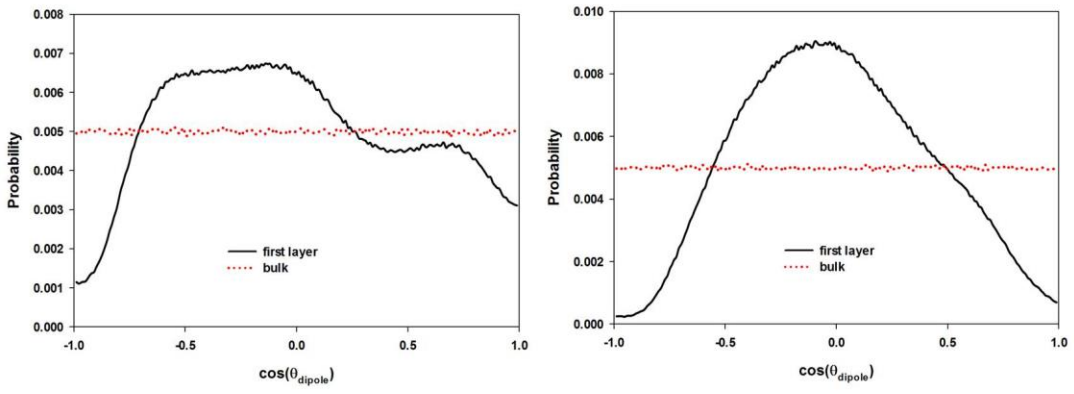

Figure 3.10. Probability distribution of $\cos(\theta_{dipole})$ within the first hydration layer on the vibrating (left) and non-vibrating (right panel) MgO surface. θ_{dipole} is the polar angle between the dipole moment of water molecules and the surface normal vector. Results for interfacial water (continuous black curve) are compared to those obtained for bulk water (dotted red curve).

In Figure 3.10, we present the probability distributions of the cosine of the polar angle formed between the dipole moment of water molecules and the surface normal vector for water on vibrating (left panel) and non-vibrating MgO substrates (right panel). We compare data obtained for water molecules within the first hydration layer (black curve) and those obtained for bulk water molecules (red dotted curve). The results show that interfacial water molecules on the vibrating surface have a much broader orientation distribution compared with those on the non-vibrating surface. This difference is probably related to the differences in atomic scale roughness of the two substrates. Interfacial water molecules adapt to the surface roughness typical of the vibrating MgO surface by adopting various orientations.

The results of Figure 3.10 complement the qualitative discussion regarding the orientation of interfacial water molecules presented in discussing Figure 3.3. The orientation distribution shown in Figure 3.10 is in fact consistent with having ~60% of the interfacial water molecules oriented so that one of their OH vectors is projected toward the solid substrate while the other points away from it.

It is also worth pointing out that water molecules in the bulk do not show preferential orientation. The preferential orientation at the interface, which is also reflected in the HB network discussed in Figure 3.7, suggests that strong dipolar interactions exist between water and the MgO substrate, whether the latter is vibrating or not. The model for water implemented herein cannot capture changes in the dipole moment of individual water molecules as they move from the bulk to an interface. Polarizable models are necessary for such investigations.

3.4.8 Comparison with Other Substrates

We can gain further insight into solid-water interfacial behaviour by comparing contact angles, density profiles, in plane distributions as well as residence times for interfacial water obtained on the nonvibrating MgO, hydroxylated α-Al_2O_3, and hydroxylated SiO_2 surfaces. Results obtained on alumina and silica are discussed at length in prior studies [19, 20, 31]. In the discussion below, the hydroxyl groups in the alumina and silica substrates are allowed to rotate (all other atoms are maintained rigid), whereas all atoms on MgO are rigid. These representations, based on our analysis, provide realistic descriptions of the three solid-liquid interfaces.

3.4.8.1 Contact Angles

We performed simulations for droplets of 1000 water molecules on the various substrates, as shown in Figure 3.11. The results demonstrate that water molecules wet alumina and silica, forming one hydration layer. The remaining water molecules form a droplet on top of the first hydration layer (Figure 3.11b, c). Conversely, a droplet is found on the MgO surface, as discussed in Section 1 (Figure 3.11a), without the formation of one hydration layer. Although this suggests that alumina and silica are more hydrophilic than MgO, the interesting result is that water molecules spread on alumina and silica, yielding one hydration layer, but then one water droplet forms on top of this layer (Figure 3.11b, c, side views, and Figure 3.12, top view). This observation is similar to the simulation results reported by Wang et al. [107], who found, by MD simulations under ambient conditions, that after water molecules form one monolayer on an overall neutral, yet ionic substrate, additional "*water does not wet a water monolayer*". Under appropriate conditions, they found few HBs between the water molecules in the first hydration layer near the substrate and those within the water droplet, which explained the unexpected results, including

the larger-than-expected contact angle for the water droplet supported onto the water monolayers. From an experimental point of view, Lutzenkirchen et al. [108] recently reported infrared data for thin water films on the sapphire C-plane [α-Al_2O_3 (0001)], which also suggest that the first hydration layer renders the surface hydrophobic to additional water molecules. Richardson et al. [109], using FT-IR spectroscopy, reported qualitatively similar observations.

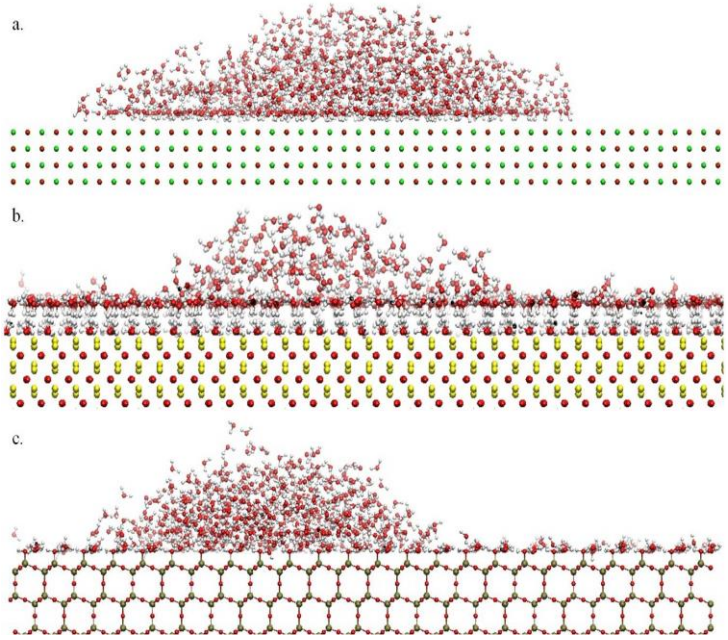

Figure 3.11. Representative simulation snapshots of droplets formed by 1000 water molecules supported on a non-vibrating MgO (a), hydroxylated alumina (b) and silica (c) surfaces. Red, white, green, yellow, and tan spheres represent oxygen, hydrogen, magnesium, aluminum and silicon atoms, respectively.

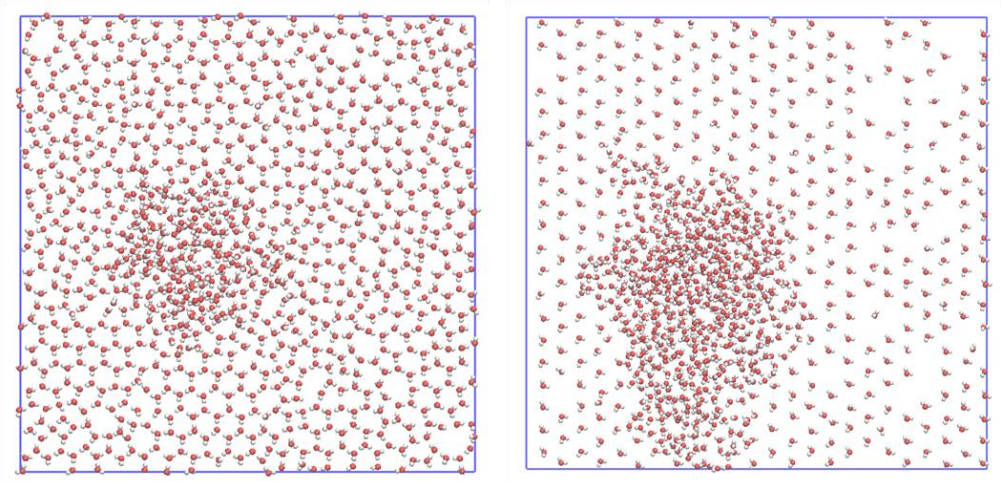

Figure 3.12. Top views of panels (b; Al_2O_3) and (c; SiO_2) (left and right panel, respectively) reported in Figure 3.11. The color code is analogous to that used in Figure 3.11. Only water molecules are shown for clarity.

3.4.8.2 Atomic Density Profiles

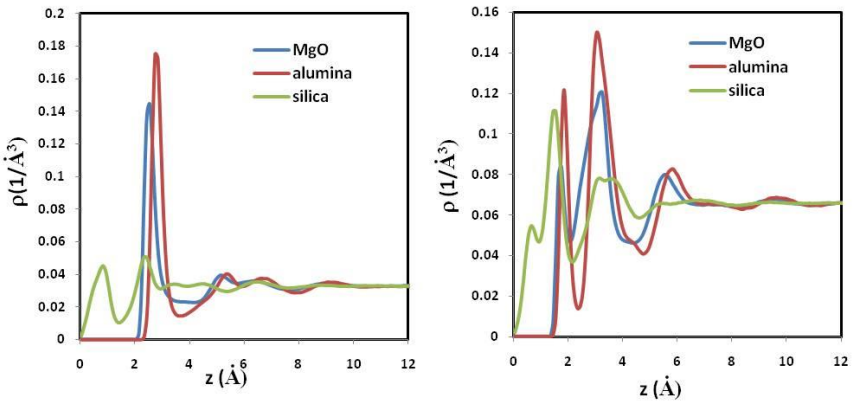

Figure 3.13. Atomic oxygen (left) and hydrogen (right) density profiles as a function of the vertical distance z from the non-vibrating MgO (blue), hydroxylated alumina (red), and hydroxylated silica (green) surfaces.

In Figure 3.13, we report oxygen (left) and hydrogen (right panel) atomic density profiles on the MgO, and hydroxylated α-Al_2O_3 and silica surfaces. Results on alumina and silica are from prior studies [19, 20]. The reference z = 0 for the alumina and silica surfaces is the plane formed by the oxygen atoms of the surface

hydroxyl groups. The results for the oxygen atomic density profiles show that the intensity of the first oxygen water layer on MgO is comparable to that found on alumina and more intense than that found on silica. This is due to the different number of adsorption sites accessible to water on each surface. On MgO, water oxygen atoms adsorb on top of the Mg atoms (Figure 3.8), whereas on alumina and silica, interfacial water molecules form HBs with hydroxyl groups on the surfaces. The density of adsorption sites on MgO is comparable to that found on alumina (14 Mg atoms/nm^2 on MgO and 15 hydroxyl group/nm^2 on alumina [19]), but larger than that found on silica (4.54 hydroxyl groups /nm^2 [20]). The higher density of adsorption sites is responsible for the larger density of water oxygen atoms found within the first hydration layer.

As explained above (Section 2) and in other detailed reports [18-20, 103], by comparing the intensity and position of the density profiles for oxygen and hydrogen atoms, it is possible to estimate semi-quantitatively the orientation of interfacial water molecules, although detailed analysis such as those in Figure 3.10 are preferable for such characterizations.

3.4.8.3 In-plane Density Distributions

In Figure 3.14 the in-plane density distributions of oxygen atoms in the first (A) and second (B) hydration layers on MgO (left panels), alumina (middle panels), and silica (right panels) surfaces are presented. Results of surface density distribution of oxygen atoms in the first hydration layer on alumina and in both layers on silica are from prior studies [19, 20]. The results suggest that water molecules occupy specific adsorption sites on each of the three surfaces. The distribution of water oxygen atoms within the first hydration layer reflects the atomic structure of the top layer of the solid substrate. On MgO, the location of water oxygen atoms correspond to the

surface Mg atoms, whereas on silica and alumina, water oxygen atoms are found near the surface hydrogen atoms, implying the formation of HBs between water molecules and the solid substrates [110]. Silica affects the structure of water molecules up to two hydration layers, whereas alumina and MgO affect only the first hydration layer. (Compare left and middle B panels to the right B panel in Figure 3.14). These results are in agreement with the density profiles presented in Figure 3.13. However, note that the second hydration layer on silica is found at a z position that corresponds to approximately that of the first hydration layer on both MgO and alumina.

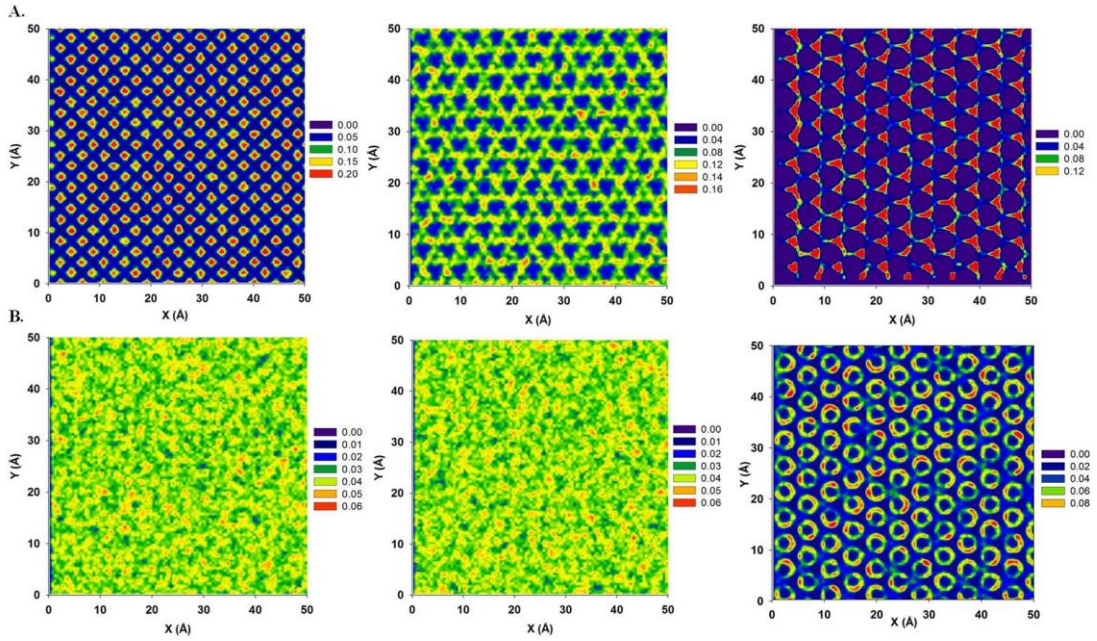

Figure 3.14. In-plane density distributions (parallel to the surface) for water oxygen in the first (A) and second (B) hydration layers formed on nonvibrating MgO (left panels), alumina (middle panels) and silica (right panels). See Figure 3.12 for the position of each hydration layer. Densities are expressed in $1/Å^3$.

3.4.8.4 In-plane Radial Distribution Functions

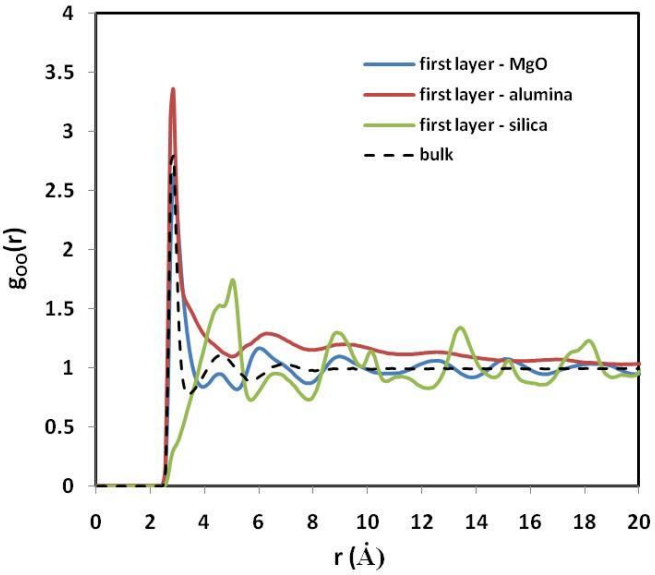

Figure 3.15. In plane oxygen-oxygen radial distribution functions, $g_{OO}(r)$, obtained within the first hydration layer on nonvibrating MgO (blue), alumina (red), and silica (green). For comparison, data for bulk water are also shown as black broken curve.

In plane oxygen-oxygen RDFs were calculated among the water molecules within the first hydration layer to gain better insight regarding the structural interfacial properties on the three substrates. For comparison, data for bulk water are also provided. The thickness (δz) of the first hydration layer was considered to be 1 Å in all cases. The results, shown in Figure 3.15, suggest that the water molecules within the first hydration layer on alumina have a structure similar to a dense liquid. Water structuring seems to increase on MgO. Some evidence of long-ranged order appears on silica, although on this substrate the first peak in the RDF is shifted to ~0.5 nm because of the large distance between preferential adsorption sites on this substrate. (See top right panel in Figure 3.14). These results are a direct consequence of the structuring imposed by the solid substrates and are consistent with the in-plane density distributions shown in Figure 3.14A.

3.4.8.5 Residence Times and Hydrogen Bond Networks

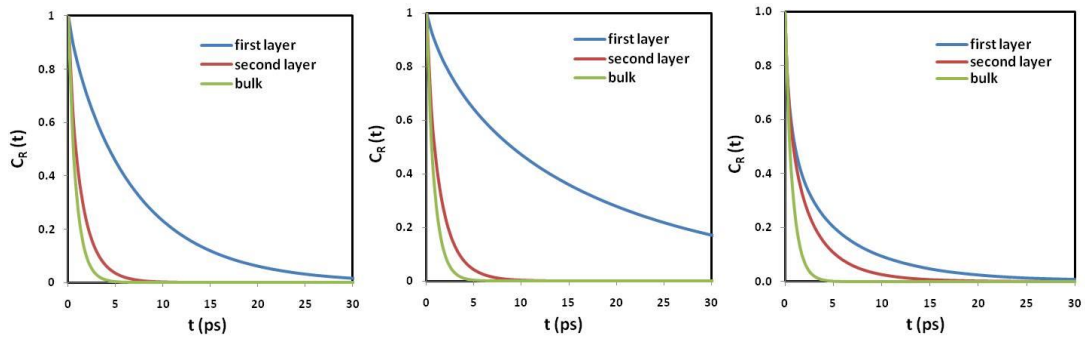

Figure 3.16. Residence autocorrelation functions $C_R(t)$ for water molecules within various interfacial layers on non-vibrating MgO (a), hydroxylated alumina (b), and hydroxylated silica (c). Data for bulk water are provided for comparison.

In Figure 3.16, we report the results for the residence autocorrelation functions $C_R(t)$ obtained for water molecules within first and second hydration layers as well as in the bulk on MgO (left), alumina (middle) [19], and silica (right) [20]. These results confirm that on these three substrates water molecules always remain within the first hydration layer longer than they do within the second layer and in the bulk region. The water molecules in the first hydration layer on alumina remain within the hydration layer much longer than those found within the first hydration layer either on MgO or on silica. The residence autocorrelation function for water molecules in the first layer on MgO decays more slowly than the corresponding one on silica. Water molecules reside within the second hydration layer on silica for longer times, on average, than they do on either MgO or alumina.

The dynamical properties of interfacial water depend strongly on the interactions between water molecules and the solid substrate as well as on those between different water molecules. Such interactions are often reflected on the HB network. In Figure 3.17, water-water HB density profiles are shown for the three substrates. The HB density in the first hydration layer is the largest on alumina and the least on

silica. The high water-water HB density, combined with the high atomic density (see Figure 3.13), is probably responsible for slowing down the dynamical properties of interfacial water molecules.

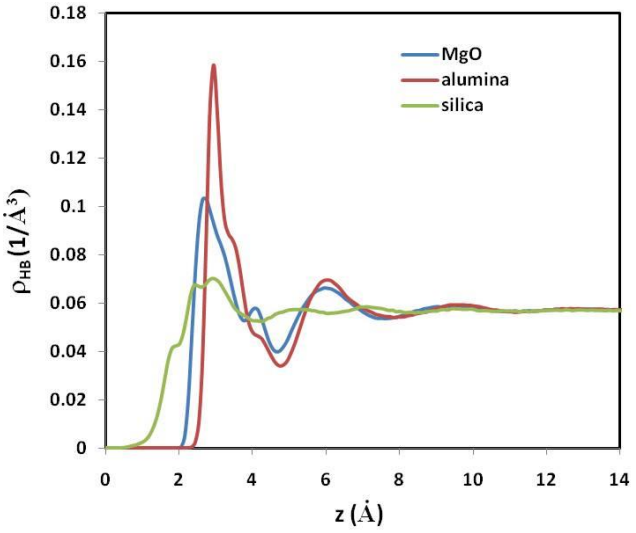

Figure 3.17. Density profiles of hydrogen bonds formed between water molecules as a function of the distance z from the non-vibrating MgO (blue), hydroxylated alumina (red) and hydroxylated silica (green).

3.5 Summary and Conclusions

MD simulations were employed to study structure and dynamics of water molecules in contact with a flat MgO substrate. Water molecules were modelled using the SPC/E model, whereas the solid substrate was simulated using the CLAYFF force field. Two representations for the solid were employed. In the first, all surface atoms were maintained rigid, whereas in the second, they were allowed to vibrate. By computing the contact angle for droplets of 1000 water molecules, we observed that better agreement with experimental data is achieved when the solid atoms are maintained rigid. The results obtained for water within thin films supported on rigid versus vibrating MgO did not exhibit significant differences, except for the water orientation within the first hydration layer. The results discussed

include atomic density profiles in the direction perpendicular to the surface, atomic density distribution along planes parallel to the substrate, HB networks, 2-D RDFs in the direction parallel to the substrate, and residence autocorrelation functions used to assess the average residence time for water in contact with the solid substrate. The results are also compared with those obtained previously for water supported on model silica and alumina substrates in an attempt to relate the properties of a solid substrate to those of the film of interfacial water supported by the substrate.

The results show a pronounced patterning of interfacial water, especially in the first hydration layer, on all the three substrates considered. The distribution of solid atoms on the substrate determines the availability of preferential adsorption sites where water molecules reside. Depending on the surface arrangement of these preferential adsorption sites, the planar distribution of water molecules at the interface, and the network of water-water HBs are established. These, in turn, determine how far the surfaces perturb the properties of interfacial water and affect the residence time of water molecules in contact with the solid substrates. Although complete experimental corroboration is still not possible, the simulation results presented here are valuable for understanding macroscopic phenomena including ion adsorption at interfaces and hydrodynamic properties in the earth subsurface.

Chapter 4 Liquid Ethanol Simulated on Crystalline Alpha Alumina

The material presented in this section was published in 2013 in volume 117, pages 3829-3840 of The Journal of Physical Chemistry B.

4.1 Abstract

Equilibrium molecular dynamics simulations were employed to investigate the structural properties of interfacial liquid ethanol on two alumina surfaces – the (0001) and the $(1\bar{1}02)$ terminations of α-Al_2O_3 – both described using the CLAYFF force field. The resultant atomic density profiles show that ethanol molecules in the first monolayer are well ordered and that their distribution depends on the surface OH groups. A pronounced dipolar orientation is found for the ethanol molecules in the first layer and also, although to a smaller extent, among the ethanol molecules in the second molecular layer. The orientational distribution predicted for the methyl group of ethanol on α-Al_2O_3 $(1\bar{1}02)$ is consistent with that observed experimentally by Shen and coworkers (*J. Phys. Chem. Lett.* 2011, 2, 1831). The orientation of molecules in the second layer is opposite compared to that found in the first adsorbed molecular layer. Our simulations show long residence times and slowly decaying reorientation autocorrelation functions for ethanol molecules in the first adsorbed layer, suggesting that within the first adsorbed layer ethanol molecules are strongly coordinated with both α-Al_2O_3 (0001) and α-Al_2O_3 $(1\bar{1}02)$ surfaces. Analysis of the hydrogen bond network confirms that preferential surface-ethanol interactions are responsible for such observations.

4.2 Introduction

Ethanol is one of the most popular hydrogen-bonding and amphiphilic fluids. An increasing number of computer simulation studies focused on bulk liquid ethanol are being reported in the literature [111-117]. For example, Saiz et al. [111] employed MD simulations to study structure and dynamics of liquid ethanol at four thermodynamic states using the transferable Optimized Potential model for Liquid Simulations (OPLS) force field [66]. The results were in overall agreement with available experiments for, e.g., bulk density and diffusion coefficients [118-120]. The OPLS force field was also used by Wensink and coworkers [114] to study dynamical properties of water/alcohol mixtures. More computational demanding polarizable and flexible models have also been developed. Wang and Cann [116], e.g., used ab initio B3LYP/6-311++G(d,p) data to parameterize accurate force fields for ethanol. Although polarizable and flexible models appear to be essential for modelling complex biological systems [116, 121-124], Noskov et al. [115] showed that results for enthalpy of evaporation, molecular volume, dielectric constant, and self-diffusion coefficient obtained by implementing polarizable force fields are comparable to those obtained by using non-polarizable force fields. Noskov et al. [115] noted that polarizable force fields should be used to accurately predict the dielectric constant and minima in the self-diffusion coefficients for ethanol-water mixtures at various compositions. Nonpolarizable models are used in this study because we are primarily interested in the structure of ethanol at solid-liquid interfaces.

Computational studies of liquid ethanol on solid substrates are somewhat scarce. Andoh and co-workers [125] conducted a series of NVT MD calculations for liquid ethanol on a fully hydroxylated silicon dioxide surface. The results showed the

formation of molecular clusters of hydrogen-bonded ethanol. Cooke et al. [126] investigated ethanol and water on the $(10\bar{1}4)$ surface of calcite. A highly ordered adsorbed layer of ethanol was found to be stable even in the presence of water.

Regarding experimental data, Rossetto et al. [127] recently studied the impact of ethanol on the adhesion of alumina surfaces in water. They found that the adhesive energy in aqueous solutions decreases as the ethanol concentration increases. The impetus for our work is based on recent experimental data reported by Shen et al. [37], who studied ethanol on the $(1\bar{1}02)$ alumina surface using sum frequency vibrational spectroscopy (SFVS). We use equilibrium MD to study structural and dynamical properties of ethanol within thin liquid films formed on two alumina surfaces – (0001) and $(1\bar{1}02)$ terminations of the hydroxylated α-Al_2O_3 – under ambient conditions. Good agreement is observed between simulated and experimental data. Quantitative information regarding how the surface features affect adsorbed ethanol via preferential surface-ethanol interactions is discussed.

4.3 Simulation Methods and Algorithms

Two crystallographic faces of sapphire α-Al_2O_3 (space group $R\bar{3}c$) [98] – C-plane (0001) and R-plane $(1\bar{1}02)$ – were used to model the alumina surfaces. Both C- and R-plane surfaces are stable termination facets on natural sapphire crystals. Coustet et al. [128] determined that the C-plane surface is hydroxylated under humid atmospheres. The fully hydroxylated C-plane contains ~15 OH groups per square nanometer. Shen et al. [129] investigated the protonated surface structure of the R-plane using SFVS. The hydroxylated R-plane shows three distinct OH species: one H-bonded OH associated with the Al_2OH of the second oxygen surface layer, one H-bonded OH, and one dangling OH associated with the $AlOH_2$ group of the topmost

oxygen layer [129]. Shen et al. suggested that the separation distance between the second and third oxygen surface layers is reduced by ~0.55Å compared than that of the bulk crystal, and by ~0.3Å compared to that of the crystal truncation rod (CTR) model [130]. The model implemented herein reflects such recommendations.

In Figure 4.1 we present the side view of the fully hydroxylated C-plane (0001) (left panel) with the surface normal (0001) and (1100) directions aligned with the Z and Y axis of the simulation box, respectively. We also show the fully hydroxylated R-plane ($1\bar{1}02$) (right panel), with the surface normal ($1\bar{1}02$) and ($1\bar{1}0\bar{1}$) directions aligned with the Z and Y axis of the simulation box, respectively. The top views of both substrates are shown in Figure 4.2. These are the substrates used in our simulations. The simulations were carried out in orthorhombic simulation boxes of constant volume. The X and Y dimensions of the simulation boxes reflect the periodicity of the solid crystalline substrate with values of 47.6 Å (49.5 Å) and 47.6 Å (46.08 Å) for the C-plane (R-plane). The Z dimension was set to 300 Å for both cases.

A thin ethanol film is prepared along the Z direction, following the procedures of prior investigations [18-20, 31]. See Figure A.1 in Appendix A for a representative simulation snapshot of the simulated system. Using 2000 ethanol molecules, we created a thin film of ~ 94 Å thickness. As the Z dimension of the simulation box was 300 Å, and as the solid substrate thickness of C-plane and R-plane sapphire surfaces were 11.91 Å and 12.58 Å, respectively, an empty gap exists between the thin film and the periodic image of the solid substrate, as in prior studies [19, 20, 31].

The CLAYFF force field was implemented to describe both alumina substrates [65]. The Optimized Potential for Liquid Simulation in the United Atom form

(OPLS-UA) [66] was implemented to describe ethanol. The methyl (CH_3) and methylene (CH_2) groups of ethanol are treated within the united atoms formalism. Bond lengths and angles in an ethanol molecule are kept fixed by implementing the LINCS algorithm [69].

Nonbonded interactions were modelled by means of dispersive and electrostatic forces. The electrostatic interactions were modelled by the Coulombic potential. Dispersive interactions were modelled with a 12-6 Lennard-Jones potential. The Lennard-Jones parameters for ethanol – ethanol and ethanol – alumina interactions were determined by geometric combining rules [64] from the values of pure components, while the Lorentz-Berthelot combining rules are used to compute the LJ parameters within the CLAYFF formalism to simulate alumina. The cutoff distance for all interactions was set to 9 Å. Long range corrections to electrostatic interactions were treated using the PME method [94].

All simulations were performed in the canonical ensemble (NVT) where the number of particles (N), the simulation volume (V), and the temperature (T) were kept constant. The simulated temperature was held at 298 K and controlled by a Nosé-Hoover thermostat [95, 96] with a relaxation time of 100 fs. Periodic boundary conditions were applied in all three directions. The simulation package GROMACS [68, 131] was used to solve the equations of motion by implementing the leapfrog algorithm with 1.0 fs time steps. The total simulation time was 25 ns. Data analysis was conducted over the last 5 ns of the simulations, after 20 ns of equilibration were completed. Equilibration was achieved when the density of ethanol in the center of the film approached the experimental bulk density at the same thermodynamic conditions.

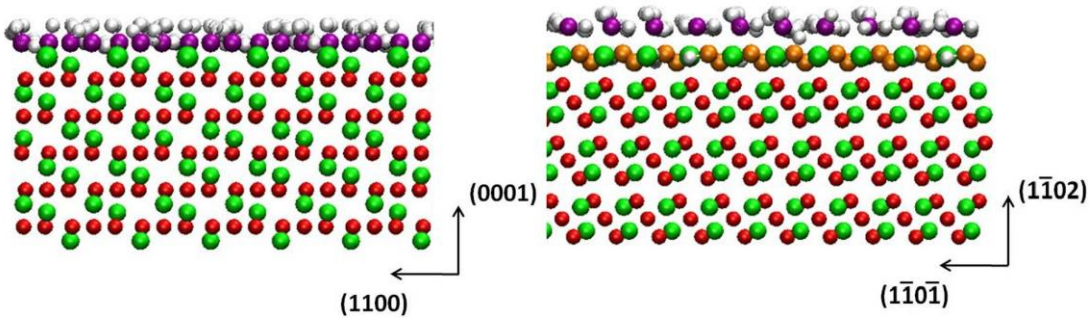

Figure 4.1. Side view of the fully hydroxylated C-plane (0001) (left) and R-plane (1$\bar{1}$02) (right) sapphire surfaces. Green and red spheres represent aluminum and oxygen atoms in the bulk structure, respectively. For the C-plane, surface hydroxyl groups are illustrated using purple for oxygen and white for hydrogen atoms. For the R-plane, surface hydroxyl groups are illustrated using purple for the first oxygen surface layer, orange for the second and third oxygen surface layers, and white for hydrogen atoms. See text for a discussion regarding the different types of OH groups expected on the R-plane.

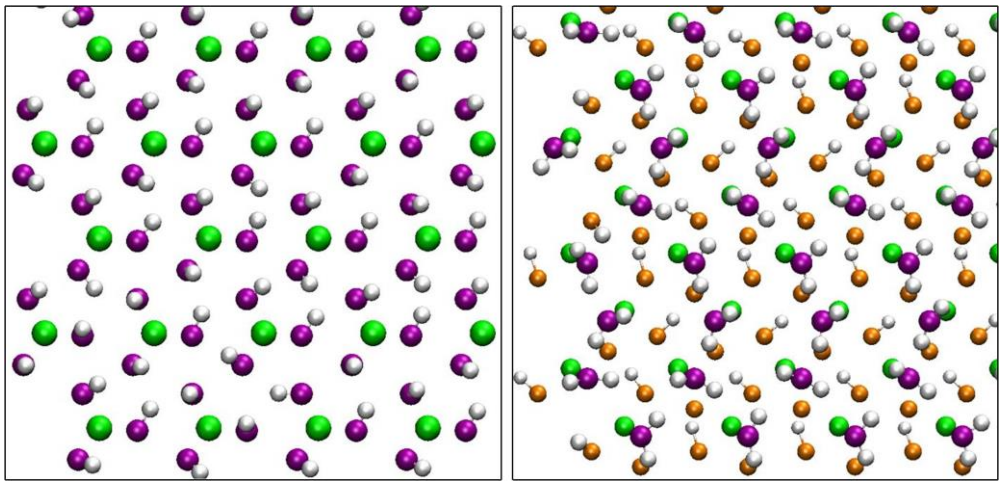

Figure 4.2. Top view of the surface hydroxyl groups on the (0001) (left) and (1$\bar{1}$02) (right) α-Al_2O_3 surfaces. The color scheme for surface hydroxyl groups is the same as that in Figure 4.1.

4.4 Results and Discussion

4.4.1 Atomic Density Profiles

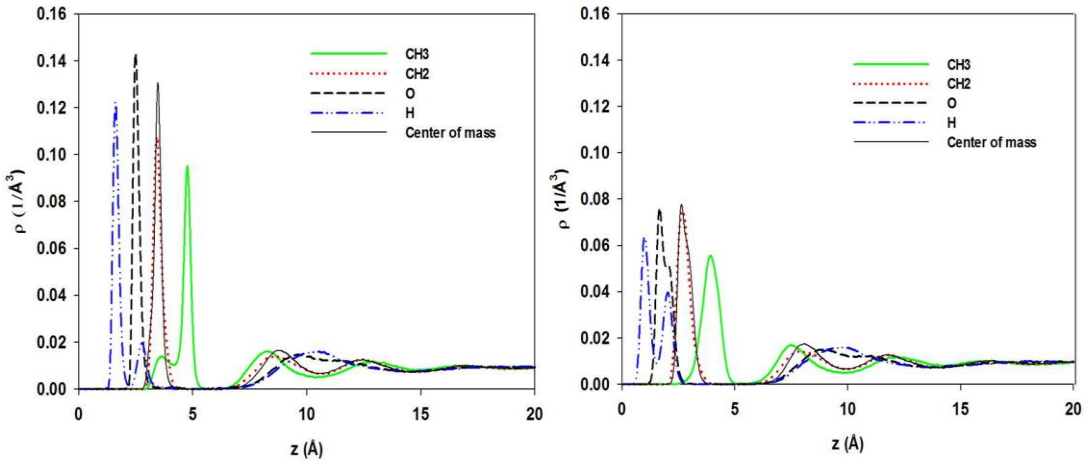

Figure 4.3. Methyl group (green solid curve), methylene group (red dot curve), oxygen (black dash curve) and hydrogen (blue double-dot dash curve) atomic density profiles of ethanol on the fully hydroxylated C-plane (left) and R-plane α-Al_2O_3 (right) surfaces. In both panels we also report the density profiles for the center of mass of ethanol molecules (black solid curves).

Figure 4.3 reports the atomic density profiles of methyl (CH_3) (green solid curve), methylene (CH_2) (red dot curve), oxygen (black dash curve), and hydrogen atoms (blue double dot dash curve) of ethanol molecules on the fully hydroxylated C-plane (left panel) and R-plane α-Al_2O_3 (right panel) as a function of the vertical distance. For the C-plane, the reference (z = 0) corresponds to the top plane of the hydroxyl group oxygen atoms of the substrate; the reference (z = 0) for the R-plane is the plane of the topmost oxygen layer.

The first methyl, methylene, oxygen and hydrogen peaks are formed on the C-plane at 4.75, 3.45, 2.45, and 1.65 Å from the surface, respectively. The methyl, methylene, oxygen and hydrogen peaks within the second layer appear at positions 8.25, 8.55, 9.65, and 10.35 Å, respectively. The results suggest that ethanol molecules found in the first adsorbed layer project their OH groups toward the

surface, while they extend their methyl groups toward the bulk liquid. This preferential orientation allows ethanol molecules to form HBs with the surface OH groups (according to a geometric criterion, HBs can exist when the distance between O and H atoms involved is 1.5 - 2.1 Å [132-134]).

The first methyl, methylene, oxygen, and hydrogen peaks are formed on the R-plane at 3.95, 2.65, 1.65, and 1.05 Å from the surface, respectively. The positions of the methyl, methylene, oxygen, and hydrogen peaks in the second layer appear at 7.45, 7.75, 8.85, and 9.85 Å, respectively. Even in this case ethanol molecules in the first layer orient their OH bond toward, and the methyl group away from the surface. The orientation of ethanol molecules within the second layer is opposite that on the first layer.

The atomic density profiles obtained on the two substrates are qualitatively similar to each other. However, the first adsorbed layer on the R-plane is at a slightly shorter distance than that at which the first layer is found on the C-plane. For example, the first hydrogen peaks are observed at 1.05 Å and 1.65 Å from the two substrates, respectively. This might be a consequence of the choice of reference planes. A smaller methyl group peak within the first layer on the C-plane is also noticed. This peak might not be visible on the R-plane because in the latter the first methyl peak is wider than on the C-plane.

The ethanol hydrogen atoms yield two well-pronounced density peaks near both surfaces. While the second peak at 2.75 Å is very weak on the C-plane, on the R-plane the second peak at 2.05 Å becomes comparable to the first. This probably reflects a different HB network formed on the two substrates. Note also that the density profile for the O atoms of ethanol yields a single, narrow peak on the C-plane, but it yields one peak followed by a pronounced shoulder on the R-plane. It is

curious that the density profile for the methyl group shows one peak, albeit wide, on the R-plane, but two peaks (the one closer to the surface much weaker than the other) on the C-plane. This suggests the possibility that excluded-volume effects might frustrate the packing of ethanol within the first adsorbed layer.

The atomic density profiles indicate the formation of a well-defined first adsorption layer of ethanol on both the C- and R- surfaces, with the ethanol methylene groups found at 3.45 Å and 2.65 Å, respectively. The intensity of the density peaks within ~7 Å from the R-plane is in general lower than that of the correspondent peaks found on the C-plane. However, the width of the density peaks on the R-plane is wider than that of the corresponding peaks on the C-plane. By integrating the density along the z direction, we confirmed that the number of ethanol molecules found within the first layer on the two substrates per unit surface area is approximately the same.

The density profiles of Figure 4.3 show evidence for a second layer of ethanol on the C- and R-plane surfaces, formed at vertical positions of 8.55 Å and 7.75 Å, respectively (positions of the density peak for the ethanol center of mass). Within the second layer, on both substrates, the ethanol methyl group is found closer to the surface than all the other groups of ethanol. This is contrary to what is observed on the first layer, where the ethanol hydrogen atoms are closer to the surface than the methyl groups. It is likely that the OH groups of ethanol in the second layer are effectively repelled from the dense layer formed by the methyl groups of ethanol in the first adsorbed layer. The intensities and the widths of the corresponding density peaks observed on the two substrates are comparable, suggesting that the differences on the surface properties are only felt within the first adsorbed ethanol layer.

The atomic density profiles drop to zero between the first and second adsorption peaks on both substrates. These results are consistent with simulation data reported by Cooke et al. [126] and Andoh et al. [125], although these were conducted on calcite and silicon dioxide, respectively.

The atomic density profiles on both surfaces become uniform as the vertical distance approaches 20 Å, suggesting that both alumina substrates perturb interfacial ethanol for up to this distance and that bulk properties are recovered at larger distances. The bulk ethanol density obtained from our simulations is ~ 0.75 g/cm^3, consistent with the simulation data reported by Andoh et al. [125] and ~ 4.5% lower than experimental data at the same thermodynamic conditions 298 K and 1 atm (0.785 g/cm^3) [135].

To quantify the structure of interfacial ethanol in terms of free energy profiles, we calculated the PMF for ethanol as a function of the distance from the surfaces. The results are shown in Figure A.2 of Appendix A. The PMF data, obtained from the density profiles of the ethanol center of mass [126, 136], are consistent with those reported for ethanol on the $(10\bar{1}4)$ plane of calcite [126]. The effective attractive PMF obtained in correspondence to the first adsorbed layer (~-2.7 k_BT and ~-2.1 k_BT on C- and R-plane, respectively) is due in part to the propensity of the ethanol molecules to form hydrogen bonds with the hydroxyl groups available on both surfaces. In correspondence to the depleted layer in between first and second adsorbed layers, our PMF results show a significant repulsive barrier (~6.3 k_BT and ~5.0 k_BT for C-plane and R-plane, respectively). The presence of this significant free-energy barrier suggests that ethanol molecules adsorbed within the first adsorbed layer are rarely able to exchange with molecules further from the surface, as confirmed below.

4.4.2 In-plane Radial Distribution Functions

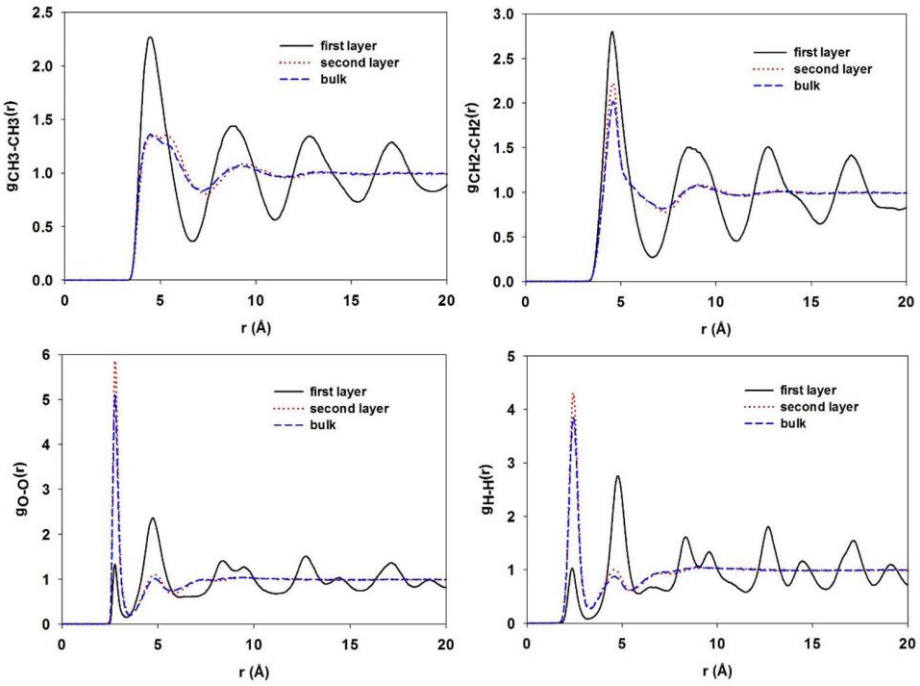

Figure 4.4. In plane CH_3 – CH_3 (top left), CH_2 – CH_2 (top right), oxygen-oxygen (bottom left), and hydrogen-hydrogen (bottom right) radial distribution functions for ethanol molecules within various ethanol layers on the alumina C-plane.

In-plane RDFs were calculated between CH_3 – CH_3, CH_2 – CH_2, oxygen-oxygen, and hydrogen-hydrogen of ethanol molecules to quantify the structural properties within the various adsorbed layers. Results are compared to those obtained in the bulk (i.e., far from the surfaces). For these calculations, following prior algorithms [18], only ethanol molecules found within a given slab parallel to the surface were considered. The thickness (δz) of the slab was 5 Å for the calculations show here. Bulk ethanol is identified as ethanol found at z > 20 Å from the substrates.

In Figure 4.4, the results are presented for in-plane RDFs for ethanol in the first and second layers on the C-plane. Several pronounced peaks are observed in all RDFs within the first layer, suggesting a well-ordered molecular structure. The

results obtained in the second layer, as well as those obtained for bulk ethanol, are indicative of liquid structures with no pronounced order. These results indicate that C-plane alumina only perturbs the first adsorbed layer of ethanol (up to distances shorter than ~6 Å). This is surprising when compared to the results for the polar orientation, discussed in Figure 4.3, which show ordered structure up to ~10-12 Å from the surface.

The most pronounced peak of all in-plane RDFs in the first layer on the C-plane is located at ~5 Å. This distance corresponds to the first peak for $g_{CH3\text{-}CH3}(r)$ and $g_{CH2\text{-}CH2}(r)$, and to the second peak for $g_{OO}(r)$ and $g_{HH}(r)$. The results obtained within the second layer and in the bulk show that the most pronounced peak of the RDFs always corresponds to the first peak (found at 5 Å for methyl-methyl and methylene-methylene RDFs, but at shorter distances for O-O and H-H RDFs). This suggests that while in the bulk both the interactions between methyl and methylene groups and those between the hydroxyl groups are responsible for determining the liquid structure, in the first layer steric effects (dictated by methyl-methyl and methylene-methylene interactions) assume a dominant role. The interactions between the hydroxyl groups of ethanol molecules are not as important as they are in the bulk because, as shown below, such groups interact preferentially with the solid substrate, rather than with other ethanol molecules.

The results for in-plane $g_{CH3\text{-}CH3}(r)$, $g_{CH2\text{-}CH2}(r)$, $g_{OO}(r)$, and $g_{HH}(r)$ for ethanol on the R-plane are shown in Figure A.3 of Appendix A. Despite some differences due to the different packing of ethanol within the first adsorbed layer, the results are consistent with those found on the C-plane.

4.4.3 In-plane Density Distributions

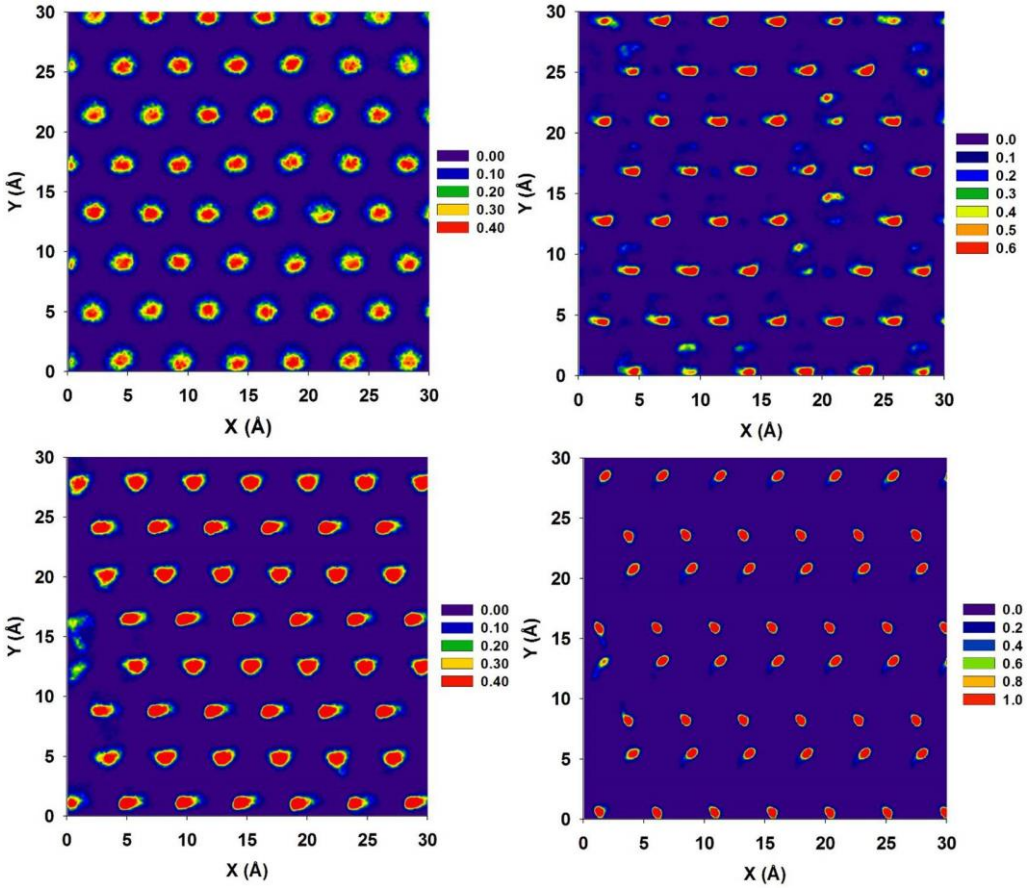

Figure 4.5. In-plane density distributions of CH_3 groups (left panel) and O atoms (right panel) of ethanol molecules within the first adsorbed layer on the α-Al_2O_3 C- (top) and R-plane (bottom). Densities are expressed in $1/Å^3$.

To visualize the organization of adsorbed ethanol molecules, we calculated the in-plane density distributions of methyl, methylene, oxygen, and hydrogen of ethanol molecules within the first adsorbed layer. The results are shown in Figure 4.5 for CH_3 groups (left) and oxygen atoms (right) of ethanol on the C-plane (top panels) and R-planes (bottom panels). The complete sets of results are shown in Figures A.4 and A.5 of Appendix A. In general, on both substrates the in-plane distribution of the methyl groups is representative of the in-plane distribution of CH_2 groups, while that of O atoms is representative of that of H atoms. Because the results above suggest

disordered liquid structure for ethanol molecules within the second layer, only ethanol molecules within the first layer were used for the present calculations.

The results in Figure 4.5 suggest that ethanol molecules occupy specific adsorption sites on each of the alumina surfaces. The resulting structures show high degrees of order, which is consistent with the in-plane RDFs discussed above. Some differences can be observed between the two substrates. On the C-plane the distance between each preferential adsorption site is ~5 Å (consistent with RDF results), whereas the distance between surface hydroxyl groups is ~2.5 Å. It is likely that the size of ethanol molecules prevents them from interacting with all hydroxyl groups available on the substrate. Also on the R-plane the minimum distance between two methyl preferential adsorption sites is ~5 Å. However, next neighboring preferential adsorption sites for O atoms on the R-plane are located at distances of both ~2.5 Å and ~5 Å.

To visualize the structure of the adsorbed ethanol, in Figure A.6 of Appendix A, we report top and side views of representative simulation snapshots obtained for ethanol on the C- and on the R-plane. The snapshots reconcile why the preferential adsorption sites for all ethanol groups on the C-plane yield hexagonal patterns, while on the R-plane CH_3 and CH_2 groups yield hexagonal structures, but O and H atoms do not. These differences are due to different HB networks formed between adsorbed ethanol and the solid substrates, as discussed in the next section.

4.4.4 Hydrogen Bond Network

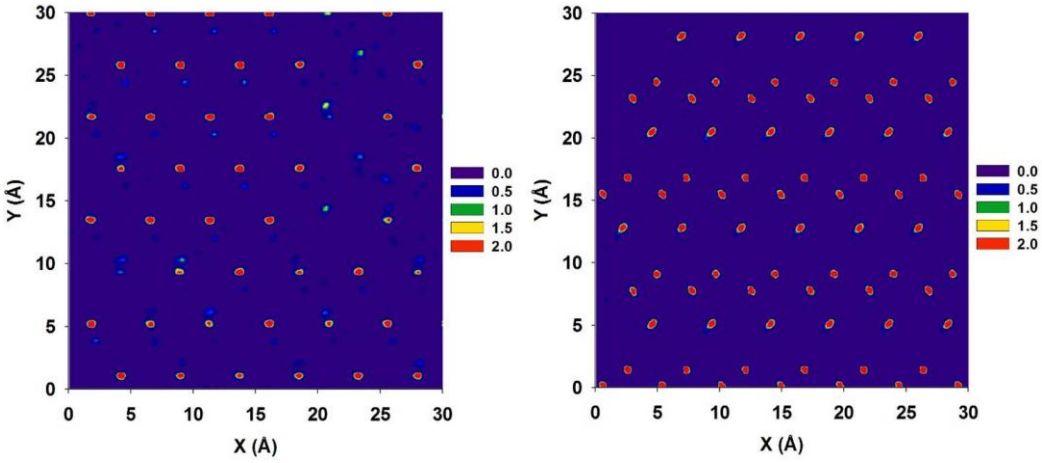

Figure 4.6. In-plane density distribution of hydrogen bonds formed between ethanol molecules in the first adsorbed layer and the hydroxyl groups present on the C- (left panel) and R-plane (right panel). Densities are expressed in $1/\dot{A}^3$.

To relate the distribution of ethanol in the first adsorbed layer to that of the surface hydroxyl groups, we calculated the density distribution of hydrogen bonds formed between the surface OH groups and ethanol on both the C- and R- planes. A geometric criterion was used to identify one hydrogen bond. According to this criterion a hydrogen bond is formed when the angle OH…O is larger than 150º and the O…H distance is between 1.5 Å and 2.1 Å [132-134]. The results, shown in Figure 4.6, suggest that while on the C-plane many surface-ethanol HBs form in locations correspondent to the preferential adsorption of oxygen and hydrogen atoms of ethanol (compare the left panel of Figure 4.6 to the top right panel of Figure 4.5), the same is not necessarily observed on the R-plane (compare the right panel of Figure 4.6 to the bottom right panel of Figure 4.5). Visualizing representative simulation snapshots (Figure 4.7) we confirm that these differences occur because on the C-plane each adsorbed ethanol forms one HB with one surface hydroxyl group. On the R-plane one adsorbed molecule can form one HB with one OH group, but

also two HBs with two neighboring surface OH groups. These OH groups are found in correspondence to two different relative positions with respect to the surface $AlOH_2$ groups.

Our results also show that the density of HBs formed between ethanol and the R-plane (~0.07 H-bonds per A^2) is higher than that of HBs formed between ethanol and the C-plane (~0.05 H-bonds per A^2).

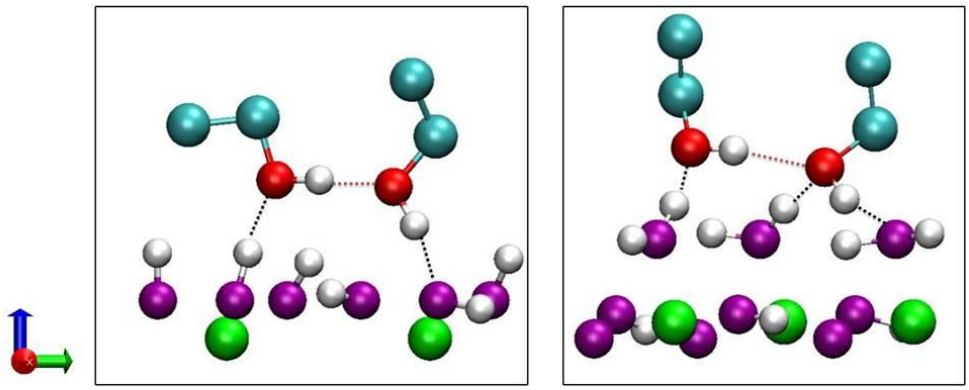

Figure 4.7. Simulation snapshots of selected ethanol molecules in the first adsorbed layer on the C- (left) and the R-planes (right). Only a few atomic surface hydroxyl groups are shown for clarity. The first adsorbed layer of ethanol is defined by those ethanol molecules whose center of mass is found at vertical distances less than 5 Å from the substrate (see density profiles). Cyan, red and white spheres represent alkyl groups, oxygen, and hydrogen atoms of ethanol molecules, respectively. Surface hydroxyl groups are shown with green, purple, and white spheres for aluminum, oxygen, and hydrogen atoms, respectively. Black dot lines represent the H-bonds formed between ethanol molecules and the surface OH groups. Red dot lines represent the H-bonds formed between ethanol molecules. Note that, in agreement with the density profiles, the oxygen atoms of ethanol are found closer to the top-most layer of oxygen atoms of the R-plane (right) than to those of the C-plane (left).

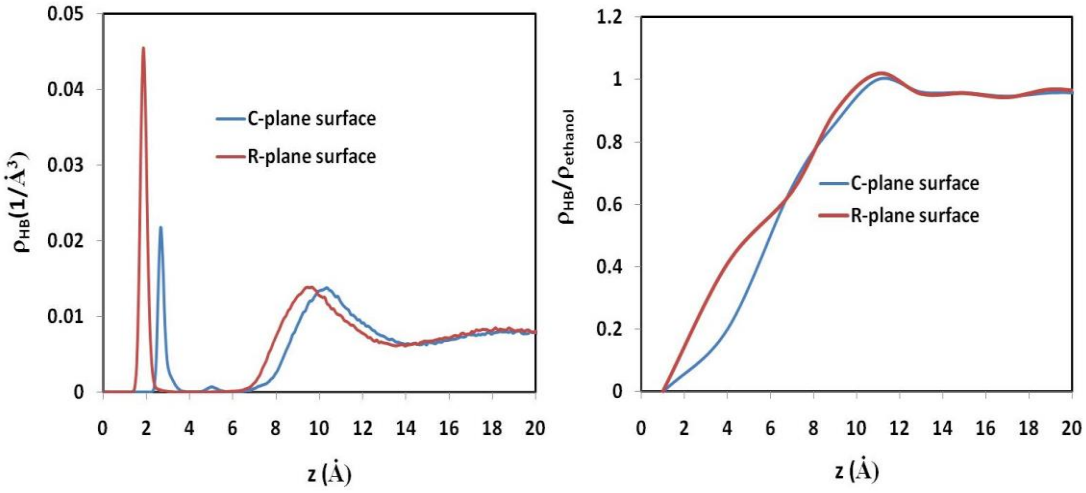

Figure 4.8. Left: Density profiles of ethanol-ethanol hydrogen bonds as function of the distance z from the C- (blue) and R-plane (red). Right: Ratio between the density of ethanol-ethanol hydrogen bonds to that of ethanol molecules as a function of the distance z from both substrates.

In Figure 4.8 we report the density profile of ethanol-ethanol HBs as a function of the distance z from the C- and R-plane. The most important observation is that many ethanol-ethanol HBs form between molecules found in the first layer adsorbed on both substrates (data more evident on the R-plane). This result is at first sight surprising, given the discussion concerning ethanol-surface HBs. However the two-dimensional RDFs (see Figure 4.4) suggest that the position of the first peak in both O-O and H-H profiles are at distances comparable to those observed in the bulk, although their intensity is significantly lower. The simulation snapshots (Figure 4.7) show that the well-ordered ethanol molecules within the first adsorbed layers can form ethanol-ethanol HBs. To quantify the ability of ethanol molecules to form HBs with other ethanol molecules as a function of the distance from the interface, we calculated the ratio between the density of ethanol-ethanol HBs and that of ethanol molecules at each position. The results are shown in the right panel of Figure 4.8. Near both surfaces the ratio is less than 1, and it increases to unity at large separations. We conclude that each ethanol in the bulk form two HBs with other

ethanol molecules (one as donor, one as acceptor), while one out of every three ethanol molecules is engaged via HBs with other ethanol molecules near the R-plane (one out of six near the C-plane). Ethanol molecules within the adsorbed layer prefer to form HBs with the surface OH groups. This behaviour contrasts that of water, for which our simulations on the C-plane suggest the possibility of forming numerous water-water HBs, in addition to water-surface ones [19].

4.4.5 Ethanol Orientation

We computed azimuthal and polar angles of the symmetric axis of the methyl group and of the OH group of each ethanol molecule with respect to the $(1\bar{1}0\bar{1})$ direction and the surface normal $(1\bar{1}02)$ (R-plane), or the (1100) direction and the surface normal (0001) (C-plane), as described pictorially in Figure A.7 of Appendix A. The symmetric axis of the methyl group connects CH_3 and CH_2 in one ethanol molecule.

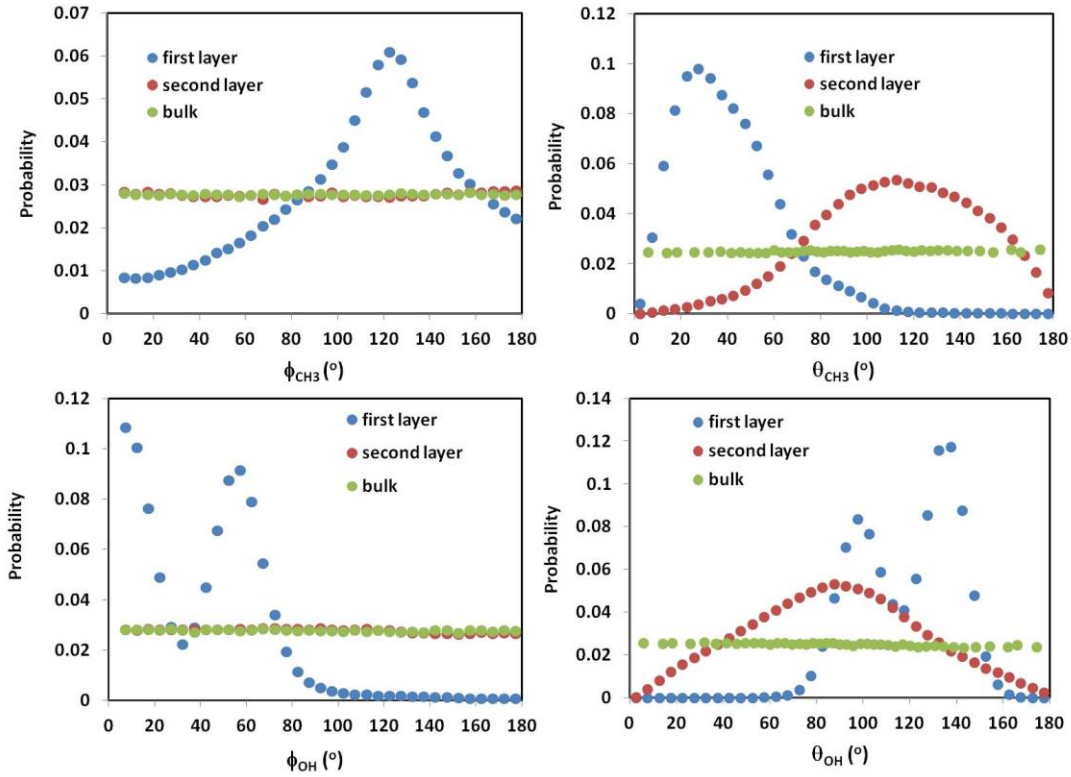

Figure 4.9. Probability distribution for ϕ_{CH3} (top left panel), θ_{CH3} (top right panel), ϕ_{OH} (bottom left panel) and θ_{OH} (bottom right panel) in the first and second layers, as well as in the bulk. ϕ_{CH3} and ϕ_{OH} are the azimuthal angles of the symmetry axis of the methyl CH_3 group and of the OH groups with respect to the $(1\bar{1}0\bar{1})$ direction, respectively. θ_{CH3} and θ_{OH} are the polar angles with respect to the surface normal (see Figure A.7 for schematic).

We begin the discussion with the R-plane, because experimental data are available to validate our predictions. The probability distribution of azimuthal and polar angles for the methyl and the OH symmetry axis are shown in Figure 4.9, top and bottom panels, respectively. We point out that it is difficult to determine the orientation of the ethanol vector $\overrightarrow{OH}$ within the first layer by experimental SFVS, as discussed by Shen et al. [37]. Such information can however be extracted from our simulations to complement the experimental observations. We report the results obtained for ethanol molecules in the first and second adsorbed layers, as well as for bulk ethanol. Ethanol molecules in the first layer orient such that the azimuthal angle

for the symmetry axis of the methyl group is preferentially ~125±5° and the polar angle ~28±5°. These data compare well with the experimental values reported by Shen et al. [37]. These authors employed SFVS to sample the orientation of a monolayer of ethanol at the R-plane – air interface. The results were consistent with azimuthal and polar angles of ~132±8° and ~38±7°, respectively. When the experiments were repeated for liquid ethanol at the R-plane interface, the results still showed a strongly oriented first adsorbed layer with similar orientations (with ethanol orientation consistent with the one observed for the monolayer case) and an ordered second adsorbed layer. Thermal motion was found to affect the second layer much more than the first. Considering that in our simulations ethanol molecules in the first adsorbed layer interact with those in the second layer, agreement with experiments appears satisfactory.

Regarding the orientation of the OH group, in the first layer its azimuthal angle is found to be preferentially ~5° and ~58°, while the polar angle is preferentially ~138° and ~98°. These two peaks are representative of the two structures of ethanol-surface HBs, shown in Figure 4.7.

The azimuthal orientation of both methyl and OH groups of ethanol molecules in the second adsorbed layer is similar to that found in the bulk. However, the polar orientation of the symmetry axis of the methyl CH_3 group with respect to the surface normal $(1\bar{1}02)$ in the second layer shows preference for a polar angle at ~113°. The polar orientation of the OH group in the second layer is also different compared to that found in the first adsorbed layer. These differences reflect the fact that ethanol molecules in the first adsorbed layer project their OH group toward the surface, while those in the second layer project the OH group away from the surface, as discussed above (see Figure 4.3).

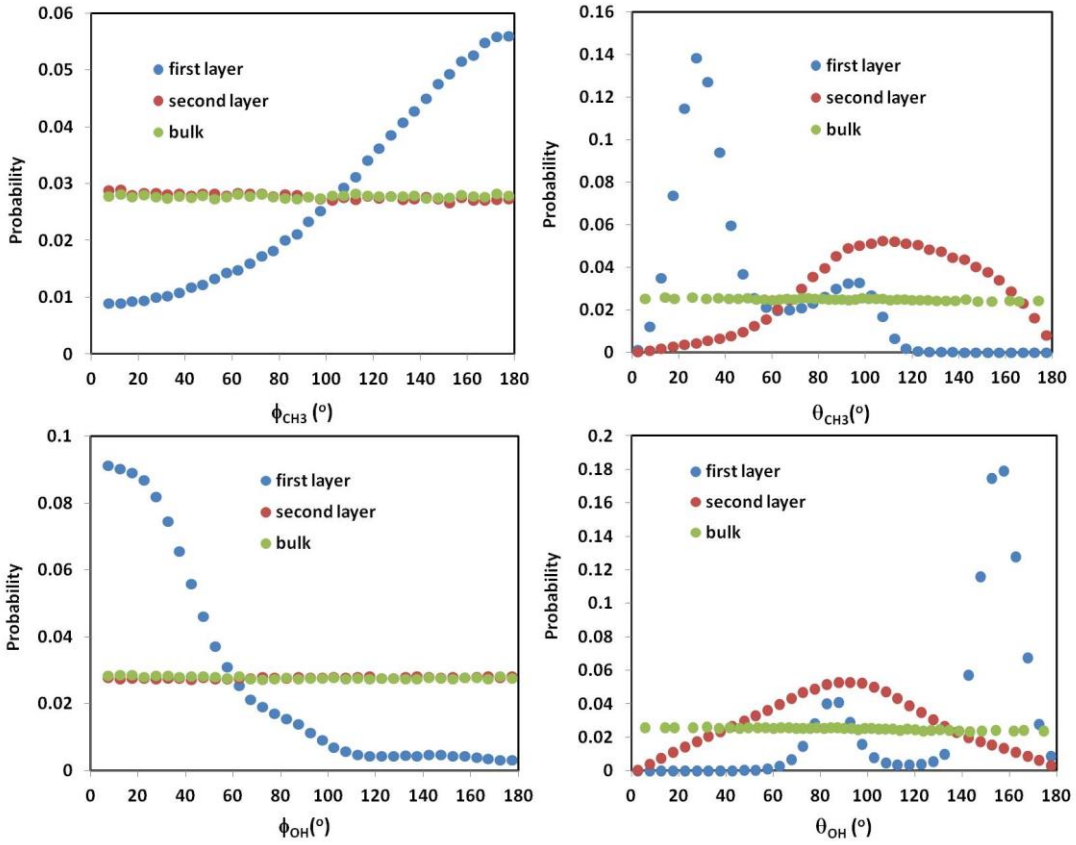

Figure 4.10. Same as Figure 4.9, for ethanol on the C-plane.

In Figure 4.10 we present the results for the orientation of ethanol molecules adsorbed on the C-plane. Different orientations compared to those discussed on the R-plane are clearly evident. For example the symmetry axis of the methyl groups in the first layer preferentially point along the backward direction with respect to the (1100) vector. The probability distribution for the polar orientation of the methyl symmetry axis for ethanol in the first layer shows two preferential orientations, ~28° and ~98°. Consistent with the density distributions of Figure 4.3, these data suggest that the symmetry axis of the methyl group points away from the C-plane, with a slight probability of maintaining the methyl symmetry axes parallel to the substrate. Ethanol molecules in the second layer do not show a preferential azimuthal

orientation for the methyl symmetry axis, while the polar angles show a preference at ~113°.

Results for the preferential orientation of the $\overrightarrow{OH}$ vector of ethanol suggest that also on the C-plane this vector either points toward the surface or remains approximately parallel to it. The results obtained in the second layer suggest a different orientation, with many OH bonds parallel to the surface. These data are similar to those obtained on the R-plane.

4.4.6 Dynamical Properties

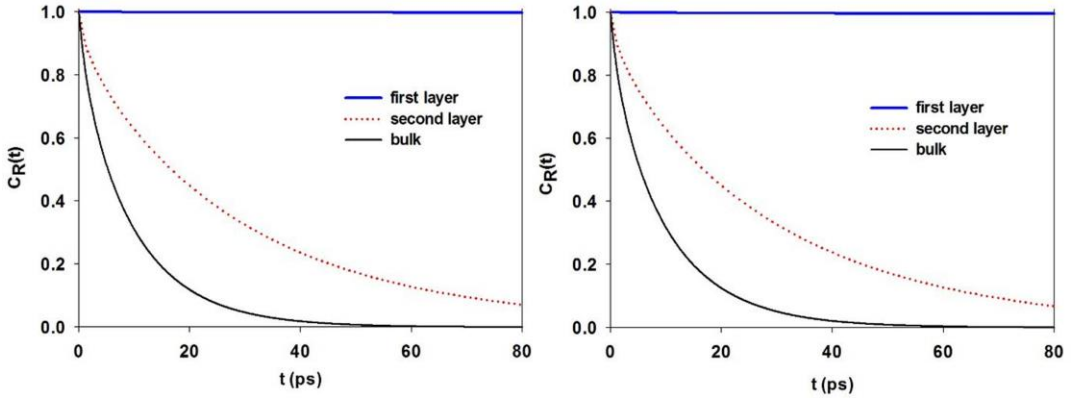

Figure 4.11. Residence autocorrelation functions $C_R(t)$ for the methylene group of ethanol molecules within the first (blue solid curve) and second adsorbed layers (red dot curve). Data obtained in the bulk are shown for comparison (black solid curve). Results are shown for ethanol on the C-plane (left panel) and on R-plane (right panel), respectively.

To quantify how long ethanol molecules remain in contact with the alumina surfaces, we computed the residence autocorrelation function $C_R(t)$ within first and second adsorbed layers (for a discussion on the method, see ref. [31]). The faster the autocorrelation function decays to 0, the shorter ethanol molecules stay in a specific hydration layer. The thickness of one layer was considered to be 5 Å. For comparison, we also computed the residence autocorrelation function for ethanol molecules in a layer far from the surface (i.e., 'bulk ethanol'). We computed $C_R(t)$

for methyl, methylene, oxygen, and hydrogen belonging to ethanol. The results were statistically identical, and only results for CH_2 are shown in Figure 4.11. In the left and right panels we show results obtained on the C- and R-plane, respectively.

The results suggest that ethanol molecules adsorbed in the first layer do not leave either substrate within the 80 ps of the analysis ($C_R(t)$ was calculated in the first layer on both substrates for up to 2 ns, and very slow decay was observed). The ethanol molecules in the second layer are much more mobile compared to those in the first layer, but they show a much longer residence time than ethanol molecules in the bulk. Based on results for density profiles and surface-ethanol PMF, it was expected that ethanol molecules would remain in contact with the two substrates for very long times. It was however not obvious that ethanol molecules in the second layer would also show reduced exchange rate with ethanol molecules in the bulk. This might be due to the fact that ethanol molecules in the first adsorbed layers provide a very tight structure, on which ethanol molecules form a second adsorbed layer.

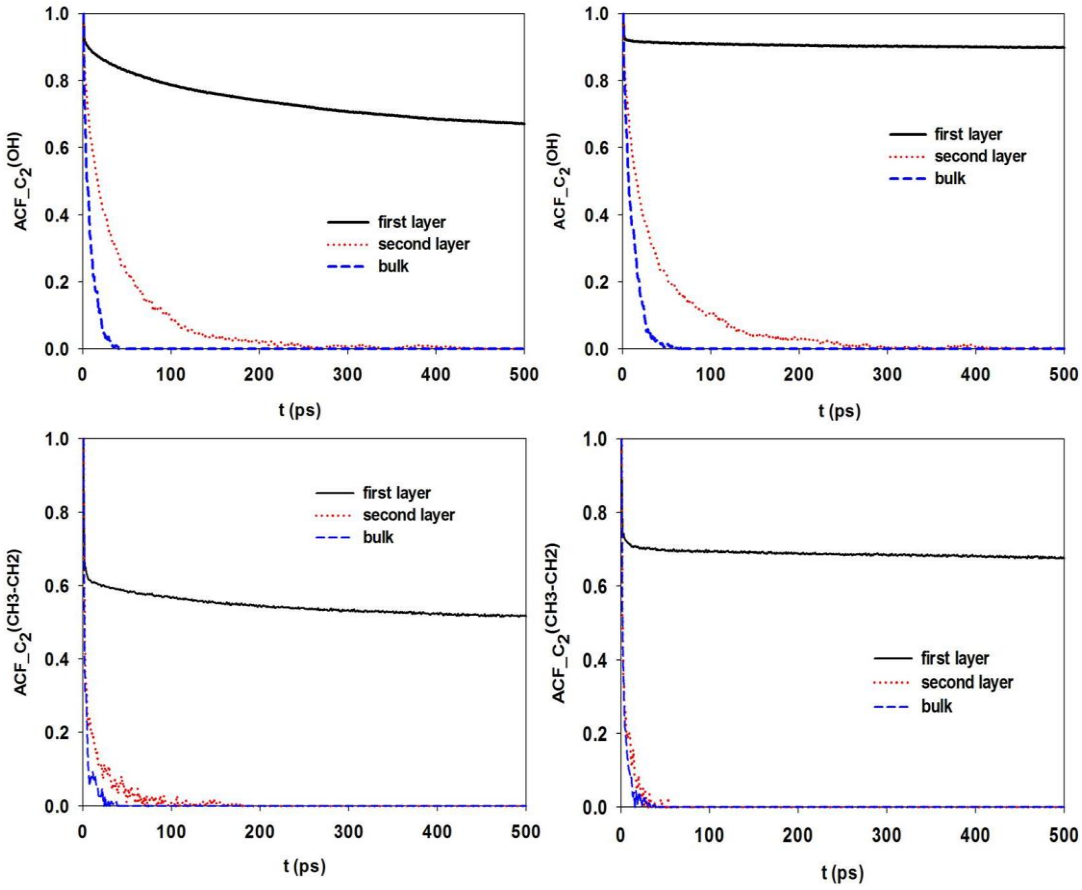

Figure 4.12. *Top:* Reorientation autocorrelation functions for OH group of ethanol molecules within the first (black solid curve) and second adsorbed layers (red dot curve). *Bottom:* Reorientation autocorrelation functions of the symmetry axis of the methyl CH_3 group of ethanol molecules within the first (black solid curve) and second adsorbed layers (red dot line). Results obtained on the C- and R-planes are shown in the left and right panels, respectively. Results for bulk ethanol are shown for comparison (blue dashed curve).

To quantify the rotational dynamics of ethanol molecules as a function of the distance from the substrate, we calculated the reorientation autocorrelation function [17]:

$$C_v(t) = \frac{\langle v(t)v(0)\rangle}{\langle v(0)v(0)\rangle} \qquad (4.1)$$

In eq. (4.1) ν is either the vector $\overrightarrow{OH}$ or the symmetric axis of the methyl group of one ethanol molecule. The faster the ACF decays to zero, the more quickly

ethanol molecules change their orientation. Ethanol molecules in the first and second adsorbed layers are considered and compared in Figure 4.12 to results obtained for bulk ethanol. The results are shown for ethanol on the C- (left) and R-plane (right). As expected, on both surfaces our results suggest that ethanol molecules in the first layer rotate more slowly than those in the second layer and much more slowly than those in the bulk. We note that in the first layer the symmetry axis of methyl group changes its orientation faster than the vector $\overrightarrow{OH}$. This is due to the HBs between ethanol and the surfaces, which are difficult to break and thus slow down the OH rotation. We also note that both rotational ACFs for ethanol in the first adsorbed layer on either substrate decay much faster than the residence autocorrelation function in Figure 4.11. This suggests that HBs form and break more frequently than ethanol molecules leave the first adsorbed layer.

Both rotational ACFs decay more slowly for ethanol molecules within the first adsorbed layer on the R-plane than on the C-plane. This is probably related to the higher density of ethanol-surface HBs detected on the R-plane. Results on the second layer are not significantly different on the two substrates.

Although the structure of ethanol molecules in the second adsorbed layer is for the most part similar to that observed for bulk ethanol (except for its preferential orientation), results for the dynamics show that the residence time of ethanol molecules within this layer is much longer than that in the bulk, and that the orientational diffusion is slightly slower than that observed in the bulk.

4.5 Conclusions

Molecular dynamics simulations were conducted to study structure and dynamics of liquid ethanol within thin films supported on the C-plane and R-plane alumina surfaces under ambient conditions. The results show that ethanol molecules

in the first adsorbed layer have a pronounced order, reflecting the structure of the substrates and the possibility of forming hydrogen bonds with the surface OH groups. A significant orientational order is observed within the first adsorbed layer on both surfaces with the methyl groups preferentially projecting toward the bulk and the OH groups forming hydrogen bonds with both the solid substrates and other ethanol molecules (to a much lesser extent). The preferential orientation of ethanol molecules within the first adsorbed layer on the R-plane is consistent with experimental sum frequency vibrational spectroscopy data. Also consistently with experiments, we found that ethanol molecules show some order within the second adsorbed layer, but to a much lesser extent compared to results obtained for ethanol in the first adsorbed layer on both C- and R-planes. Our results suggest that those molecules in the first adsorbed layer seldom leave, and that their rotational diffusion is hindered compared to bulk values, probably because of preferential hydrogen bonds with the substrates. As suggested by Catalano et al. [137-139] in the case of water, our results can be explained by the formation of a complex hydrogen-bonded network between adsorbed ethanol and the supporting solid substrates. The results presented here could be useful to advance our understanding regarding the behaviour of hydrogen-bonding and amphiphilic molecules in contact with materials of both technological and geological importance. Applications that could benefit from this understanding include industrial, geophysical, petroleum, and environmental ones.

Chapter 5 Preferential Adsorption from Liquid Water-Ethanol Mixtures in Alumina Pores

The material presented in this section was published in 2014 in volume 30, pages 8066-8077 of Langmuir.

5.1 Abstract

The sorptivity, structure and dynamics of liquid water-ethanol mixtures confined in alumina pores were studied by molecular dynamic simulations. Due to an effective stronger attraction between water and the alumina surface, our simulations show that water is preferentially adsorbed in alumina nanopores from bulk solutions of varying composition. These results are in good qualitative agreement with experimental data reported by Rao and Sircar (*Adsorpt. Sci. Technol.* **1993**, 10, 93). Analysis of the simulated trajectories allows us to predict that water diffuses through the narrow pores more easily than ethanol, in part because of its smaller size. Our results suggest that ethanol has an anti-plasticization effect on water within the narrow pores considered here, whereas it has a plasticization effect on water in the bulk. Rao and Sircar suggested that alumina could be used in concentration swing and/or concentration-thermal swing adsorption processes to separate water from ethanol. In addition, our results suggest the possibility of using alumina for manufacturing permselective membranes to produce anhydrous ethanol from liquid water-ethanol solutions.

5.2 Introduction

Aqueous mixtures of alcohols are prevalent hydrogen-bonding fluid mixtures. They can be applied as water-based fracturing fluids to stimulate subsurface formations in the practice of hydraulic fracturing; they might reduce fracturing fluid

leak off and enhance fluid recovery [4]. The recent push for ethanol as an additive to gasoline in the United States has focused community interest in the production of anhydrous ethanol [42, 43]. In fact, water is always present in ethanol produced from the fermentation of biomass, and it is also found in ethanol produced via the catalytic hydration of ethylene. Traditional distillation processes are problematic because ethanol and water yield an azeotrope at the 89.4:10.6 molar ratio, 78.2°C, and 1 atm pressure [44] (azeotropic distillation is required, which is energy intensive [45]). Among alternative processes [46], the advent of molecular sieves has rendered feasible the implementation of membrane-based separations, which allow selective removal of water from water-ethanol mixtures. Zeolites are often used for these applications. For example, membranes based on zeolite 3A are widely employed industrially [47]. One can use hydrophobic zeolites, such as silicalite, or hydrophilic ones, such as NaA, depending on whether ethanol or water permselectivity is required, respectively. Molecular simulations can be used for better understanding these processes. Yang et al. [140] employed grand canonical Monte Carlo (GCMC) and NVT MD techniques to study the preferential adsorption and diffusion from a water-ethanol gaseous mixture in a silicalite crystal. The results were consistent with the experimentally observed selective adsorption of ethanol [48, 49]. Kuhn et al. [141] studied the adsorption and diffusion of water and ethanol in all-silica DD3R zeolites. Their experiments and simulations suggested that the ability of the material to separate water from ethanol is due to the fast diffusivity of water through the porous matrix. Zhang and Liu [142] recently reported that a membrane based on NaA zeolites shows excellent performance for the removal of water from water-ethanol mixtures. Although many studies focused on the separation of water from ethanol using various membranes based on zeolites [47, 50, 140-142], polymers [51,

52], etc., little is known about the molecular structure and dynamics of water-ethanol mixtures within the pores present in these materials. Understanding how confinement affects preferential adsorption, structure, and dynamics of water-ethanol mixtures might lead to the design of membranes that yield improved selective separation while requiring a milder pressure drop than zeolite-based membranes. For these studies to be effective, it would be desirable to compare the properties of the confined systems to those observed for bulk fluids. Some studies have been reported for liquid water-ethanol mixtures in the bulk. Wensink et al. [114] investigated alcohol and water mixtures to determine the relation between transport properties at the molecular (diffusion and rotational mobility) and macroscopic (viscosity) levels. Mejia and coworkers [143] employed quantum chemical topology (QCT) and MD simulations to study water-ethanol clusters near the azeotropic composition.

In this study, we employ equilibrium MD simulations to examine the preferential adsorption of water-ethanol mixtures in 1 nm slit-shaped hydroxylated α-Al_2O_3 pores under ambient conditions from bulk liquid mixtures. This system was chosen because Rao and Sircar showed experimentally that alumina can preferentially adsorb water [144], and because we have conducted prior simulations for both liquid water and liquid ethanol in contact with an alumina substrate that appear to be consistent with experimental data [19, 37, 144, 145]. We investigate here the structural and dynamical properties of ethanol and water under confinement as opposed to in the bulk to understand the transport mechanisms in the pores and quantify the potential application of porous alumina as membrane materials for producing anhydrous ethanol.

In the remainder of this paper, we first describe the simulation model and algorithms, we discuss our results, and we then summarize the main observations obtained from our atomistic modeling effort.

5.3 Simulation Methodology

Alumina pore surfaces were modelled as crystallographic faces of sapphire α-Al_2O_3 (space group $R\bar{3}c$) – C-plane (0001) [98]. Within our simulation box, two alumina slabs were considered, facing each other along the Z direction to represent a slit-shaped pore. The slit shape is a realistic pore geometry for alumina pores [146-148]. All the nonbridging oxygen atoms were protonated to obtain a chemically realistic surface [128]. The surface area of each slab is 91.35×90.6845 $Å^2$ (X – Y plane). The simulation box is periodic in the X, Y, and Z directions. The Y dimension of the simulation box reflects the periodicity of the solid crystalline substrate (90.6845 Å). The X and Z dimensions were set to ~400 Å and 33.82 Å, respectively. The large X size allows for the formation of a 'bulk' phase far from the solid material. Along the X direction we allow for the formation of a vacuum of ~200 Å width. This allows us to maintain the pressure in the liquid system at near ambient conditions. The Z dimension is chosen to allow for the formation of a slit pore of width 10 Å (the pore width refers to the center-to-center distance between surface hydroxyl oxygen atoms of the two alumina slabs across the pore). It is known that both pore geometry and pore size strongly impact structural and dynamical properties of confined fluids. The width of 10 Å is chosen in this work because it is large enough for both ethanol and water to enter the pore, which allows us to examine the competitive adsorption and differential diffusion of ethanol and water inside the pore. Due to periodic boundary conditions, the alumina slit pores are effectively infinite along the Y direction. Simulations were carried out for six

mixtures at water/ethanol composition of 10/90, 20/80, 30/70, 50/50, 70/30, and 80/20 (mol/mol). The total number of molecules was constant for all systems. The number of water and ethanol molecules used in each simulation is listed in Table 5.1. All simulations were initiated by conducting short runs in which liquid ethanol was the only component. These simulations were conducted to fill the pores with ethanol. After these systems approached equilibrium, water molecules were added into the bulk volumes, in the desired amount.

The CLAYFF force field [65], the OPLS-UA [66], and the rigid SPC/E model [67] were implemented to describe the alumina pore, ethanol, and water, respectively. Non-bonded interactions were modelled by means of dispersive and electrostatic forces. The electrostatic interactions were modelled by the Coulombic potential. Dispersive interactions were modelled with a 12-6 Lennard-Jones potential. The Lennard-Jones parameters for unlike interactions were determined by the Lorentz-Berthelot combining rules [64] from the values of like components. The cutoff distance for all interactions was set to 9 Å. Long-range corrections to electrostatic interactions were treated using the PME method [94].

All simulations were performed in the canonical ensemble NVT where the number of particles (N), the simulation volume (V), and the temperature (T) were kept constant. The simulated temperature was held at 298 K and controlled by a Nosé-Hoover thermostat [95, 96] applied to all components with a relaxation time of 100 fs. Building on prior results, only hydrogen atoms of pore surface hydroxyl groups were allowed to rotate, whereas all other atoms of alumina pores were kept rigid. The equations of motion were solved by implementing the leapfrog algorithm [97] with 1.0 fs time steps. The simulation package GROMACS [68, 131] was used for performing the simulations. The total simulation time was 300 ns for each

system. Data analysis was conducted over the last 20 ns of the simulations, after 280 ns of equilibration were completed. These long simulations were required to equilibrate the systems. Equilibration was considered achieved when the densities of water and ethanol within the pore remained constant. We also conducted additional simulations in which water molecules were preadsorbed inside the alumina pores and ethanol molecules were in the bulk. We confirmed that the final configurations were consistent with those obtained when a different initial configuration was used, strongly suggesting that the results presented are representative of equilibrated systems. In Figure 5.1 we report the side view of the alumina pore in contact with 20/80 (mol/mol) water/ethanol mixture at 298K after the system reached equilibrium. Although water molecules were added to the bulk liquid, they were found to gradually substitute for ethanol previously adsorbed in the alumina pore. This suggests that water is more favourably adsorbed in the alumina pores considered here than ethanol. To better understand the results obtained when the liquid mixtures are in contact with the alumina pores, we conducted a few simulations for fluids on one freestanding alumina surface.

Table 5.1. Number of water and ethanol (EtOH) molecules per each system simulated.

System	**Water/EtOH (mol/mol)**	**Number of Water Molecules**	**Number of Ethanol Molecules**
I	10/90	500	4500
II	20/80	1000	4000
III	30/70	1500	3500
IV	50/50	2500	2500
V	70/30	3500	1500
VI	80/20	4000	1000

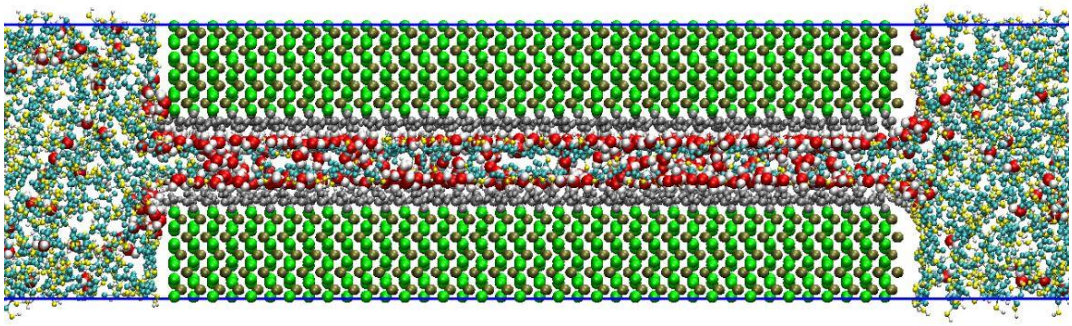

Figure 5.1. Representative simulation snapshot for the 20/80 (mol/mol) water/ethanol mixture in contact with the protonated α-Al_2O_3 alumina pore at 298K. Red and white spheres represent oxygen and hydrogen atoms in water molecules, respectively. Cyan, yellow, and white spheres represent alkyl groups, oxygen, and hydrogen atoms in ethanol, respectively. Green, tan, and silver spheres represent aluminum, oxygen atoms, and hydroxyl groups in alumina, respectively. Water molecules are enlarged for clarity.

5.4 Results and Discussion

5.4.1 Liquid Mixtures in Contact with Freestanding Alumina

To understand if water molecules can displace ethanol molecules within the α-Al_2O_3 (0001) pores even when ethanol is already adsorbed, as suggested by the snapshot of Figure 5.1, we calculated the isosteric heat of adsorption for ethanol and water on a freestanding alumina surface at infinite adsorbate dilution (i.e., the isosteric heat of adsorption in the Henry's law region). The algorithm implemented is explained in detail in Appendix B. The calculated heat of adsorption for water on alumina at 298K (52.12 kJ/mol) is much higher than that obtained for ethanol (29.17 kJ/mol), confirming that the alumina surface effectively attracts water molecules much more strongly than it does ethanol molecules. Note that our results for water on alumina are consistent with those reported by Kittaka et al. [149] for water on the hydroxylated C-plane of α-Al_2O_3. Our estimates are also in good agreement with the

experimental heat of adsorption reported by Rao and Sircar for water on alumina in the Henry's law region (54.39 kJ/mol) [144].

Because gas phase results can differ from results in condensed phases, we also calculated the effective PMF as a function of the distance between one molecule and the α-Al_2O_3 (0001) surface. We considered one water molecule as it approaches the alumina surface covered by ethanol (system A), one water molecule as it approaches the alumina surface covered by ethanol and a few water molecules already adsorbed on alumina (system B), and one ethanol molecule as it approaches the alumina surface covered by water (system C). Details about the method for PMF calculations are illustrated in Appendix B. The PMF results for systems A and C (illustrated in Figure B.1 of Appendix B) indicate that as the various molecules approach the surface they encounter a relatively large free-energy barrier before they adsorb on the surface. Once they adsorb on the surface, the PMF exhibits a minimum, which depends on the system. The depth of the free-energy well corresponding to adsorption for systems A and B (~-1.4 and ~-1.8 kcal/mole, respectively) is much larger than that obtained for system C (~-0.01 kcal/mole). This suggests that water is preferentially adsorbed on alumina. The PMF obtained for system B is more attractive than that obtained for system A. This is likely due to the formation of HBs between the water molecule approaching the surface and the water molecules already adsorbed on it. The large energy barrier encountered for the molecules to adsorb suggests that, once water molecules are adsorbed on alumina, they tend not to desorb. Comparing the free-energy barrier obtained for systems A and B, our results suggest the free-energy barrier is much lower when a few water molecules are already adsorbed on alumina. This suggests that the rate-limiting step for water adsorption on an ethanol-covered alumina corresponds to the adsorption of the first

few water molecules, after which adsorption proceeds very fast, and the entire alumina surface can be easily covered by water. We do not dwell further along this qualitative analysis, as this paper is focused on alumina pores.

5.4.2 Liquid Mixtures in Contact with Narrow Alumina Pores

5.4.2.1 Selective Adsorption of Water

In Table 5.2 we show the overall molar ratio of water and ethanol for the various systems investigated in which a liquid mixture was in contact with the 1 nm – wide alumina pore. In the same table we also report the simulation results for the molar composition in the bulk and within the pore after equilibrium has been reached for the six systems investigated. In all cases our results show that water preferentially adsorbs within the pore. For the dehydration of ethanol, it is worth pointing out that the equilibrium partition can yield a bulk mixture of composition beyond the azeotropic point (9/91) when the overall system composition at the beginning of the simulation is below this point (20/80). As this preferential adsorption renders azeotropic distillations not necessary, our results suggest that the use of alumina pores as an adsorbent could aid the dehydration of ethanol at ambient conditions (298K).

Table 5.2. Overall system composition (ratio of water to ethanol molecules), composition of the bulk phase after 280 ns of simulation, and composition of the liquid mixture inside the alumina pore. Simulations conducted at 298 K.

System	Overall System Composition (water to ethanol molecular ratio)	Bulk Mixture Molecular Composition After Adsorption	Molecular Composition of the Confined Mixture
I	10/90	6/94	32/68
II	20/80	9/91	60/40
III	30/70	12/88	82/18
IV	50/50	24/76	95/5
V	70/30	51/49	98/2
VI	80/20	68/32	99/1

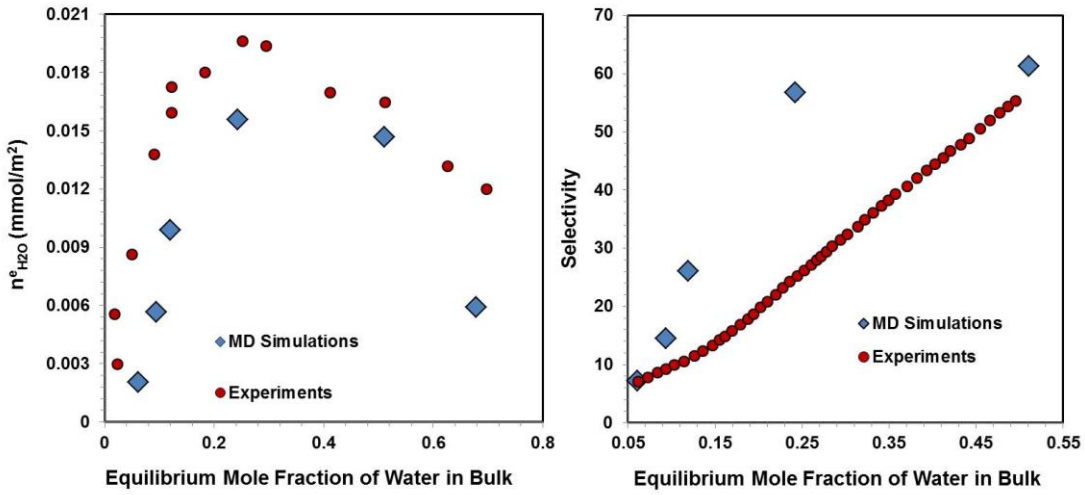

Figure 5.2. (Left) Equilibrium surface excess of water for the liquid ethanol – water mixtures adsorbed within the simulated alumina pore. (Right) Selectivity of water adsorption over ethanol. Different symbols are for different data sets. The results from the present simulations at 298K are shown as blue diamonds, those from experiments [144] at 303 K as red circles.

To facilitate comparison against experiments, in the left panel of Figure 5.2 we present the surface excess of water within the simulated alumina pore at 298 K as a function of the composition of the water-ethanol mixture after adsorption has reached equilibrium. Following Matranga et al. [150, 151], the water surface excess is defined as:

$$n^{e}_{H2O} = \frac{N_{pore} - V_{pore}\rho_{bulk}}{S} \quad (5.1)$$

In eq. (5.1), n^{e}_{H2O} is the equilibrium surface excess of water; N_{pore} is the number of water molecules adsorbed inside the pore; V_{pore} is the volume of the alumina pore; ρ_{bulk} is the equilibrium bulk density of water in the equilibrated water-ethanol mixture; S is the surface area of the adsorbent (the surface area for our simulated system is ~ 166 nm^2, while the specific surface area of the activated alumina used in Rao's works, Alcoa H152, is ~176 m^2/g [152]). Note that although eq. (5.1) focuses on the surface area of the adsorbent, all molecules within the pore volume are used for the calculation. As the pore used in our simulations is only 1 nm in width, it can be argued that most of the water molecules present within it are interacting with the alumina surfaces. Should the pores be wider, water molecules near the center of the pore are likely not to interact with the surfaces. To reconcile experimental and simulated data, we considered experimental values per gram of porous adsorbent, knowing that the specific pore volume for the materials used by Rao and Sircar was ~ 0.666 cm^3/g [144].

As shown in Figure 5.2, left, the simulated surface excess of water obtained in this study shows a trend similar to that of the experimental data reported by Rao and Sircar [144]. Although the agreement is not quantitative, both simulated and experimental curves show a maximum in surface excess at mole fraction $x \approx 0.25$. It

is noted that the surface excess predicted by our simulations is in general lower than that reported experimentally (compare, for example, the maximum surface excess, which is ~0.015 mmol/m^2 in the simulations and ~0.020 mmol/m^2 in the experiments). Because our simulations suggest that the preferential adsorption of water within the alumina pore is a phenomenon driven by preferential surface-water interactions, it is possible that the difference between experimental and simulated results in excess water adsorption is due to the available specific surface area of alumina adsorbent, which is much smaller in our simulations (α-alumina) than in the experiments (γ-alumina). The different surface densities of OH groups (larger in α-alumina) certainly contribute to the differences seen in Figure 5.2. Despite these differences, however, it is encouraging that both experimental and simulated results, when expressed in the form of excess surface adsorption of water, consistently show an inverted asymmetric U shape. Water is selectively adsorbed within the alumina pores, in particular on the alumina surfaces, at all bulk compositions.

We also calculated the selectivity of water adsorption, defined as [151, 153]:

$$S = \frac{x^a_{H2O}}{x^a_{EtOH}} \cdot \frac{x_{EtOH}}{x_{H2O}} \tag{5.2}$$

In eq. (5.2) x^a_{H2O} and x^a_{EtOH} are the mole fractions of water and ethanol, respectively, in the adsorbed phase (inside the pore) at equilibrium and x_{H2O} and x_{EtOH} are the corresponding equilibrium bulk mole fractions. The results from our simulations are shown as blue tilted squares in the right panel of Figure 5.2. Because experimental data are available in the range of water mole fractions less than 0.5, we only show results obtained when the equilibrium bulk water concentration x_{H2O} is < 0.52. When compared to results reported experimentally for zeolite A, which can yield water adsorption selectivity as high as 10,000 [142, 154, 155], our simulations

only show moderate selectivity for water adsorption. However, our data are qualitatively comparable to the experimental data reported by Rao and Sircar (also shown in Figure 5.2). Both experimental and simulated data show that selectivity increases with bulk water mole fraction. Our results are in quantitative agreement with experiments at low bulk water mole fractions ($x_{H2O} < 0.07$), but increase much faster as the bulk water mole fraction increases. As will be discussed in detail below, our simulations suggest that water adsorption selectivity is due to preferential water adsorption on the alumina surfaces. The discrepancy between simulated and experimental data in the right panel of Figure 5.2 is probably due to the fact that the pores used for our simulations are much narrower and because of the differences in surface properties (the pores used in our simulations are crystalline, while those used in the experiments are amorphous). Note that preliminary simulation results on pores of width 0.6 nm (not shown here for brevity) showed an even more pronounced enrichment of water in the confined phase, which is due in large part to the exclusion of ethanol from such narrow pores. Overall, the comparison between experiments and simulations shown in Figure 5.2, combined with the analysis of the equilibrium structure of water-ethanol mixtures within the pores (next section), suggests that porous alumina materials composed of smaller pores could be the most effective in dehydrating ethanol. Our results also suggest that the selectivity reaches a plateau (in our simulations achieved when $x_{H2O} \approx 0.25$). This is probably an artifact of our simulations, and it is due to the fact that the pore considered in our case becomes almost completely filled with water at these conditions.

5.4.2.2 Structural Properties of the Confined Liquid Mixture

5.4.2.2.1 Atomic Density Profiles

We focus on the four systems I, II, III and IV (see Table 5.1 for system composition) for analysis of structural and dynamical properties of ethanol and water molecules confined inside the pore.

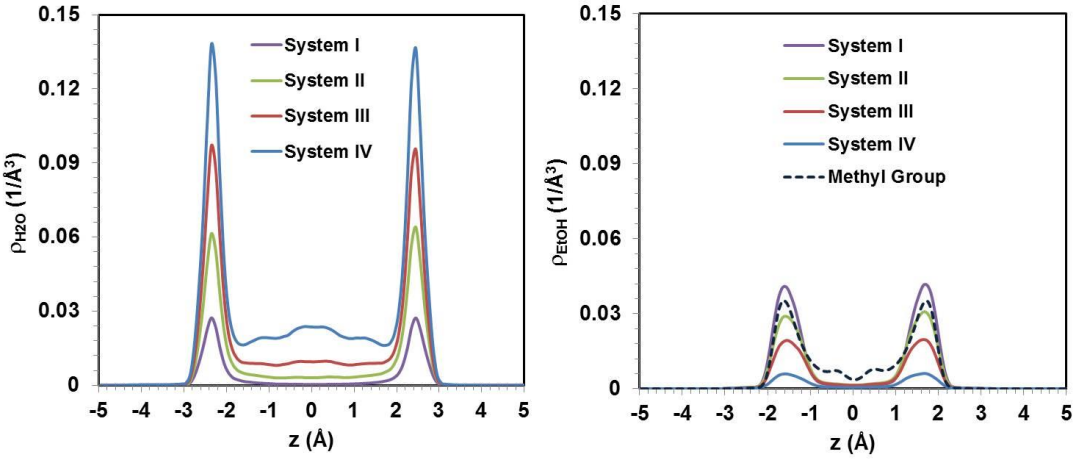

Figure 5.3. Density profiles of water oxygen (left) and ethanol methylene group (right) as a function of the distance z across the alumina pore for simulated systems I, II, III, and IV. The dark blue dashed curve in the right panel represents the density profile for the methyl group of ethanol for system I. The reference (z = 0) corresponds to the center of the pore.

In Figure 5.3 we report the atomic density profiles of water oxygen (left) and of ethanol methylene group (right) as a function of the vertical distance Z across the alumina pore. The results are shown for simulated systems I, II, III, and IV at increasing water content. For comparison, in the right panel we also report the density profile obtained for the ethanol methyl group corresponding to simulated system I (dark blue curve). In this figure the reference z = 0 corresponds to the center of the pore. The planes of oxygen atoms formed by the surface hydroxyl groups of the bottom and top pore alumina surfaces are located at -5 Å and +5 Å, respectively. Visual comparison of the data shown in the left and right panels of Figure 5.3

confirms, as expected, that as the water content increases inside the pore, the amount of ethanol decreases. However, the structural distribution of water and ethanol molecules across the pore volume does not seem to depend significantly on the composition of the fluid mixture, within the conditions explored in our simulations. Explicitly, water molecules clearly form hydration layers in contact with each of the two pore surfaces (note the peaks in the oxygen density profiles, located at approximately -2.35 Å, near the bottom surface, and at approximately +2.45 Å, near the top surface). Water molecules can also be found in the center of the pore, but only when the water mole fraction is above 0.6. At the highest water content considered, the density profiles shown in the left panel of Figure 5.3 suggest that water molecules yield an enriched zone near the center of the pore. However, this enrichment is not very pronounced.

The results for the density profiles of methylene groups of ethanol (right panel in Figure 5.3) suggest that ethanol molecules form two layers within the pores simulated here. The peaks of the density appear at positions -1.65 Å and +1.65 Å, symmetric with respect to the pore center. The density profiles for the methyl groups of ethanol, which we report only for system I for clarity (dashed curve in the right panel), can be used for estimating, qualitatively, the orientation of the ethanol molecules with respect to the alumina surface. Because the maxima in the density profiles for the methylene groups correspond to those for the methyl groups, our results suggest that ethanol molecules orient with the symmetry axis of the methyl group parallel to the pore surfaces. This is not consistent with the simulations of liquid ethanol on a free-standing alumina surface, wherein ethanol molecules point the symmetry axis of the methyl group out of the surface (~28° with respect to the surface normal) [145]. This difference is due primarily to the small pore width

considered in the present work, which does not allow for the ethanol molecules adsorbed on both pore surfaces to adopt the configuration most favourable on a free standing surface. It is possible that, because of this conformational constraint, water molecules are more favourably adsorbed within the narrow pore than they would be on a freestanding surface, when compared to ethanol molecules.

5.4.2.2.2 Hydrogen Bonding

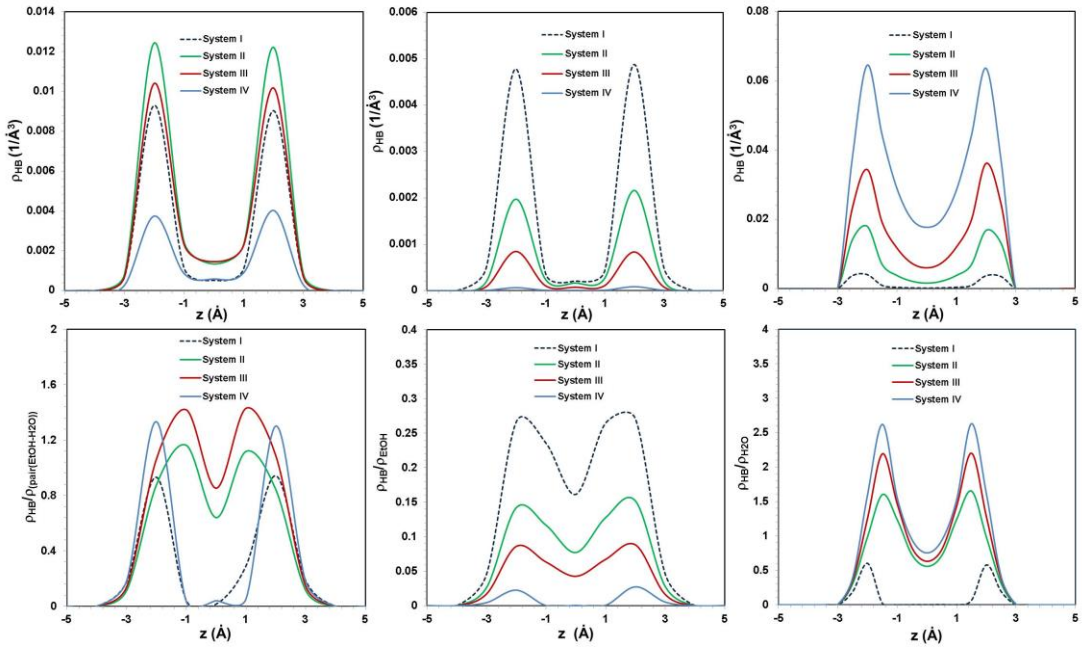

Figure 5.4. Top panels: Density profiles of hydrogen bonds (HBs) formed between water and ethanol molecules (left panel), between ethanol molecules (middle panel), and between water molecules (right panel) as a function of the distance z across the alumina pore along the z direction in the pore. Bottom panels: Same results shown on the top panels, but normalized with respect to the local molecular density (see text for details). Results are shown for simulated systems I, II, III, and IV. The reference (z = 0) corresponds to the center of the pore.

To visualize the molecular interactions between the various fluid molecules within the pore, we investigated the density of HBs as a function of water:ethanol molar ratio (systems I-IV). A geometric criterion was used to identify one HB between two molecules. More details about the method for HB identifications are

detailed in the previous work [145]. We considered HBs between water and ethanol molecules, those between two ethanol molecules, and those between two water molecules. The results are shown in Figure 5.4, left, middle and right panel, respectively. In the top panels we report the absolute values for the HB densities. In the bottom panels of Figure 5.4 we normalize the HB density values by the local molecular density. For both water and ethanol we consider the density of oxygen atoms. In the case of water-ethanol HBs (bottom left panel) the HBs density is normalized by the minimum of the local density of water or ethanol molecules. This choice was made to discount the presence of molecules that cannot participate to water-ethanol HBs.

The results for the absolute density of water-ethanol HBs (top left) suggest that these HBs are localized within the first hydration layer, whereas they are absent from the center of the pore. When the normalized data are considered (bottom left) the picture becomes more complete. For systems I and IV (ethanol-rich and water-rich, respectively) the water-ethanol HBs are indeed localized near the alumina surface, while for the other two systems some water-ethanol HBs form also near the pore center. While large variations in the peak density of water-ethanol HBs are observed in the top panel (with system II showing the largest density of water-ethanol HBs), the bottom panel reveals that the normalized density of this type of HBs does not change much with the system composition. This suggests that water and ethanol molecules tend to form as many HBs as possible in this highly confined system.

Regarding ethanol-ethanol HBs (middle panels of Figure 5.4), our results show that, as expected, both their absolute (top) and normalized (bottom) densities decrease as the water mole fraction increases, because there are fewer and fewer ethanol molecules available to form HBs. Our absolute results (top) suggest that

ethanol-ethanol HBs form predominantly near the alumina surfaces, and not near the center of the pore. This is a consequence of the tendency of ethanol molecules to form HBs with the –OH groups available on the alumina surface, as described elsewhere [37, 145]. Because of this preference, few ethanol hydroxyl groups are present near the pore center, as also suggested by the density profiles of the oxygen atoms of ethanol (shown in Figure B.2 in Appendix B).

Regarding the water-water HBs, as expected, our results show that their density increases as the water mole fraction increases. In the center of the pore the density of water-water HBs normalized by the water density (bottom right panel of Figure 5.4) does not change substantially for all systems considered other than system I (in which case the few water molecules present are adsorbed on the alumina surfaces). The density of water-water HBs is in general larger than that of both water-ethanol and ethanol-ethanol HBs because water molecules can form more HBs than ethanol molecules do (~3.5 HBs per water molecule in bulk liquid for the model implemented here vs ~1 HB per water molecule for bulk liquid ethanol [145]).

5.4.2.3 Dynamical Properties of the Confined Liquid Mixture

In Figure 5.5, we report representative results to quantify the dynamical properties for water and ethanol molecules confined within the alumina pore as a function of the fluid composition. The results were obtained after the systems had reached equilibrated states. We computed the residence autocorrelation function $C_R(t)$ (top panels) to estimate how long the various molecules remain within the pore, the dipole moment autocorrelation function (middle panels) to estimate the rotational dynamics of the molecules in the pore, and the mean square displacement (bottom panels) to estimate the translational mobility of the molecules within the pore. Once

the molecules exit the pore, they no longer contribute to the quantities calculated in this section. The results are shown separately for water and ethanol molecules.

Following prior reports [17, 156], the residence autocorrelation function is calculated as:

$$C_R(t) = \frac{\langle P(t)P(0)\rangle}{\langle P(0)P(0)\rangle} \tag{5.3}$$

where P(0) = 1 when the corresponding ethanol or water molecule is found inside the pore at time t = 0. If a tagged molecule continuously remains in the pore when the time t progresses, then P(t) = 1; P(t) = 0 when the molecule exits the pore. P(t) remains equal to 0 even if the molecule eventually returns inside the pore. It is possible to estimate how long water and ethanol molecules remain in the alumina pore by studying the residence autocorrelation function C_R. The faster the autocorrelation function decays to 0, the shorter the time water or ethanol molecules stay inside the pore. Considering the results in Figure 5.5, and comparing the results of $C_R(t)$ for water to those obtained for ethanol, it appears that water molecules remain inside the pore longer than ethanol molecules do at all pore fluid compositions considered. This is probably related to the stronger effective attraction between water and alumina surfaces and also to the higher free-energy barrier experienced by water as it desorbs from a freestanding alumina surface (see Figure B.1 in Appendix B). Within the first 500 ps, our analysis suggests that the C_R obtained for water molecules decays faster in the order system II > system I > system III > system IV. This order is inconsistent with the density of water (see Figure 5.3) and the density of both water-water and water-ethanol HBs (see Figure 5.4) observed within the pore. Perhaps a combination of steric effects (due to the bulky ethanol molecules) and preferential interactions (HBs with both ethanol and other water

molecules, but also with the surface) explains the residence time results. Conversely, the decay of the C_R obtained for ethanol molecules is directly related to both the density of ethanol molecules and the density of ethanol-ethanol HBs within the pore, suggesting that ethanol motion might be hindered by the presence of other ethanol molecules.

The dipole-dipole autocorrelation function is computed as:

$$C_{DM}(t) = \frac{\langle M_i(t) M_i(0) \rangle}{\langle N(t) M_i(0) M_i(0) \rangle} \tag{5.4}$$

where M(0) is the dipole moment of a water or that of an ethanol molecule at time t = 0, M(t) is the dipole moment of the same molecule at time t, and N(t) is the number of water or ethanol molecules remaining in the pore at time t. If molecules exit the pore, they do not contribute any more to the calculation even though they may return at some later time. Hence, as time progresses, N(t) decreases. The faster the reorientation correlation function decays from 1 to 0, the more quickly water or ethanol molecules change their orientation. Comparing the results of $C_{DM}(t)$ for water to those obtained for ethanol within the pore, we observe that ethanol molecules change their orientation more slowly than water molecules do at all pore fluid compositions considered. This is likely due to the fact that ethanol experiences more difficulty rotating when confined in the narrow pore compared to water (ethanol is large compared to water). The results of $C_{DM}(t)$ as a function of the pore composition show that the presence of more ethanol molecules inside the pore slows the rotational dynamics of both water and ethanol. It is likely that the greater the number of ethanol molecules that stay in the pore, the less accessible the space for water and ethanol to change their orientation.

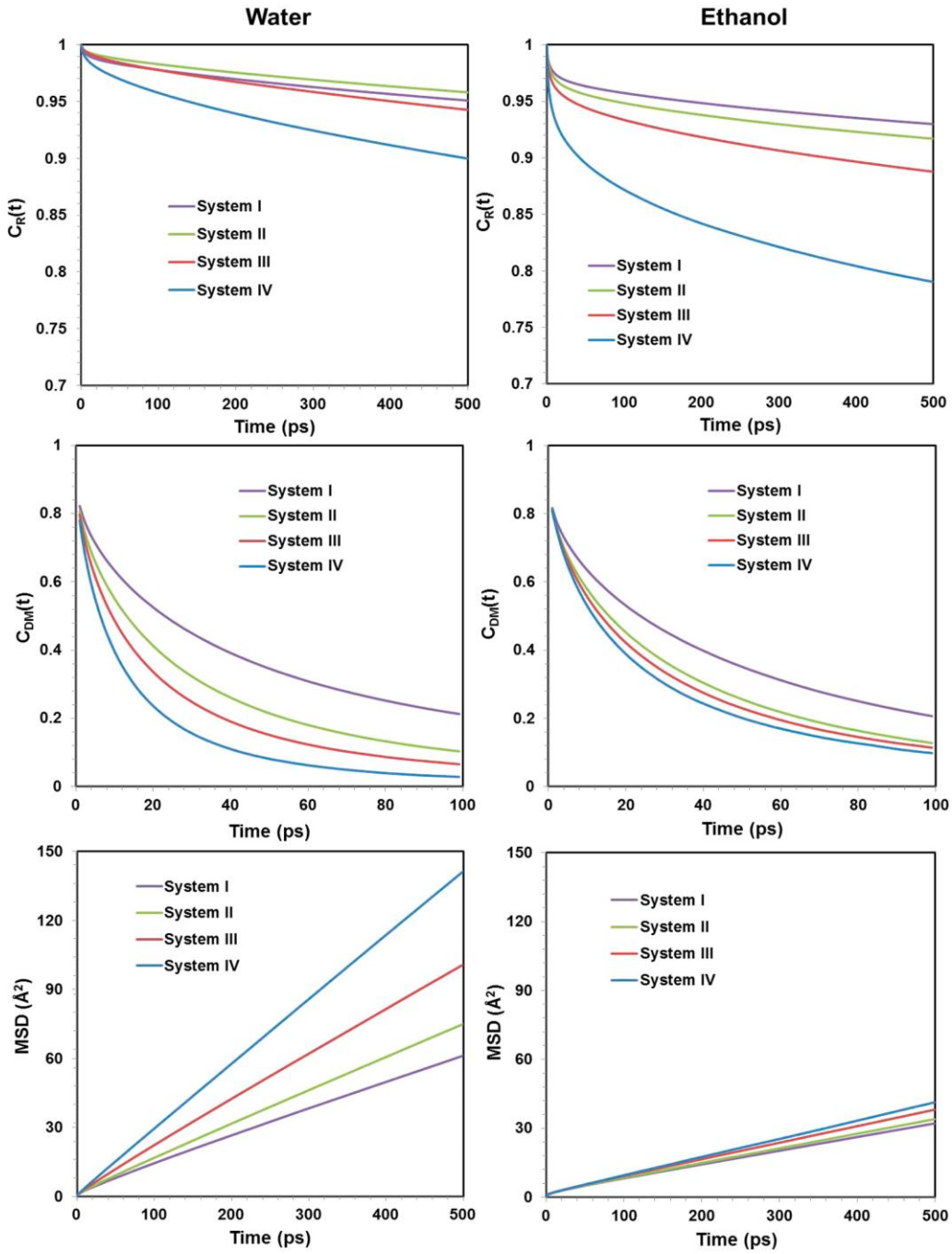

Figure 5.5. Dynamic properties for water (left panels) and ethanol (right panels) confined in the alumina pore at 298K for systems I, II, III, and IV. Top: Residence autocorrelation function $C_R(t)$. Middle: Dipole moment autocorrelation function $C_{DM}(t)$. Bottom: In plane mean square displacement parallel to the alumina pore surfaces. Only molecules inside the pore are considered for these calculations.

The in-plane mean-square displacement (MSD) is quantified as:

$$\left\langle \Delta r(t)^2 \right\rangle = \frac{\left\langle \sum_{i \in pore} \left[(x_i(t) - x_i(0))^2 + (y_i(t) - y_i(0))^2 \right] \right\rangle}{N(t)} \tag{5.5}$$

The slope of the in-plane MSD as a function of time could be used to estimate the self-diffusion coefficient for water or ethanol molecules in the plane parallel to the pore surfaces [64]. The larger the slope, the faster molecules diffuse. The results (bottom panel of Figure 5.5) suggest that the diffusivity of water molecules increases with water density whereas that of ethanol increases as the ethanol density in the pore decreases. Yang et al. [140] reported results qualitatively similar to those in Figure 5.5 in their study on ethanol/water transport through silicalite membranes. Our results show that the mobility of water is enhanced with decreasing ethanol concentration, which illustrates an anti-plasticization effect of ethanol on water within the alumina pore considered here, presumably due to both steric effects (ethanol is large compared to water) and to the slow mobility of confined ethanol [157].

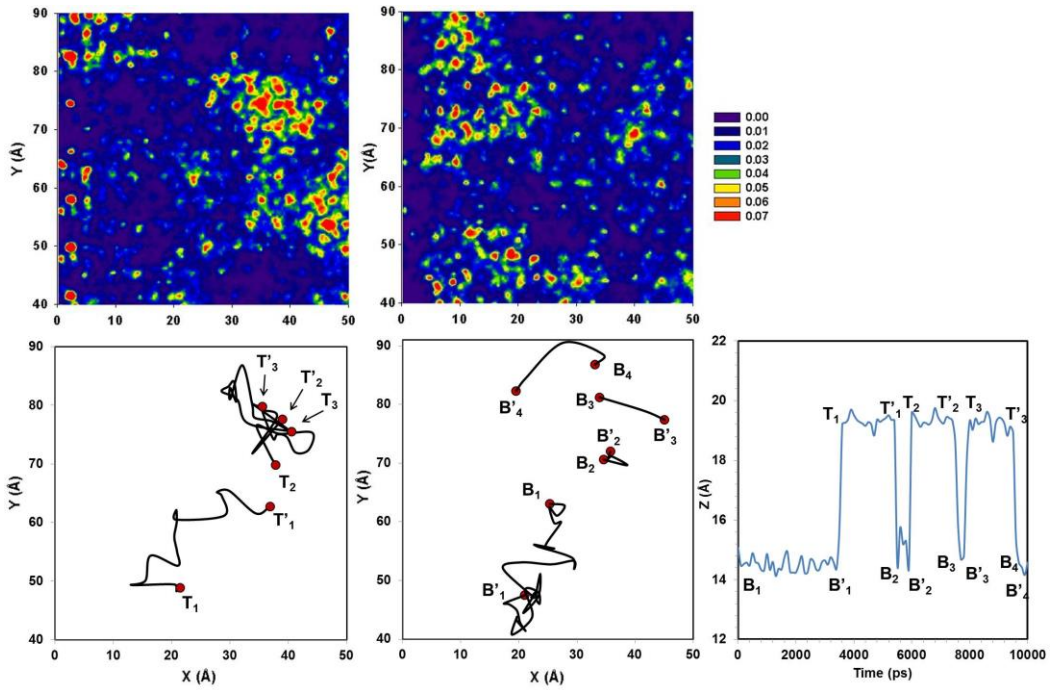

Figure 5.6. Trajectory of one representative water molecule in the X – Y plane (bottom left and middle panels) together with the planar density distribution of water at the top (top left) and bottom (top middle) slabs. The trajectory of the representative water molecule in the Z dimension as function of simulation time is also shown (bottom right). The trajectories are obtained from 10 ns long simulation fragments for system I, respectively. B-B' or T-T' represents the planar distances that this water molecule travels while remaining continuously on the bottom or on the top surfaces, respectively. Densities are expressed in $1/\dot{A}^3$.

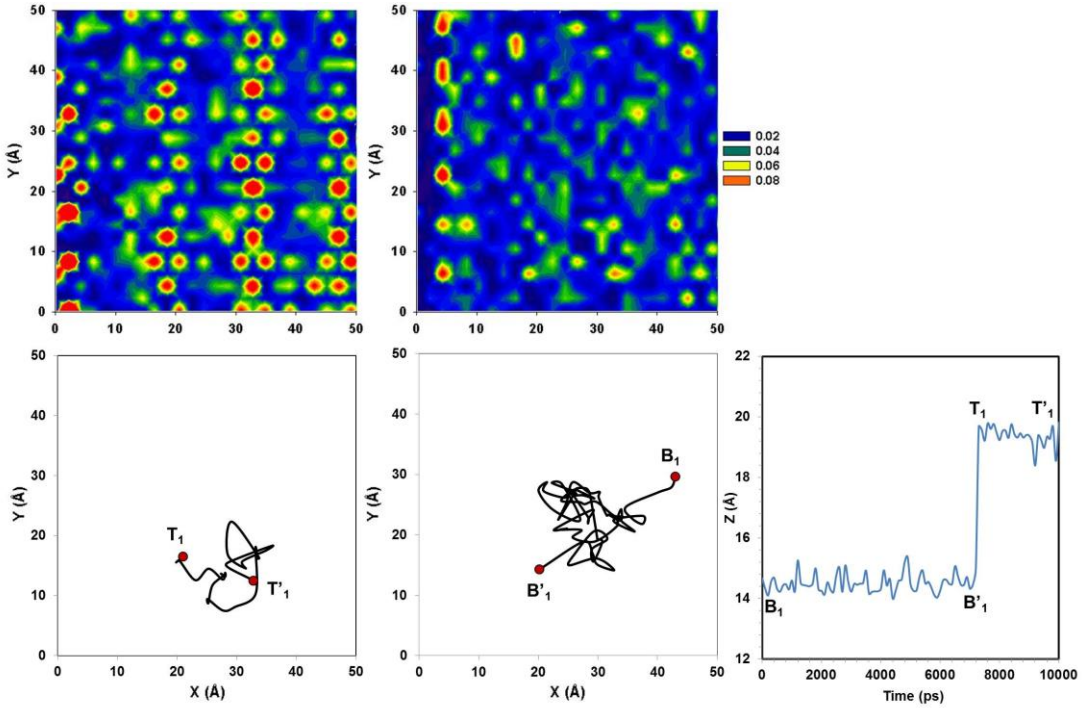

Figure 5.7. Same as Figure 6, for one representative ethanol molecule.

In Figure 5.6 and 5.7 we report the trajectories of representative molecules obtained from 10 ns long simulation fragments. For this analysis we consider only system I. Figure 5.6 and 5.7 refer to water and ethanol, respectively. The left and middle bottom panels are projections on the X-Y plane (top and bottom pore surfaces, respectively), and the right bottom panels are projections in the Z direction. We also show the planar density profiles for oxygen atoms of water and of ethanol in the left and middle top panels of Figures 5.6 and 5.7, respectively. Visual inspection of a number of simulated trajectories confirm that the results shown in Figures 5.6 and 5.7 are representative of the behaviour of confined water and ethanol, although a thorough statistical analysis was not performed. Visual inspection of the trajectories suggests that water molecules travel larger planar distances than ethanol molecules in an equal length of time, which is consistent with the MSD results. Perhaps more

interestingly, our results show that water molecules remain for rather long times close to the high-density locations of water in the hydration layer and travel larger distances when they enter regions covered mostly by ethanol. Occasionally, they leave one hydration layer and they 'jump' to the hydration layer on the opposite pore surface (top to bottom or vice versa). In some cases they move along the X-Y direction while they are in between the two hydration layers. This is due to the low molecular density found at the center of the pore (see Figure 5.3), which facilitates molecular diffusion. However, in general, the water molecules do not move in the planar direction while jumping from one hydration layer to the other, at least within the results shown in Figure 5.6. In the short length of our analysis, the single water molecule transferred from one hydration layer to the opposite one several times, which is probably related to the reduced free-energy barrier experienced upon sorption/desorption when multiple water molecules are present on the alumina surface (see Appendix B).

During the same length of time (10 ns), the ethanol molecule considered in our analysis (Figure 5.7) did not travel very far along the X-Y plane, and only once managed to move from the solvation layer on one surface to the one on the opposite surface. This is consistent with the slow dynamical, rotational and translational motions, quantified for ethanol molecules in Figure 5.5.

It is possible that the different mobilities observed for water and ethanol molecules are due to the different crowding environments, with molecules found in low-density regions moving faster than those found in high-density neighbourhoods. To test this hypothesis, we select two water molecules and two ethanol molecules, one that moves rather fast and one that diffuses rather slowly. For each molecule we calculate in-plane RDFs with the surrounding fluid molecules. We then compare the

results for the fast and the slow molecules (Figure B.3 in Appendix B). For both water and ethanol, our results suggest that slow and fast molecules do not pack differently with respect to neighbouring ethanol molecules. However, there is a significant difference in the packing of water molecules near the fast- or slow-moving water and ethanol molecules. In particular, water molecules diffuse fast when surrounded by fewer water molecules, while ethanol molecules diffuse fast when surrounded by many water molecules. Because ethanol molecules lie preferentially with the CH_2-CH_3 bond almost parallel to the surface and their OH group forming hydrogen bonds with the surface groups, our results suggest that ethanol molecules can be dislocated from the surfaces when HBs can be formed with surrounding water molecules. Indeed, the results shown in Figure B.4 in Appendix B confirm that when ethanol molecules orient their OH groups nearly parallel to the surfaces, presumably to form HBs with surrounding molecules, they move faster than when they point their OH groups perpendicularly to the surfaces.

5.4.3 Bulk Liquid Mixtures – Dynamical Properties

To better appreciate the effect of confinement on the properties of water-ethanol mixtures, we calculated some dynamical properties for water and ethanol in the bulk phase. Mimicking the calculations for the confined systems, we calculated the residence autocorrelation function, the dipole moment autocorrelation function, and the 3-D MSD for water and ethanol molecules outside of the pore as a function of the fluid composition. The results are shown in Figure B.5 in Appendix B. We considered systems I, II, III, and IV, and the calculations were performed after the systems reached equilibrium. Note that the equilibrium bulk compositions for systems III and IV (12/88 and 24/76 (mol/mol) water/ethanol, respectively) are below the azeotrope, while those for systems I and II (6/94 and 9/91 (mol/mol)

water/ethanol, respectively) are above the azeotrope. The algorithms implemented here are analogous to those discussed for Figure 5.5, except that the MSD is calculated in the three directions. Only those molecules that remain continuously in the bulk were considered.

The results for C_R and C_{DM} show a strong dependency on composition. In particular, both water and ethanol molecules move more slowly at compositions near the azeotrope. This is probably because of the formation of an extensive HB network between water and ethanol molecules at such conditions. The results for the MSD show that the translational mobility of water is somewhat comparable to that of ethanol at each composition considered. This trend is qualitatively similar to experimental observations, according to which the self-diffusion coefficient of ethanol is similar to that of water when the water mole fraction ranges from 0.05 to 0.25 [158-160]. The MSD data suggest that the self-diffusion coefficient of both ethanol and water decreases monotonically with the water mole fraction. Within the range of compositions considered here, the self-diffusion coefficient of bulk water increases as the ethanol density increases. These results suggest a plasticization effect of ethanol on water, whereas our prior results showed an anti-plasticization effect within the pore.

5.5 Conclusions

Molecular dynamic simulations were employed to investigate the adsorption, structure, and dynamics of liquid water-ethanol mixtures in 1 nm wide slit-shaped alumina pores at ambient conditions. The results are consistent with the selective adsorption of water within the pores. This seems to be due to preferential surface-water interactions, consistent with results on freestanding alumina surfaces. Analysis of the molecular structure for the mixtures under confinement shows that the

preferential adsorption is predominantly a surface-driven phenomenon, suggesting that it should be less pronounced in pores much wider than those considered for the present simulations. The investigation of the dynamical properties of the confined mixtures suggests that water diffuses through the narrow pores faster than ethanol. Because both the structure and dynamics of confined fluids depend on size and shape of the confining pores, the results presented here are strongly dependent on pore features. Preliminary results on slit pores of width 0.6 nm show, for example, more pronounced enrichment of water compared to the data discussed in this paper. The combination of structural and dynamical results reported here for water-ethanol mixtures suggests that alumina-based porous materials could be used as permselective membranes for the removal of water from aqueous ethanol solutions. The performance of such devices for practical applications will also depend on the rate at which molecules enter and exit the pores [161, 162], which has not been quantified in the present analysis.

Chapter 6 Aqueous Methane in Slit-Shaped Silica Nanopores: High Solubility and Traces of Hydrates

The material presented in this section was published in 2014 in volume 118, pages 4860-4868 of The Journal of Physical Chemistry C.

6.1 Abstract

Equilibrium molecular dynamic simulations were employed to investigate the methane solubility in water confined between two parallel silica surfaces. The solid substrate was obtained from β-cristobalite; all nonbridging oxygen atoms were protonated. The resultant surface density of OH groups was of ~4.54 sites per nm^2. The simulations were conducted at constant temperature, 300K, and at increasing bulk methane pressure for pores of width 1.0 nm. For bulk systems, these thermodynamic conditions are outside of the window of methane hydrates stability. Methane solubility in confined water was found to far exceed that in bulk systems. The increase in tangential pressure, observed under confinement, cannot solely explain the marked increase in solubility predicted by our simulations. Most likely, the structure of confined water favours the sequestration of methane. The excess chemical potential for methane was found to significantly decrease within the confined water compared with that in the bulk phase. On the basis of the cage adsorption hypothesis for hydrate nucleation, the predicted solubility of methane in the confined water (up to ~0.05 mole fraction) is large enough to suggest the possible formation of methane hydrates. Indeed, analysis of simulation data shows the presence of amorphous cages of hydrogen-bonded water that host a single methane molecule. Within the limits of our simulations, these amorphous cages only last for short times. Perhaps the pores considered are too narrow to allow the formation of

stable methane hydrates, and perhaps longer simulations would allow us to observe the formation of a hydrate nucleus. The large methane solubility in confined water predicted by our simulations might have consequences for hydraulic fracturing and other technological processes.

6.2 Introduction

Understanding the behaviour of mixtures of water and volatile hydrocarbons confined in subsurface formations is important for explaining the geochemical processes at Earth's subsurface, the crust and mantle [55, 56]. Recent reports have shown that the methane content in aquifers within regions where hydraulic fracturing is performed is exceptionally high [163]. Although these reports are to some extent controversial, understanding the possible physical reasons responsible for such observations might help prevent undesired environmental consequences due to hydraulic fracturing. From a different perspective, under appropriate pressure-temperature conditions the simultaneous presence of water and natural gas leads to the formation of natural gas hydrates. Methane hydrates have seized great scientific attention because of the potential of harvesting methane as an energy source and because of their possible impact on global warming should the stored methane, a powerful greenhouse gas, be unintentionally released to the atmosphere. Much remains to be understood regarding the formation and stability of methane hydrates, especially under confinement [164-166]. Many experimental [167-172] and computational studies [173-181] have dealt with bulk gas hydrate systems. A few experimental investigations focused on the impact of solid surfaces or porous matrices on the formation of gas hydrates [59-62].

Several algorithms, typically based on MD simulations, have been implemented for triggering the spontaneous formation of hydrates. Some promote high methane

concentration by melting a hydrate crystal [175, 182, 183], others conduct MD simulations for up to microseconds, employ coarse-grained models to speed up calculations [179, 184], or constrain the thermodynamic gradients during the simulations [185, 186]. Guo and Roger [187] studied the pre-nucleation steps of methane hydrate formation under metastable conditions. Their observations are invoked below to explain some of our results. Other molecular simulation studies provided insights regarding the structure and behaviour of gas hydrates near a solid surface or within porous matrices [188-191]. In some cases, silica surfaces were considered [192-194]. It is expected that the presence of the surfaces can facilitate the formation of gas hydrates, possibly because the surfaces provide nucleation sites. However, it is also possible that the surfaces prevent the formation of hydrate cages via a distortion of the hydrogen-bonded network formed by interfacial water molecules. No simulation studies have been carried out for the formation of gas hydrates confined in pores, silica or otherwise, with pore size smaller than the size of the sI or sII hydrate unit cell (12 Å).

We report equilibrium MD simulations conducted for methane – water mixtures confined within 1 nm slit-shaped silica pores in equilibrium with bulk methane at moderate conditions (T = 300K, P_{bulk} = ~6 – 28 MPa). Silica pores were used in this study because it has been reported that gas hydrates can be found in sand layers [195]. We examined the methane solubility in water inside the pore as well as the structural properties of water molecules surrounding methane under confinement. In addition to studying methane solubility in confined water and the molecular structure of the confined systems, we attempt to answer the following fundamental questions: can hydrates form in such small silica pores at mild bulk pressures? What is the main driving force for triggering the hydrate formation in the confined phase?

6.3 Methods and Algorithms

Our MD simulations were performed using the package GROMACS [68, 131]. Two silica slabs facing each other across the pore volume along the Z direction yield slit-shaped pores. The silica slabs were constructed to reproduce β-cristobalite SiO_2. All the nonbridging oxygen atoms on the silica surface were protonated, yielding 4.54 OH groups per square nanometer, which is realistic [18, 31]. In our simulation box each of the two surfaces across the volume is of dimensions 104.05×100.8 $Å^2$ (X – Y plane). The simulation box is periodic in the X, Y, and Z directions. The Y dimension of the simulation boxes reflects the periodicity of the solid crystalline substrate (100.8 Å); the X and Z dimensions were set to 224.78 Å and 42.92 Å, respectively. All simulations were carried out for pores of width 10 Å (the pore width refers to the shortest center-to-center distance between surface oxygen atoms of top and bottom slabs). Because of periodic boundary conditions, the silica pores are effectively infinite along the Y direction. On the contrary, the pores are finite along the X direction, along which they are exposed to 'bulk' systems. The simulation setup mimics the one implemented in prior studies [196].

The initial configuration is built with water and methane molecules placed outside the slit pore, in the 'bulk' region. As the simulation progresses, water and methane fill both the pore and the bulk volume. The number of water molecules was fixed at 3,300 while the methane molecules were varied from 1,000 to 4,000. The 3,300 water molecules were sufficient to fill approximately half of the pore volume along the X direction. By changing the number of methane molecules we manipulated the bulk pressure, which we estimated for each system after equilibrium was achieved using the Peng Robinson equation of state from the density of molecules in the bulk gas phase (pure methane) [197]. The calculated bulk pressures

for various CH_4-H_2O system compositions are shown in Table 6.1. Note that in hydraulic fracturing high pressure is obtained by pumping large amounts of water, while we obtain high pressures by adding methane to the simulated system. As we are interested in the behaviour of water-methane systems within the pores, the two processes are equivalent for the scopes of the present work.

Table 6.1. Bulk phase pressure estimated for seven methane- water systems simulated at T=300K.

Number	**System Composition**	**Estimated Bulk Pressure (MPa)**
1	1000 CH_4-3300 H_2O	6.29
2	1500 CH_4-3300 H_2O	9.30
3	2000 CH_4-3300 H_2O	12.17
4	2500 CH_4-3300 H_2O	15.22
5	3000 CH_4-3300 H_2O	18.94
6	3500 CH_4-3300 H_2O	22.79
7	4000 CH_4-3300 H_2O	27.61

The CLAYFF force field was implemented to describe the silica slabs [65]. The silicon and oxygen atoms were held at fixed positions while the surface hydroxyl hydrogen atoms were allowed to vibrate. The OPLS-UA was implemented to model methane [66], and the rigid SPC/E model was used to simulate water [67]. The SPC/E water bonds and angles were kept fixed by employing the SETTLE algorithm [70]. Nonbonded interactions were modelled by means of dispersive and electrostatic forces. The electrostatic interactions were modelled by the Coulombic potential. Dispersive interactions were modelled with 12-6 Lennard-Jones potentials. The Lennard-Jones parameters for unlike interactions were determined by the Lorentz-Berthelot combining rules [64] from the values of like components. The cutoff

distance for all interactions was set to 9 Å. Long range corrections to electrostatic interactions were treated using the PME method [94].

Temperature, pressure, and methane – water potential models are known to strongly impact methane solubility in water. In this work, we focus only on the effect of pressure on the solubility of methane in water at 300 K and moderate bulk pressures (the thermodynamic conditions considered are outside of the hydrate stability conditions [198]). Paschek [199] observed that choosing a water model that describes correctly the density of pure water plays an important role in illustrating the behaviour of methane in water. Because the SPC/E water model correctly describes the water density at ambient conditions, we consider it a reasonable choice for the present study, as the simulations are only conducted at 300 K and moderate pressures. Docherty et al. [200] obtained the excess chemical potential of methane in water by adjusting the dispersive methane-water interactions to properly account for polarization effects. In our simulations we did not modify the dispersive methane-water interactions to account for polarizability which might impact on describing correctly the excess chemical potential for non-ideal mixtures (e.g. methane –water mixtures). Despite this approximation, although our absolute values for the excess chemical potential of methane do not reproduce quantitatively experimental data [201, 202], they agree with literature simulation data [203, 204], and the excess chemical potential obtained from our simulations (9.31 kJ/mol) compares well with experimental data (8.48 kJ/mol). We consider our calculations valuable for comparing the excess chemical potential of confined versus bulk systems (the same approximations are implemented in both environments), not for estimating the absolute value of the excess chemical potential.

All simulations were performed in the canonical ensemble (NVT) where the number of particles (N), the simulation volume (V), and the temperature (T) were kept constant. The simulated temperature was maintained at 300 K and controlled by a Nosé-Hoover thermostat [95, 96] with a relaxation time of 100 fs. The equations of motion were solved by implementing the leapfrog algorithm [97] with 1.0 fs time steps. The total simulation time was 49 ns. Data analysis was conducted over the last 2 ns of the simulations, after 47 ns of equilibration were completed. Equilibration was considered achieved when the density of methane within the pore approached a constant value that did not change appreciably over 13 ns.

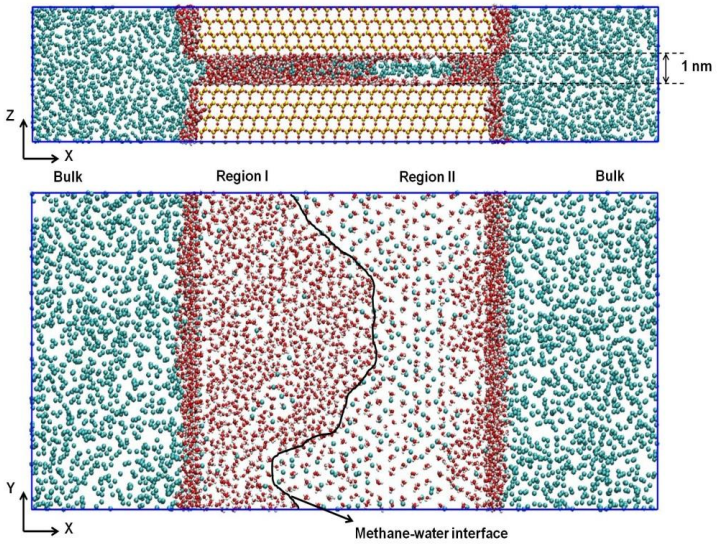

Figure 6.1. Side and top views of a representative simulation snapshot for a system containing 3,000 CH_4 and 3,300 H_2O molecules (P_{bulk} = 18.94 MPa). Yellow, red, white, and cyan spheres represent silicon, oxygen, hydrogen atoms, and methane molecules, respectively.

6.4 Results and Discussion

The final configuration obtained for the system containing 3000 CH_4 and 3300 H_2O molecules (P_{bulk} = 18.94 MPa) at 300K after 49 ns is shown in Figure 6.1 (side and top views are both provided). The top view of the system (bottom panel) is

shown without the two silica slabs for clarity. For all simulated systems, water occupies approximately half of the pore volume and methane occupies the remainder of the pore volume and most of the bulk. An interface can be observed between methane and water within the pore, which divides the pore in two regions: region I contains mostly water (with methane dissolved, left side in Figure 6.1) and region II contains mostly methane (with some water near the silica surfaces, right side in Figure 6.1). In region I some methane molecules are dispersed within the confined water, while in region II water wets the surfaces and methane occupies the pore center. The region I – region II interface that can be seen roughly parallel to the Y direction of the simulation box (black curve in Figure 6.1) is irregular in shape. This unexpected shape is probably due to fluctuations in the local pressures at the methane – water interface [205]. In fact, during our simulations we observed a frequent exchange of methane molecules between region I and region II, which likely causes fluctuations in the local pressure. Such fluctuations are probably accentuated by the small size of the pore simulated. Koga et al. [206], using in situ neutron reflectivity, found that the water-methane interface can become very rough at conditions when hydrates start forming. Although this experimental observation might not apply to our simulations because the experiments were conducted for bulk systems, the authors suggested that microscopic hydrate embryos form at the methane – water interface in a dynamic equilibrium manner, causing the rough interface.

6.4.1 Methane Density Profiles

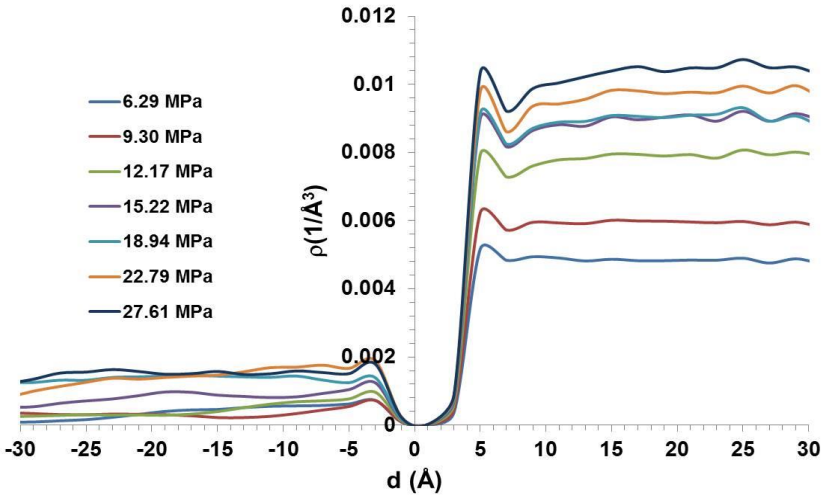

Figure 6.2. Density of confined methane molecules in the direction perpendicular to the methane-water interface. In this representation the interface is located at d=0.0 nm. Regions I and II (water-rich and methane-rich) are found at negative and positive d, respectively.

To gain quantitative insights regarding the behaviour of methane, we calculated its molecular density in the direction parallel to the pore surface (e.g., from left to right in Figure 6.1). Along this direction methane is found both in region I (water rich) and in region II (methane rich). To identify the position of the interface between region I and region II, we implemented the algorithm proposed by Berkowitz et al. [207]. Briefly, for each methane molecule, the algorithm searches for the nearest water molecule at the interface. The X component of the distance between the methane molecule and the nearest water molecule at the interface is then used as the position of the methane molecule, ***d***. More details are provided as Appendix C. The methane density profiles are then reported as a function of the distance from the interface between region I and region II.

In Figure 6.2 we show the methane density profiles for seven systems. The reference (d=0) corresponds to the position of the interface. Regions I and II

correspond to negative and positive ***d***, respectively (see Figure 6.1). The results show that in all cases the methane density is zero at the interface and that the methane density increases far from the interface. Methane densities in region II are much higher than those in region I because of the large amount of water present in region I. Two maxima in methane concentration are observed at ***d*** ~-3 Å and ~5 Å (regions I and II, respectively). After some oscillations, the methane densities reach approximately constant values 'far' from the interface. Note that the average methane density in region I remains constant after equilibration even though the interface between region I and region II (black curve in Figure 6.1) changes shape continually. In general, in both regions I and II the methane density 'far' from the interface increases as the bulk pressure increases. However, the trend is not monotonic. For example, our results suggest, perhaps unexpectedly, that when the bulk pressure decreases from 18.94 to 15.22 MPa the methane density in region II does not change, while the methane density decreases in region I. This is surprising because the methane density in region II increases sharply when the bulk pressure increases from 6.29 to 12.17 MPa, while in the same pressure range the methane density does not change in region I. Methane density in region I also does not seem to change much when the pressure increases from 18.94 to 27.61 MPa. These observations suggest that changes in methane solubility in confined water are not proportional to the bulk pressure, perhaps because a transition occurs for the methane-water system under confinement at some of the conditions tested.

6.4.2 Structure of Confined Aqueous Methane

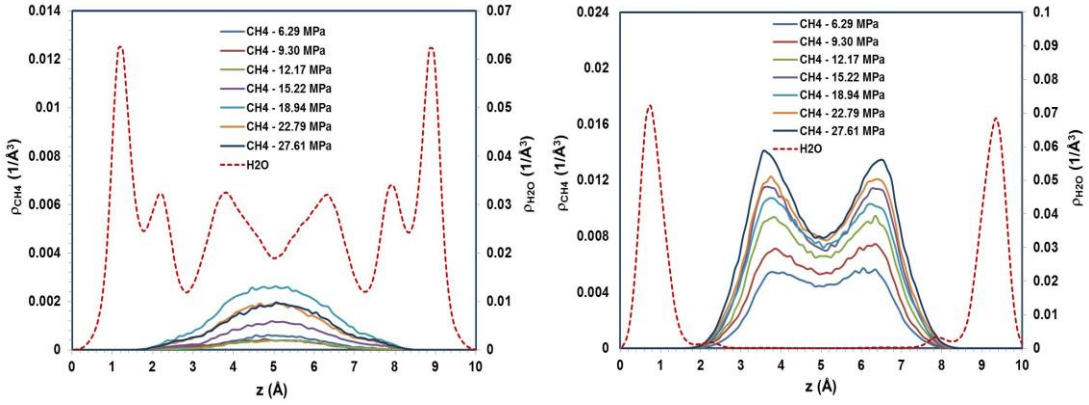

Figure 6.3. Density profiles of water oxygen atoms (dotted curve) and methane molecules (continuous curves) as a function of the distance z across the silica pore. The results are obtained from seven simulation systems. The data are shown for Region I (left panel) and Region II (right panel). The reference (z = 0) is the plane formed by the oxygen atoms of the surface hydroxyl groups of the bottom silica slab. Note that the density profiles for water do not change significantly with pressure.

To quantify the preferential distribution of methane within the pore, we calculated density profiles for water oxygen atoms and methane molecules along the Z direction perpendicular to the pore surface. This analysis is common for understanding fluids confined in narrow pores [208, 209]. Our calculations are conducted independently for region I and for region II because of the different molecular distribution evident from visual inspection of, e.g., Figure 6.1. In the left and right panels of Figure 6.3 we report the results obtained in regions I and II, respectively, as the pressure increases. The reference (z = 0) is the plane of oxygen atoms formed by the surface hydroxyl groups of the bottom silica surface. The water oxygen atomic density profiles indicate the formation of two well-defined hydration layers in contact with the pore surfaces (peaks at 1.15 Å and 8.95 Å in region I and peaks at 0.75 Å and 9.35 Å in region II). In region II, a small, almost imperceptible density peak for water molecules is found at z ~2.25 Å (and, symmetrically, at z ~7.85 Å). The results for the density profiles for water oxygen atoms as a function of

the distance Z inside the pore (both region I and II) do not change as the bulk pressure increases (data not shown for brevity), although the distribution of water in the two regions is obviously very different (as confirmed by visual inspection of simulation snapshots). On the contrary, the density profiles for methane in both regions I and II change as the bulk pressure increases. These data are shown in both left and right panel of Figure 6.3. In region II, methane molecules are always excluded from the two hydration layers near the solid surfaces and form two layers near the center of the pore. In region I, methane molecules seem to accumulate in a rather wide region near the center of the pore. Although this region of methane accumulation is centered in a layer of low local water density, we point out that other layers of lower local water density exist within the pore but do not seem to promote methane accumulation (e.g., right after the first two hydration layers). In the case of aqueous electrolytes confined in narrow pores, our prior simulations suggested stronger correlations between hydration layers and preferential ions distributions [1, 10]. Note that the molecular density of methane in region I is approximately 1 order of magnitude lower than that of water. Generally, the increase of bulk pressure increases the molecular density of methane in both regions I and II (inside the pore). However, it can be seen that the methane density in region I remains constant as the bulk pressure increases from 6.29 to 12.17 MPa. This observation is consistent with the results discussed in Figure 6.2. Unexpectedly, while the increase of bulk pressure from 18.94 to 27.61 MPa builds up the methane density in region II, the density of methane in region I decreases. Other small changes in the density profiles for confined methane as a function of bulk pressure might be related to computational uncertainties.

In addition to density profiles in the direction perpendicular to the surface, we calculated in-plane density profiles for water oxygen atoms within the first hydration layer. Following prior studies [18, 20, 31], we also computed the in-plane density distribution of HBs formed between water molecules. To identify one HB we used the geometric criterion proposed by Marti [106]. The results are shown in Figure 6.4. Regarding the distribution of water molecules (top panel), we found a large difference when the structural arrangement in region I was compared to that of region II. Whereas in region I water molecules accumulate above the vertices of the hexagons formed by silicon atoms on the surface, as described by Ho et al. [20], water molecules in region II preferentially occupy in the middle of the silicon hexagonal rings (see schematic in Figure 6.5). It should be noted that water molecules in region I fill the whole pore while in region II water molecules only wet the silica surfaces, in qualitative agreement with simulation results for similar systems reported by Bagherzadeh et al. [194] The results shown in Figures 6.4 and 6.5 are probably due to the fact that water molecules at interfaces tend to adopt the molecular structure that maximizes the number of HBs (both among water molecules and between water and surface groups). In region I, water molecules in the first hydration layer can form HBs among themselves (as shown in the right panel of Figure 6.4) and with water molecules farther from the surface (as discussed elsewhere [10, 20]). On the contrary, in region II, the water molecules in the first hydration layer can form HBs only with the surface –OH groups, as no HBs are possible with methane (note that no water-water HBs are found in region II – right panel of Figure 6.4).

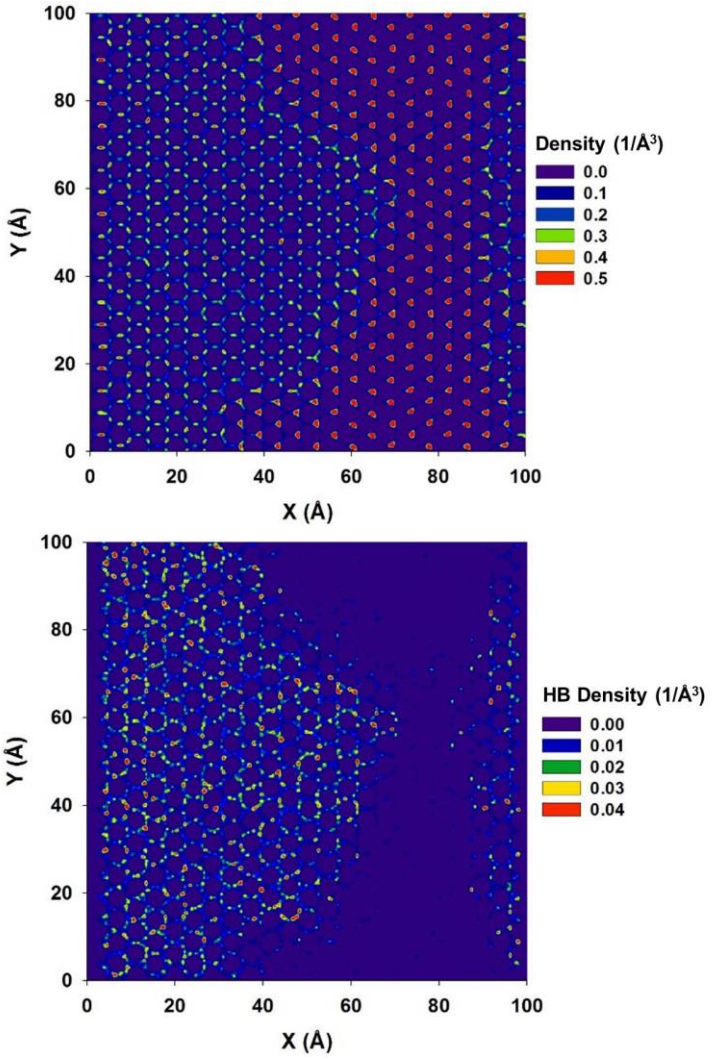

Figure 6.4. Surface density distributions of water oxygen atoms found in the first hydration layer (top panel) and water-water hydrogen bonds found within the to the first oxygen peak (bottom panel). The entire pore surface is considered, with Regions I and II on the left and right of each panel (see Figure 6.1). The results are obtained for the system containing 3,000 methane and 3,300 water molecules (P_{bulk} = 18.94 MPa). Densities are expressed in $1/Å^3$.

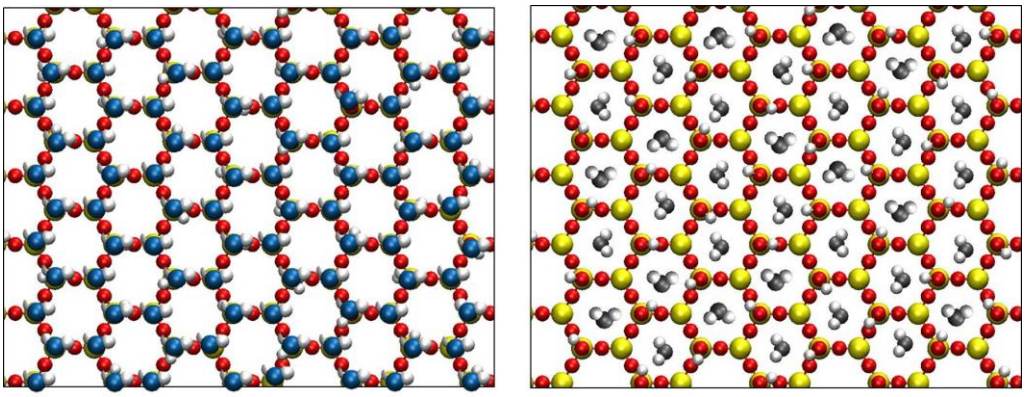

Figure 6.5. Schematic of the preferential adsorption sites for water molecules in the first hydration layer on Regions I (left panel) and II (right panel). Blue spheres represent the positions of water oxygen atoms in Region I above the vertices of the hexagons formed by six silicon atoms on the surface. As described elsewhere [20], water molecules occupy alternatively the vertices of the hexagons highlighted in the left panel. The gray spheres represent the positions of water oxygen atoms in Region II, where water preferentially adsorbs on the middle the hexagonal rings formed by the surface atoms. For a more detailed description of the structure of interfacial water near silica see Ho et al. [20].

6.4.3 Methane Solubility

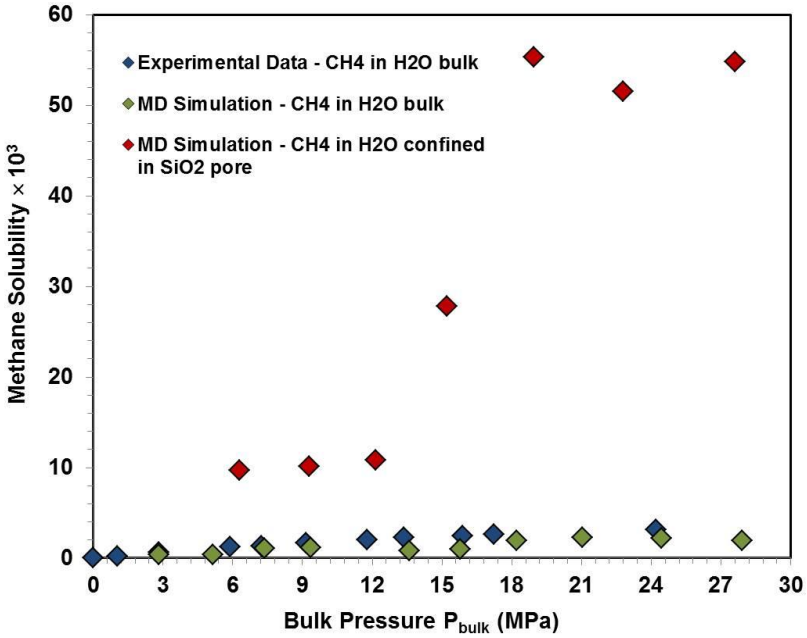

Figure 6.6. Methane solubility in liquid water as a function of bulk pressure. Simulation data for confined systems from this work are shown as red diamonds. Simulated bulk CH_4 solubility data in liquid water at 298K as reported by Sakamaki et al. [210]are shown as green diamonds. The correspondent experimental data [211-213] for CH_4 in bulk water are shown as blue diamonds.

On the basis of equilibrated systems we can calculate the methane solubility in the confined water. For these calculations we consider only the water-methane mixture in region I. The results are shown in Figure 6.6, in which methane solubility is shown as a function of bulk pressure. As mentioned above, the bulk pressure is estimated from the methane density using an equation of state (see Table 6.1). More details are provided as Appendix C. The red symbols in Figure 6.6 are the results from the present work, obtained at 300K. For comparison, we also report the methane solubility in bulk liquid water at 298 K as predicted, using simulations, by Sakamaki et al. [210], as well as experimental data for bulk systems from the literature [211-213]. The results in Figure 6.6 are consistent with a significant increase of methane solubility in water under confinement compared to bulk data

(both from simulations and from experiments) at comparable T and P. Although this result is at first sight surprising, it should be noted that several studies have recently shown that confinement enhances gas solubility in liquids. For example, using GCMC simulations, Luzar and Bratko [214] found large increases for N_2 and CO_2 solubility in water upon confinement within hydrophobic pores; Miachon et al. [215] reported proton NMR experimental data for the solubility of hydrogen, methane, and ethane in CCL_4 or CS_2 confined in γ-alumina and silica mesopores, showing a dramatic increase of gas solubility induced by confinement. Diaz Campos et al. [216] reported enhanced methane solubility in water confined in slit-shaped graphitic pores. Bagherzadeh et al. [194] did not report significant methane solubility enhancement in the water that forms bridges between two hydroxylated silica surfaces. It is possible that these simulations, which lasted ~2 ns, were too short, as Guo and Rodger [187] reported that ~50 ns are needed to approach equilibrium. It is also possible that the structure of water within those molecular bridges was not inductive to enhance methane solubility.

We can gain insights into enhanced methane solubility in confined water by considering results from Long et al. [217], who recently pointed out that the tangential pressure in carbon nanopores can be much larger than the bulk pressure because of confinement effects. Should a similar phenomenon occur for the systems considered here, the pressure in the pores could be much larger than that of the bulk systems the pores are in equilibrium with. To test this possibility we calculated the pressure tensor within the silica pores, implementing the algorithm explained in detail in the Appendix C. The results of tangential pressures are presented in Figure C.3 in Appendix C. We found that even though the tangential pressure is larger than

the bulk pressure, the enhanced pressure alone cannot explain the enhanced methane solubility predicted by our simulations.

To further understand the increased solubility of methane in confined liquid water, we evaluated the excess free energy for methane in bulk liquid water and in confined liquid water (see Table C.1 in Appendix C). More details about the method for excess free energy calculations are illustrated in Appendix C. The calculated excess chemical potential for CH_4 in bulk liquid water at 300K (9.31 kJ/mol) is consistent with that reported by Lee et al. [204] (9.57 ± 0.16 kJ/mol). When water is confined within the silica pore, our results show a lower excess free energy per CH_4 molecule (8.77 kJ/mol), which is consistent with higher methane solubility in confined versus bulk water.

In Table 6.2 we summarize our results as a function of the tangential pressure within the pores as well as the bulk pressure. Although methane solubility is found to generally increase as the tangential pressures increases, the increase is small when the tangential pressure increases from 18.65 to 31.26 MPa but dramatic when the pressure increases from 31.26 to 36.99 MPa. Further increase of the tangential pressure has little effect on the methane solubility, which fluctuates around 53.9 ± 1.5×10^{-3} in the pressure range from 36.99 to 44.59 MPa.

It is worth noting that the bulk conditions considered for the present simulations (T = 300 K, P ~6-28 MPa) are out of the methane hydrate stability range for bulk systems. Despite this, we observe that when the bulk pressure is ~18.94 MPa, the solubility of methane in confined liquid water reaches ~0.05, approximately one-third that of the methane solubility in methane hydrates. Guo et al. [187] reported that this methane concentration (corresponding to approximately 1.7 methane molecules per cubic nanometer) is necessary to initiate the nucleation of methane

hydrates. At this concentration the average separation between methane molecules in bulk systems is of 8.4 Å. Guo et al. [218] proposed the cage adsorption hypothesis (CAH) to describe the mechanism of hydrate formation. According to the CAH, one methane molecule must cross an energy barrier located at ~8.8 Å from a growing hydrate cage to adsorb to the outside of a cage face, resulting in the growth of the hydrate. Hence, hydrate nucleation becomes plausible as the methane solubility approaches ~0.05 because the correspondent average methane – methane distance, 8.4 Å, is less than the distance at which the energy barrier to adsorption on a hydrate cage is located (~8.8 Å). On the basis of this hypothesis, hydrate nucleation could occur in three of our systems (P_{bulk} = 18.94, 22.79, or 27.61 MPa) as these system reach the methane solubility value of ~0.05 (see Table 6.2).

Table 6.2. Tangential pressure and solubility of methane in liquid water confined in the silica pore as obtained from our equilibrium simulations.

P_{bulk} (MPa)	P_{pore} ($P_{xx} = P_T$) (MPa)	Solubility × 10^3
6.29	18.65	9.7
9.30	22.75	10.1
12.17	31.26	10.8
15.22	36.51	27.8
18.94	36.99	55.3
22.79	41.21	51.5
27.61	44.59	54.8

6.4.4 Probability of Hydrate Formation inside the Pore

To quantify the possible formation of methane hydrates within the narrow 1 nm silica pores considered here, we computed the F4 structural order parameter [219].

For this calculation we considered the H_2O molecules found within 5.45 Å from each methane molecule (the first peak of the in-plane methane-water oxygen RDFs $g_{CH4\text{-}OW}(r)$) in region I, and we followed the procedure described in Appendix C. When the F4 order parameter is larger or equal to ~0.7, a hydrate cage is considered formed around the given methane. Statistics were obtained during the last 2 ns of simulation time for the seven simulated systems. The analysis gave us the probability of observing 1, 2, 3, etc. hydrate cages. The results are presented in the left panel of Figure 6.7.

Our results show that the probability of observing methane hydrate cages is high when P_{bulk} = 18.94 MPa. At these conditions, in fact, the methane solubility in confined water approaches ~0.05. Unexpectedly, although the methane solubility obtained when P_{bulk} = 22.79 MPa and P_{bulk} = 27.61 MPa is also ~0.05, the probability of observing methane hydrate cages is lower than that obtained for P_{bulk} = 18.94 MPa. This difference could be due to low statistical accuracy in our analysis, perhaps due to the higher tangential pressure under confinement.

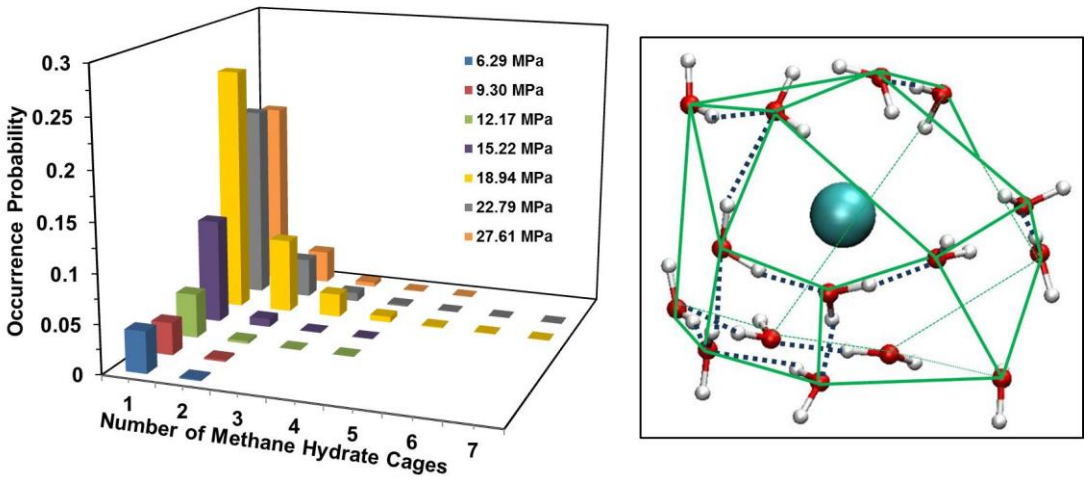

Figure 6.7. (Left) Probability of observing the methane hydrate cages found in seven simulation systems. We report on the X-axis the number of methane hydrate cages found in seven simulation systems with various bulk pressures. (Right) A representative simulation snapshot of one selected methane hydrate cage found in the system of P_{bulk} = 18.94 MPa at a specific simulation time. The color schemes for water molecules and methane molecule are the same as those used in Figure 6.1. Dark blue dotted lines represent hydrogen bonds formed between water molecules in the hydrate cage. The green lines connect contiguous water molecules on the hydrate cage.

Despite the fact that the probability of observing hydrate cages in our systems is substantial, we point out that these cages are very short lived, with lifetimes shorter than ~0.2 ps. This suggests that perhaps large hydrates are not stable within the narrow pores considered here (1 nm in width). It is also possible that the hydrate structures we observe are much smaller than the expected critical nucleus size at 300K [180], and therefore hydrates cannot grow during our simulations. Because the arrangement of water molecules on the silica surface is hexagonal (see Figure 6.5), if hydrates form within the pores they should be of either tetrakaidecahedron of hexakaidecahedron geometries ($5^{12}6^2$ or $5^{12}6^4$ cages, respectively). However, the narrow pores considered here might frustrate the formation of hydrates. In the right panel of Figure 6.7, we show one representative simulation snapshot representing one methane hydrate cage as obtained in our simulations (obtained at P_{bulk} = 18.94

MPa). We note that the structure of the cage is amorphous, which is thoroughly different from the structure of common hydrate cages (pentagonal dodecahedral 5^{12}, tetrakaidecahedron $5^{12}6^2$ or hexakaidecahedron $5^{12}6^4$). The results in Figure 6.7 suggest a formation of incomplete methane hydrate cages with very short lifetime occurred for our systems. It remains to be determined whether pores of slightly different width might favour the formation of hydrates.

6.5 Concluding Remarks

In summary, the solubility of methane in liquid water confined between two silica slabs versus the bulk pressure was studied using molecular dynamic simulations. We found a large increase in methane solubility in confined water. This result cannot be explained solely by the increased tangential pressure due to confinement, and it is probably related to the structure of confined water. The highest methane solubility observed in our simulations is consistent with that required for onset of hydrates formation, according to the cage adsorption hypothesis of Guo et al. [220]. Indeed, analysis of our simulation snapshots reveals the frequent formation of amorphous water cages that contain methane. In addition to suggest that confinement might enhance hydrates formation, our results could help the development of technologies of wide societal importance, including hydraulic fracturing, in which high-pressure water comes in contact with hydrocarbons and natural gas confined in narrow pores.

Chapter 7 Factors Governing the Behaviour of Aqueous Methane in Narrow Pores

The material presented in this section was published in 2015 in volume 374, pages 20150019 of Philosophical Transactions of The Royal Society A Mathematical Physical and Engineering Sciences.

7.1 Abstract

All-atom equilibrium molecular dynamics simulations were employed to investigate the behaviour of aqueous methane confined in 1 nm-wide pores obtained from different materials. Models for silica, alumina, and magnesium oxide were used to construct the slit-shaped pores. The results show that methane solubility in confined water strongly depends on the confining material, with silica yielding the highest solubility in the systems considered here. The molecular structure of confined water differs within the three pores, and density fluctuations reveal that the silica pore is effectively less 'hydrophilic' than the other two pores considered. Comparing the water fluctuation autocorrelation function to local diffusion coefficients of methane across the hydrated pores we observed a direct proportional coupling between methane and water dynamics. These simulation results help to understand the behaviour of gas in water confined within narrow sub-surface formations, with possible implications for fluid transport.

7.2 Introduction

It is known that structural and dynamical properties of confined water are strongly affected by the solid substrate characteristics, yielding different behaviours compared to those observed in the bulk [100]. Several attempts have been made to relate the behaviour of water molecules near an interface to hydrophobic/philic

features at sub-nanometer resolution. We explore here whether small changes in surface properties can yield marked differences in the effective hydrophobic vs. hydrophilic features of a narrow pore. The feature of interest is the methane solubility in confined water, which is directly related to hydraulic fracturing applications. In a recent contribution we reported that methane solubility in water increases significantly when water is confined in slit-shaped pores of width 1 nm carved out of silica [221]. This investigation will clarify whether the features of the confining material are essential for this observation, or instead if the pore size is the most important parameter. To quantify the molecular features of confined water we investigate its structure, and its density fluctuations, building on recent progress in the field [99, 222, 223].

In this study, we report equilibrium MD simulations for methane – water mixtures confined within 1 nm slit-shaped nanopores in equilibrium with bulk methane. In addition to solubility and structure, we also quantify the mobility of methane within the three pores of interest. The simulations are conducted at the temperature T=300K, and at bulk pressures P_{bulk} in the range from ~6 to 82 MPa. Silica, alumina, and MgO were used as solid substrates because they are fundamental components of many minerals found in the subsurface. In the remainder of the article we first introduce the simulation methodology; we then discuss the results, i.e., methane solubility, fluid structure, density fluctuations, and mobility; we finally summarize our main results.

7.3 Simulation Methodology

Aqueous methane confined in silica, alumina, and MgO narrow pores was studied by all atom MD simulations using the package GROMACS [68, 131]. Two slabs of each type of pore material facing each other across the pore volume along

the Z direction yield slit-shaped pores. The silica slabs were constructed to reproduce β-cristobalite SiO_2 [18, 20, 31, 221]. Alumina pore surfaces were modelled as crystallographic faces of sapphire α-Al_2O_3 (space group $R\bar{3}c$), C plane (0001) [19, 224]. Each MgO slab was derived from the space group *Fm3m* along the (001) plane [75, 88]. All the non-bridging oxygen atoms on the silica and alumina surfaces were protonated, while the MgO surfaces were not hydroxylated, as suggested by theoretical and experimental observations [18, 31, 87]. In a prior simulation we detailed the behaviour of pure water supported on free-standing solid surfaces obtained from these three model materials [225]. Each of the two surfaces placed parallel to the X-Y plane of the simulation box and across the pore volume is of dimensions 104.05×100.8, 91.35×90.68, and 103×105.1 $Å^2$ for the systems of silica, alumina, and MgO, respectively. The simulation box is periodic in the three directions. The Y dimension of the simulation boxes reflects the periodicity of the solid crystalline substrate; the X and Z dimensions were set to 224.78 Å – 42.92 Å, 180.43 Å – 33.82 Å and 185.1 Å – 33.12 Å for silica, alumina and MgO systems, respectively. All simulations were carried out for pores of width 10 Å (the pore width refers to the shortest center-to-center distance between surface oxygen atoms of the solid slabs across the pore volume). Due to periodic boundary conditions, the nanopores are effectively infinite along the Y direction. On the contrary, the pores are finite along the X direction, along which they are exposed to "bulk" systems. The simulation setup mimics the one implemented in the previous study [221].

The initial configurations for the three systems are built with water and methane molecules placed outside the slit pore, in the bulk region. As the simulation progresses, water and methane fill both the pore and the bulk volume. The number of methane molecules was varied from 1000 to 4000 while the number of water

molecule was fixed at 3300, 1000 and 1500 for the silica, alumina, and MgO systems, respectively. These different amounts of water molecules were chosen because they were sufficient to fill approximately half of the pore volume along the X direction. By changing the number of methane molecules we manipulated the bulk pressure, which we estimated for each system after equilibrium was achieved, using the Peng-Robinson equation of state from the pure methane density of molecules in the bulk gas phase [197]. The calculated bulk pressures for various CH_4-H_2O system compositions are shown in Table 7.1.

Table 7.1. Bulk phase pressure estimated for seven methane-water systems simulated at T=300K.

System Composition	Estimated Bulk Pressure (MPa)		
	Silica (3300 H_2O)	Alumina (1000 H_2O)	Magnesium Oxide (1500 H_2O)
1000 CH_4	6.3	9.3	9.6
1500 CH_4	9.3	14.7	14.9
2000 CH_4	12.2	21.4	21.2
2500 CH_4	15.2	29.8	28.9
3000 CH_4	18.9	41.7	40.0
3500 CH_4	22.8	58.2	55.0
4000 CH_4	27.6	82.4	76.1

The CLAYFF force field was implemented to describe the three narrow pores [65]. Silicon, aluminum and oxygen atoms were held at fixed positions while the surface hydrogen atoms of the –OH groups were allowed to vibrate; all atoms in the MgO substrate were kept rigid. At the simulated conditions (P up to 80 MPa and ambient T) many studies reported no significant structural distortions within the

substrates considered here until pressures exceeding 10's of GPa are reached [226-233]. We therefore consider it reasonable to maintain the pore models rigid (except for –OH vibrations) in our simulations. The OPLS-UA was implemented to model methane [66], and the rigid SPC/E model was used to simulate water [67]. The SPC/E water bonds and angles were kept fixed by employing the SETTLE algorithm [70]. Non-bonded interactions were modelled by means of dispersive and electrostatic forces. The electrostatic interactions were modelled by the Coulombic potential. Dispersive interactions were modelled with 12-6 Lennard-Jones potentials. The Lennard-Jones parameters for unlike interactions were determined by the Lorentz-Berthelot combining rules [64] from the values of like components. The cutoff distance for all interactions was set to 9 Å. Long-range corrections to electrostatic interactions were treated using the PME method [94].

All simulations were performed in the canonical ensemble (NVT) where the number of particles (N), the simulation volume (V), and the temperature (T) were kept constant. The simulated temperature was maintained at 300 K controlled by Nose-Hoover thermostat [95, 96] with a relaxation time of 100 fs. The equations of motion were solved by implementing the leapfrog algorithm [97] with 1.0 fs time steps. The total simulation time was 49 ns. Data analysis was conducted over the last 2 ns of the simulations, after 47 ns of equilibration were completed. Equilibration was considered achieved when the density of methane within the pore approached a constant value that did not change appreciably over 13 ns.

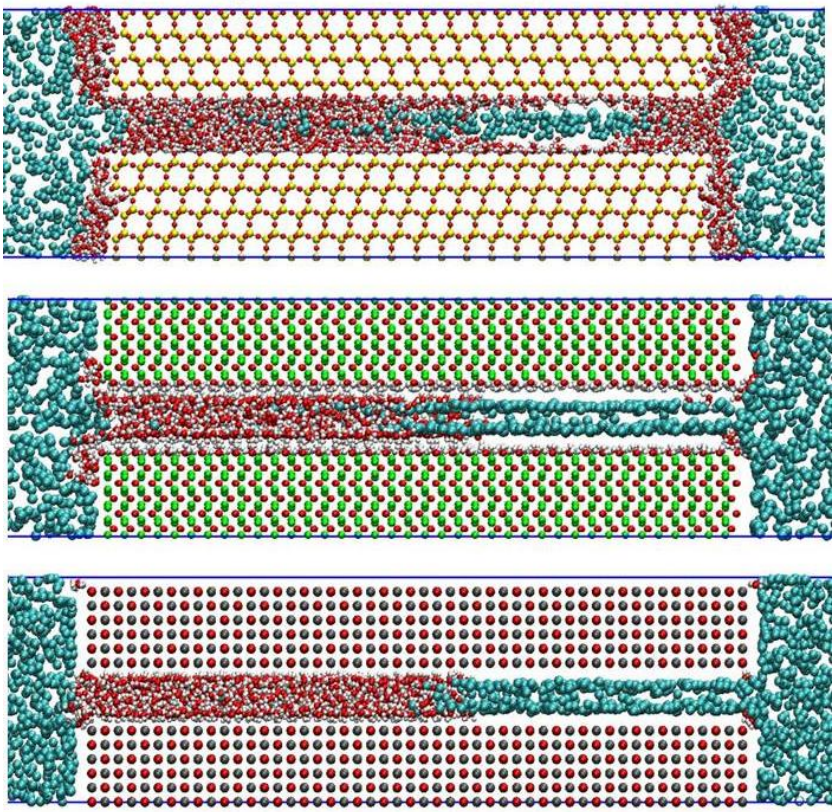

Figure 7.1. Representative simulation snapshots for aqueous methane in slit-shaped silica (top panel), alumina (middle panel) and MgO (bottom panel) pores of width 1.0 nm. Red, white, cyan, yellow, green and gray spheres represent oxygen, hydrogen, methane, silicon, aluminum and magnesium atoms, respectively.

7.4 Results and Discussion

7.4.1 Methane Solubility

The final configurations obtained for aqueous methane confined in the silica (top), alumina (middle) and MgO (bottom) pores at 300K after 49 ns are shown in Figure 71. For all simulated systems water occupies approximately half of the pore volume, and methane occupies the remainder of the pore and most of the bulk. Similar to the systems confined in our previous study (as presented in Chapter 6), focused on silica pores, an interface is observed between the water-rich and the methane-rich phases within the alumina and MgO pores. We identify as Region I the

pore volume occupied mostly by water with methane dissolved in it (left in Figure 7.1); Region II is the pore volume occupied mostly by methane (right in Figure 7.1). A significant difference in the distribution of water and methane in Region II within the three pores is observed: within the silica pore water wets the surfaces and methane occupies the pore center, while in alumina and MgO pores only methane molecules occupy the whole Region II. Water at contact with the silica surface within Region II is able to form hydrogen bonds with the surface –OH groups available on this substrate, as described elsewhere [225]. This is not possible on the other two substrates, where the density of adsorption sites is too large (i.e., while the density of –OH groups is 4.54 per nm^2 on silica, the surface density of OH groups is of 15 per nm^2 on alumina and the surface density of Mg atoms is of 14 per nm^2 on the MgO substrate). The Region I – Region II interface that can be seen roughly parallel to the Y direction of the simulation box is irregular in shape (not shown for brevity). The irregularity of the Region I – Region II interface, the presence of water molecules on the pore opening from Region II to the bulk system, and the presence of water molecules near the silica surface cause the methane molecules confined in Region II of the silica pore in Figure 1 appear disordered. While the methane distribution would change with variations in the amount of water simulated in this system, as well as upon variations in pore width, we have not varied the size of the simulation box in this investigation.

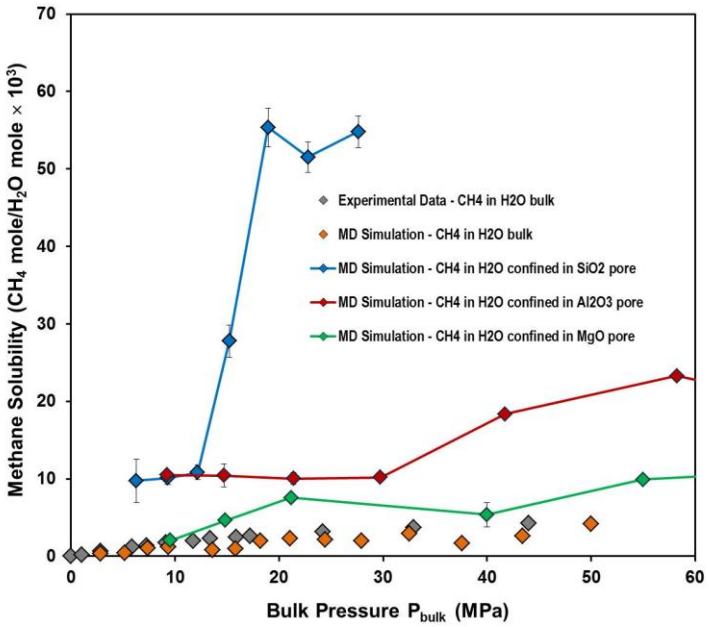

Figure 7.2. Methane solubility in confined water as a function of bulk pressure. Simulation data for aqueous CH_4 confined in silica, alumina, and MgO pores are shown as blue, red, and green diamonds, respectively. Lines are guides to the eye. Simulated bulk CH_4 solubility data in liquid water at 298K as reported by Sakamaki et al. [210] are shown as orange diamonds. The corresponding experimental data [211-213] for CH_4 in bulk water are shown as gray diamonds.

Following our prior work (as presented in Chapter 6), we computed the methane solubility in the confined water within Region I in the three pores. It is worth repeating that for these calculations we only consider the water-methane mixture in Region I. The results are shown in Figure 7.2, in which methane solubility is shown as a function of bulk pressure. The bulk pressure is estimated from the methane density using an equation of state (see Table 7.1). The blue, red, and green symbols are the results of methane solubility in water confined in silica, alumina, and MgO pores at 300K. We also report the methane solubility in bulk liquid water at 298 K as predicted, using simulations, by Sakamaki et al. [210] (orange symbols) as well as the correspondent experimental data from literature [211-213] (gray symbols). The results in Figure 7.2 are consistent with a significant increase of methane solubility in water due to confinement. The enhancement of methane solubility is likely due, in

part, to the enhanced pressure in the pore. However, as we discussed in our previous work, this increased pressure is not sufficient to explain the high solubility predicted in confinement. Comparing the methane solubility in confined water within the three pores, we observe that the results obtained in the silica pore are much higher than those found within the alumina and MgO pores, with the results obtained in the MgO pores showing the lowest solubility out of the three confined systems considered. In addition to differences in pressures within the pores, it is also possible that the distinct structure of confined water within the three pores is responsible for the results observed. We also note that the methane solubility estimated from our simulations show large variations upon relatively small changes in bulk pressure. While we attribute these changes to statistical uncertainty, it is possible that other factors play important roles (e.g., the structure and the density fluctuations of confined water).

7.4.2 Structure of Confined Fluids - Methane and Water

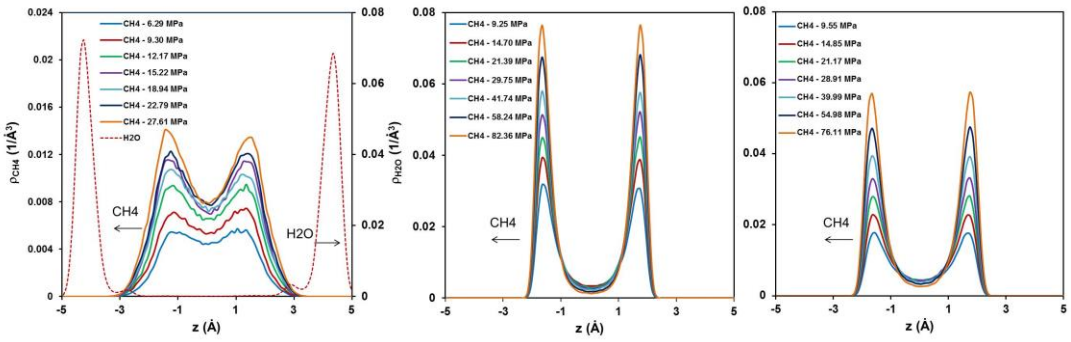

Figure 7.3. Density profiles of water oxygen atoms (dotted curve) and methane molecules (continuous curves) in Region II as a function of the distance z across the silica (left), alumina (middle), and MgO (right) pores. The results are obtained from seven simulation systems for each pore. The reference (z=0) corresponds to the center of the pore.

It is worth noting that the tangential pressure in the pore is directly proportional to the methane density in the pore, as discussed in previous studies [217, 221]. In Figure 7.3 we report the molecular density of methane in Region II along the direction perpendicular to the pore surface within the silica (left), alumina (middle), and MgO (right) pores as the bulk pressure increases. The reference (z=0) corresponds to the center of the pore. The results show that generally the increase of bulk pressure increases the molecular density of methane in Region II for all three pores. Comparing the methane density confined within three pores, we find that the methane densities in the silica pores are much smaller than those found in the alumina and MgO pores, which indicates that the tangential pressures in the silica pore are also much smaller. However, the methane solubility in water confined in the silica pore is much higher than that found for the two other pores (see Figure 7.2). These results suggest that the differences in the methane solubility are probably related to the distinct structural behaviour of confined water in the silica pore compared to the alumina and MgO pores. However, the higher methane solubility in water confined in the alumina pore than in the MgO pore is likely due to the higher tangential pressure, as suggested by the higher methane density in Region II (compare the data in middle and right panels in Figure 7.3 for systems at comparable bulk pressure). For completeness, we also report the water density profiles within the three pores. As mentioned above, water wets the silica surface, yielding a very dense molecular layer near the solid surfaces, while it is essentially not present within the other two pores considered here.

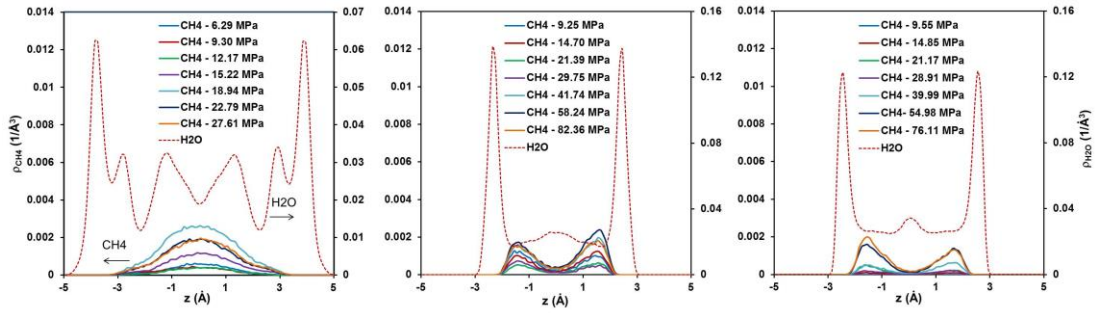

Figure 7.4. Density profiles of water oxygen atoms (dotted curves) and methane molecules (continuous curves) in Region I as a function of the distance z across the silica (left), alumina (middle), and MgO (right) pores. The results are obtained from seven simulation systems for each pore. The reference (z=0) corresponds to the center of the pore.

In Figure 7.4 we present the methane density profiles within Region I for the three pores considered as a function of bulk pressure. Generally, the molecular density of methane in Region I increases as the bulk pressure increases. The results suggest that methane molecules are always excluded from the two hydration layers near the solid surfaces in all hydrated pores; while methane molecules accumulate in a rather wide region near the center of the silica pore, they yield two layers off-center of alumina and MgO pores. For completeness, we also report the density profiles for water in the same region. The results for the density profiles of water oxygen atoms within Region I for the three pores show that more well-defined hydration layers are observed in the silica pore compared to two other pores. It is worth pointing out that methane molecules always accumulate in correspondence of density minima identified by the water density profiles.

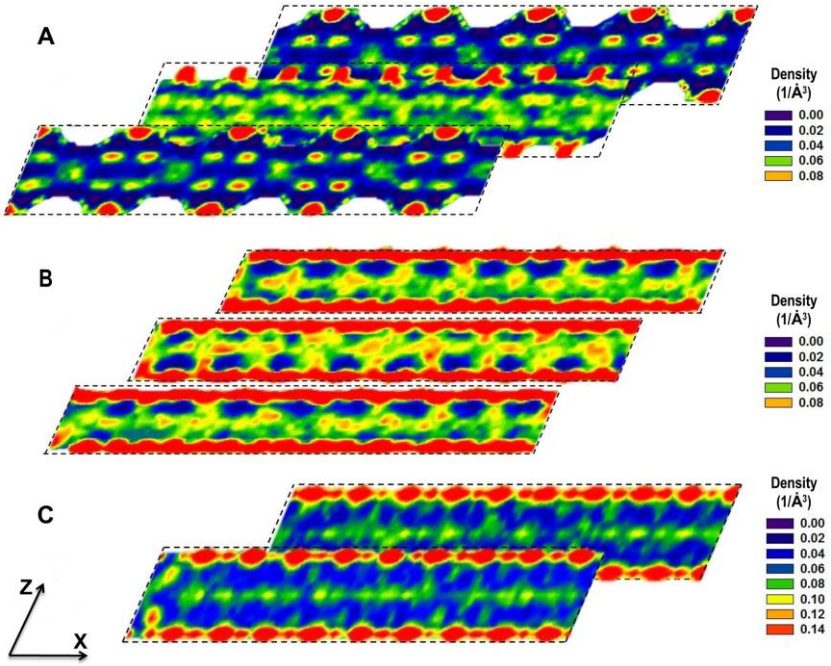

Figure 7.5. In-plane density distributions of water oxygen atoms found in layers parallel to the X – Z plane at several locations along the Y direction within silica (panel A), alumina (panel B) and MgO (panel C) pores. The results are obtained from systems containing only water. Densities are expressed in number of molecules per cubic angstrom. The consecutive layers were located at the following positins along the Y direction: for the silica pore the three layers were from 3.75 Å to 4.75 Å, from 4.75 Å to 5.75 Å, and from 5.75 Å to 6.75 Å; for the alumina pore the three layers were from 10 Å to 12 Å, from 12 Å to 14 Å, and from 14 Å to 16 Å; for the MgO pore the two layers were from 9 Å to 11 Å and from 11 Å to 13 Å.

Analysis of the distributions of water molecules within three pores could allow us to gain better insights into the structure of confined water. We calculated the in-plane density distributions of water oxygen atoms found in layers parallel to the X – Z plane at several locations along the Y direction. In Figure 7.5 we report the results obtained for silica (panel A), alumina (panel B) and MgO (panel C) pores. The results are obtained from systems containing water only. The high-density areas (red-green spots) of the contour plots indicate the positions where the water oxygen atoms preferentially reside. Visual inspection of the results suggests a significant difference in the structural properties of confined water. Specifically, water molecules spread on

the silica surfaces yielding small volumes depleted of water (as seen in the panel A) while they fill the alumina and MgO pores thoroughly, forming two well-defined hydration layers in contact with the surfaces (panels B and C). These distributions indicate that cavities are stably formed only in the hydrated silica pore while they are not typically present in the other hydrated pores.

7.4.3 Water Density Fluctuations under Confinement - Degree of Hydrophobicity

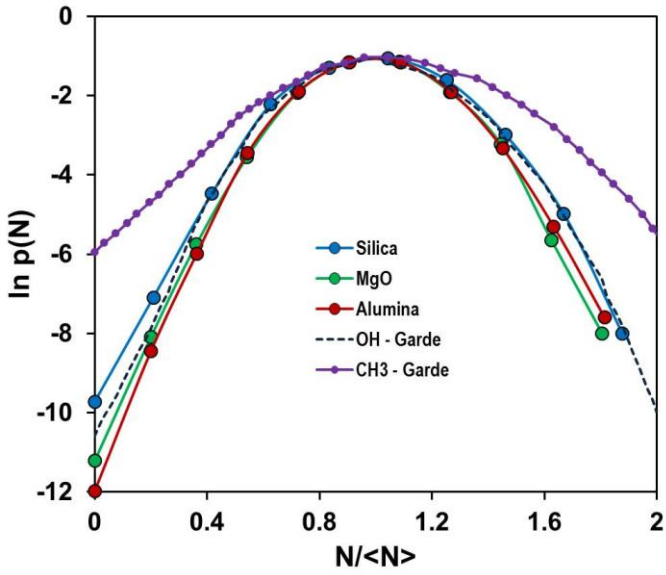

Figure 7.6. Probability distribution for observing N water molecules, p(N), in a small spherical observation volume (r = 3.3 Å) located at the center of the hydrated silica (blue), alumina (red), and MgO (green) pores. The results are obtained from the systems containing only water in the nanopores.Results for observing N water molecules in the same probe volume next to hydrophilic OH (black dashed) and hydrophobic CH_3 (purple) surfaces reported by Garde et al. [99] are shown for comparison.

To quantify the differences in the behaviour of confined water, which might result in differences in methane solubility, we quantify the water density fluctuations within the hydrated pores. Specifically, we calculated the probability of observing N molecules within a small spherical observation volume ν of radius r = 3.3 Å located

at the center of the hydrated silica (blue), alumina (red), and MgO (green) pores. The probabilities are calculated as [223]:

$$\boldsymbol{P_v(N) = \langle \delta(N_v - N) \rangle = \lim_{t\to\infty} \frac{1}{t} \int_0^t dt' \delta(N_v(t') - N)} \quad (7.1)$$

Garde and coworkers [222] showed that the spontaneous formation of cavities within hydration water is a strong signature that discriminates among surfaces of different degrees of hydrophobicity. Other quantities such as local averaged water density and contact angle do not seem sufficient to provide such a discriminant [225]. In Figure 7.6 we show the results for the calculations of eq. (7.1) within the three hydrated pores considered here. The results are compared to similar calculations reported in the literature for water on free-standing surfaces of varying degrees of hydrophobicity. Comparing the data, we observe that the three pores considered in this work can be considered 'hydrophilic'; however, there is a clear difference in their relative degree of hydrophilicity, with the silica pores being less 'hydrophilic' than the other two pores considered. This observation could explain why methane is more favourably adsorbed within the hydrated silica pore than in the other two pores. Comparing the results obtained for the alumina with those found for MgO pores, we notice that the alumina pore is slightly more 'hydrophilic' than the MgO pore. This does not agree with the slightly larger methane solubility observed in water confined in the alumina vs. the MgO pore. In this case, the differences in tangential pressure, suggested by the differences in methane densities in Region II (see Figure 7.3) seem to be responsible for the differences in methane solubility. Garde et al. [99] stated that one important and direct consequence of enhanced fluctuations at an interface is that the formation of a cavity near that interface is easier. The results of the water distributions within the three pores reported in Figure

7.5 indeed confirm the observation of cavity formation within the hydrated silica pores while we do not see the cavities in the two other hydrated pores.

7.4.4 Coupling of Methane Dynamics to Hydration Fluctuations

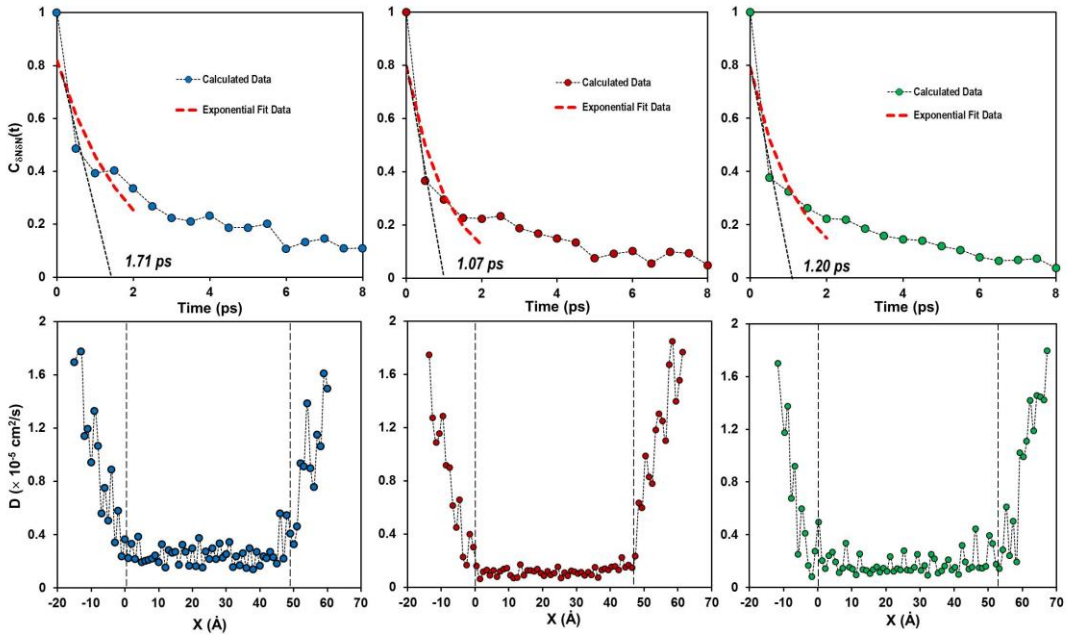

Figure 7.7. (Top) Normalized water fluctuation autocorrelation function $C_{\delta N \delta N}(t)$ in the silica (left), alumina (middle), and MgO (right) pores. The results are obtained from systems containing only water. (Bottom) Diffusion profiles for methane across the hydrated silica (left), alumina (middle), and MgO (right) pores. The results were obtained from the systems containing water fully occupying the pores and one methane molecule constrained at the center of the simulation box in Y-Z plane while it moves along the X direction. The region between two dashed lines represents the inner hydrated pore.

To further quantify the mutual relation between methane behaviour and confined water properties, we analysed the normalized water fluctuation autocorrelation function $C_{\delta N \delta N}(t)$ within the three pores and the methane diffusion profiles inside the hydrated pores. The results are shown in the top and bottom panels of Figure 7.7, respectively, for silica (left panels), alumina (middle panels) and MgO (right panels) pores. We computed the normalized water fluctuation autocorrelation function

through the water occupancy *N(t)* in the probe volume ν (r = 3.3 Å) located at the center of the hydrated pores, defined as [234]:

$$\boldsymbol{C_{\delta N \delta N}(t) = \frac{\langle \delta N(t) \delta N(0) \rangle}{\langle \delta N(0) \delta N(0) \rangle}} \qquad \text{with } \delta N(t) = N(t) - \langle N \rangle \qquad (7.2)$$

The local diffusion coefficients for methane were estimated from umbrella sampling trajectories according to a simplified form of the Woolf and Roux equation [235, 236]:

$$\boldsymbol{D(x = \langle x \rangle) = \frac{var(x)}{\tau_x}} \qquad (7.3)$$

where ⟨x⟩ is the average position of the harmonically restrained methane molecule along the X direction, var(x) = $\langle x^2 \rangle - \langle x \rangle^2$ is its variance, and τ_x is its correlation time, formally defined as

$$\boldsymbol{\tau_x = \frac{\int_0^\infty \langle \delta x(t) \delta x(0) \rangle dt}{\langle \delta x^2 \rangle}} \qquad \text{with } \delta x(t) = x(t) - \langle x \rangle \qquad (7.4)$$

For the diffusion calculations, the methane molecule is forced to remain at the center of the simulation box in the Y-Z plane while it moves along the X direction. The x = 0 is located at the pore entrance.

From single exponential fits on the normalized water fluctuation autocorrelation function we find that the decay time of water fluctuations in the three pores decreases in the order silica (~1.71 ps), MgO (~1.20 ps) and alumina pore (~1.07 ps). This means that the hydration fluctuation in the pore increases in the order alumina < MgO < silica pore, which is consistent with the density fluctuation results in Figure 7.6. Note that the exponential fitting to the autocorrelation functions is only conducted at short observation times (less than 2 ps), where a single exponential function is assumed to be sufficient to capture the system behaviour. The decay time

obtained for the normalized water fluctuation autocorrelation function next to hydrophilic surfaces is comparable to that reported for bulk water by Setny et al. [234]. Note that the characteristics of water density fluctuations next to hydrophilic surfaces are similar to those obtained for bulk water [99].

In the bottom panels of Figure 7.7, we show the diffusion profiles of the methane molecule across three hydrated pores. The estimated diffusion coefficients decrease as methane enters the hydrated pore. The calculated diffusion coefficient of methane outside the hydrated pores (~ 1.8×10^{-5} cm^2/s) is consistent with the experimental diffusivity of methane in bulk water at similar conditions (1.9×10^{-5} cm^2/s) [237]. The results of averaged diffusion coefficients of methane inside the hydrated pores (the region between two dashed lines) suggest that methane diffuses faster in the hydrated silica pore (~ $2.45 \pm 0.03 \times 10^{-6}$ cm^2/s) than in the alumina (~ $1.12 \pm 0.02 \times 10^{-6}$ cm^2/s) and MgO (~ $1.61 \pm 0.03 \times 10^{-6}$ cm^2/s) pores. Correlating the methane diffusion with the hydration fluctuations in the silica, alumina and MgO pores clearly indicates a direct proportional coupling between methane and water dynamics.

7.5 Conclusions

We employed molecular dynamics simulations to study the behaviour of methane dissolved in water confined within silica, alumina, and MgO pores with 1 nm width. The methane solubility in confined water in the silica pore is much higher than that found in the two other pores at comparable T and P. This is due to the fact that the hydrated silica pore is less ‘hydrophilic’ than the other two pores considered. Despite the fact that the hydrated alumina pore is slightly more hydrophilic than the hydrated MgO pore, methane solubility in water confined in the alumina pore is slightly larger than that obtained in the MgO pore. This difference is probably due to

higher tangential pressure expected in the alumina pore. Analysis of water fluctuation autocorrelation functions and local diffusion coefficients of methane across the hydrated pores shows a direct proportional coupling between methane and water dynamics. These results suggest that the properties of confined water are dictating both structural and dynamic behaviour of methane dissolved in the hydrated pores. Implications in the diffusion of fluids in the sub-surface should be investigated in the framework of hydraulic fracturing, shale gas, and perhaps also carbon sequestration.

Chapter 8 Summary and Outlook

Learning fundamental insights regarding the behaviour of hydrogen-bonding fluids or their mixtures near mineral surfaces or within porous matrices helps us relating to multiple practical applications such as nano-fluidic devices, water desalination, membrane-based separations, natural gas sweetening, shale gas production, gas hydrate control, etc.

This thesis has provided molecular-level insights into the structural and dynamical properties of water, ethanol and aqueous hydrocarbon mixtures on various free-standing solid surfaces or confined in porous matrices by employing all-atom equilibrium molecular dynamics simulations.

In Chapter 3 we have compared the properties of water within thin films supported on magnesium oxide when its atoms are frozen versus when they are allowed to vibrate. Analysis of the contact angle for droplets of 1000 water molecules on the substrate, it shows better agreement with experimental data when the substrate is treated as rigid. The structural and dynamical properties of interfacial water on rigid versus vibrating MgO did not display significant differences, except the water orientation within the first hydration layer. We have also compared with those reported earlier for water on alumina, and on silicon dioxide surfaces. We observed a well-ordered pattern of interfacial water, especially on the first hydration layer, on all the three substrates considered. The arrangement of solid atoms on the substrate governs the availability of preferential adsorption sites where water molecules occupy. Depending on the distribution of these preferential adsorption sites on the surface the planar distribution of water molecules at the interface, and the network of water-water HBs are formed. These decide how far the surfaces perturb the properties of interfacial water and impact the residence time of water molecules

near the solid substrates. Despite the lack of experimental validations, the results of this work are important to gain insights into macroscopic phenomena including ion adsorption/desorption processes on solid substrates and hydrodynamic properties in the earth subsurface.

In Chapter 4 we conducted simulations to study the behaviour of thin liquid ethanol films supported on the C-plane and R-plane alumina surfaces at ambient conditions. By computing atomic density profiles, in-pane RDFs, planar density distributions and HB networks it shows a well-organized ethanol layer near the alumina surface, resembling the structure of the substrates and the probability of forming HBs with the surface hydroxyl groups. We observe a pronounced orientational order in the first adsorbed layer on both surfaces. Comparing the simulated preferential orientation of ethanol molecules within the first adsorbed layer on the R-plane with experimental sum frequency vibrational spectroscopy data shows good agreement. Analysis of the dynamical properties suggests that ethanol molecules in the first adsorbed layer hardly move out of this layer, and that their rotational diffusion is impeded compared to the case that they are in the bulk, likely due to preferential HBs with the substrates. The results in this study could play a significant role in widening our understanding regarding the behaviour of hydrogen-bonding and amphiphilic molecules in contact with materials of both technological and geological implications. Several industrial, geophysical, petroleum, and environmental applications employ hydrogen-bonding and amphiphilic molecules at solid surfaces; for example, these molecules could be a technical drilling fluid which is used to lubricate the drill bit and maintain hydrostatic pressure during oil and gas exploration.

In Chapter 5 we have investigated sorption, structure, and dynamics of liquid water-ethanol mixtures confined in 1 nm-wide slit-shaped alumina pores at ambient conditions. The simulated results show the selective adsorption of water within the pores, which is consistent with the experimental data. It is likely due to preferential surface-water interactions, compatible with results on freestanding alumina surfaces. The inspection of the dynamical properties of the confined mixtures indicates that water travels through the narrow pores more quickly than ethanol. The structural and dynamical results presented here for water-ethanol mixtures suggest the opportunity of using alumina-based porous materials as perm-selective membranes for the separation of water from aqueous ethanol solutions.

In Chapter 6 we have studied the behaviour of aqueous methane confined in 1nm-wide silica pore. We observed a significant increase in the solubility of methane in liquid water confined between two silica slabs. The highest methane solubility found in our works is comparable with that required for triggering the hydrate nucleation, based on the cage adsorption hypothesis of Guo et al [188]. Visual inspection of the representative simulation snapshots unveils the constant formation of amorphous water cages in which methane is confined. This suggests that the confinement might increase the possibility of the hydrate formation. In addition, our results regarding the investigation of the properties of mixtures of water and volatile hydrocarbons within porous matrices could give guidance for the development of hydraulic fracturing technologies, in which high-pressure water used as fracturing-fluid stimulates the subsurface formation and encounters hydrocarbons and natural gas confined in narrow pores.

In Chapter 7 we have focused on understanding the impact of porous matrices obtained from different materials on the behaviour of confined aqueous methane.

Models for silica, alumina, and magnesium oxide were employed to create the slit-shaped pores. Our results suggest the strong dependence of methane solubility in confined water on the confining material, in which the methane solubility in liquid water confined in the silica pore is much higher than the other two pores considered here. The difference in molecular structure of confined water within the three pores and in density fluctuations show that the alumina and MgO pores are effectively more 'hydrophilic' than the silica pore. Investigation of the water fluctuation autocorrelation function together with local diffusion coefficients of methane through the hydrated pores reveals a direct proportional coupling between methane and water dynamics. These simulation results could provide useful insights into the behaviour of gas in water confined within narrow porous matrices, with possible significances for fluid transport. Significances in the diffusion of fluids within porous matrices should be examined in the scheme of hydraulic fracturing, shale gas, and possibly carbon sequestration as well.

Continuing the research interests in the fluid transport within narrow sub-surface formations, we will investigate the dynamical properties of gas mixtures across hydrated pores carved out of different solid materials. The solid materials should be obtained from rather stable structures representative of minerals found in the sub-surface, and therefore are expected to be chemically stable for time scales shorter than those at which mineral dissolution processes become relevant. The composition of gas mixtures should resemble that of natural gas including methane, ethane, propane, carbon dioxide and hydrogen sulfide. Our aim is to quantify the selectivity of gas mixture transport through hydrated narrow pores, which could be exploited for the separation of gases, e.g., in natural gas sweetening.

Appendices

A. Supporting Information for Chapter 4

A.1. Force Field Parameters

Table A.1. Force field parameters implemented in this work.

Species	q(e)	ε (KJ/mol)	σ (Å)	Ref	Combining Rules
Al	1.575	5.5639E-06	4.271	[65]	Lorentz-Berthelot combining rules for alumina – alumina surface interactions. $\sigma_{ij} = \frac{1}{2}(\sigma_{ii} + \sigma_{jj})$ $\epsilon_{ij} = \sqrt{\epsilon_{ii}\epsilon_{jj}}$
OB (bridging oxygen)	-1.05	0.65020	3.166		
ON (non-bridging oxygen)	-0.95	0.65020	3.166		
H (surface OH groups)	0.425	0	0		
CH_3 (ethanol)	0	0.732200	3.905	[66]	Geometric combining rules for ethanol – ethanol and ethanol – alumina surface interactions $\sigma_{ij} = \sqrt{\sigma_{ii}\sigma_{jj}}$ $\epsilon_{ij} = \sqrt{\epsilon_{ii}\epsilon_{jj}}$
CH_2 (ethanol)	0.265	0.493712	3.905		
O (ethanol)	-0.7	0.711280	0.3070		
H (ethanol)	0.435	0	0		

A.2. Simulation Snapshots

In Table A.1 we report force-fields parameter implemented in this work to describe ethanol-ethanol as well as ethanol-surface interactions. Parameters include partial charges, as well as size and energy interaction parameters for customary

Lennard-Jones interactions. Different combining rules are employed, as described in the table.

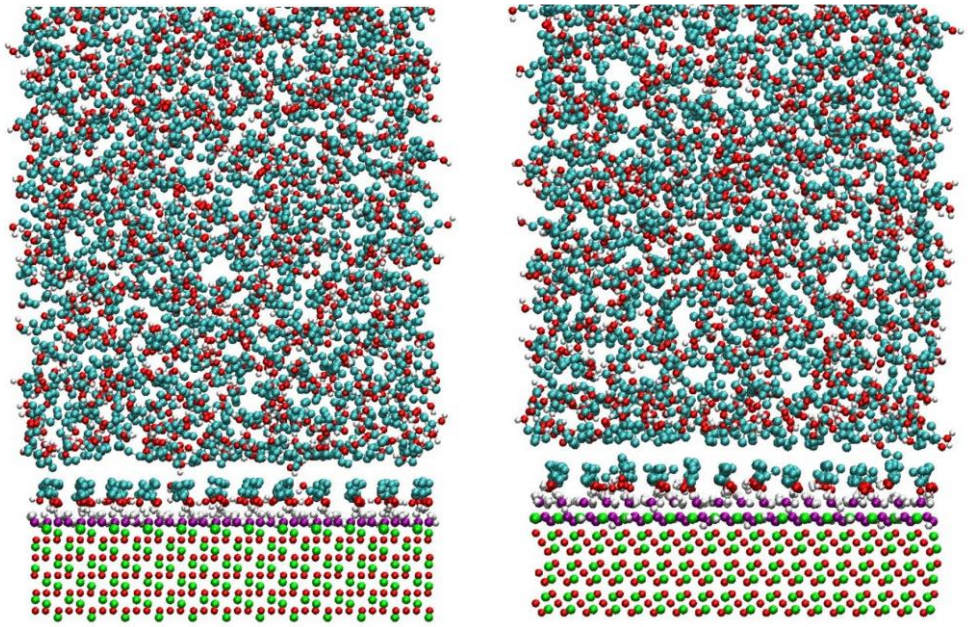

Figure A.1. Simulation snapshots for ethanol on the C-plane (0001) (left) and R-plane ($1\bar{1}02$) (right) sapphire surfaces. Green and red spheres represent aluminum and oxygen atoms in the bulk structure, respectively. For both surfaces, surface hydroxyl groups are illustrated using purple for oxygen and white for hydrogen atoms. Ethanol molecules are represented using cyan, red, and white spheres for methyl (methylene) groups, oxygen and hydrogen atoms, respectively.

In Figure A.1 we show representative simulation snapshots of a thin film of ethanol simulated on the C-plane (0001) (left) and R-plane ($1\bar{1}02$) (right) sapphire surfaces.

A.3. Free Energy Landscapes

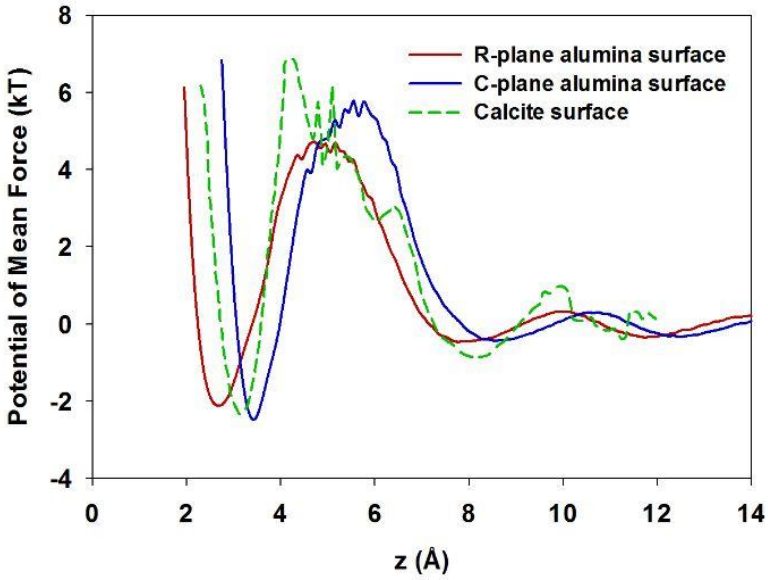

Figure A.2. Potential of mean force for ethanol molecules as a function of the vertical distance from the C-plane (0001) (blue solid curve), the R-plane ($1\bar{1}02$) (red solid curve) of the α-Al_2O_3 and the calcite (green dash curve) surface. Simulations are conducted at ambient conditions for three systems. For the C-plane, the reference (z = 0) corresponds to the top plane of the hydroxyl group oxygen atoms of the substrate; the reference (z = 0) for the R-plane surface is the plane of the topmost oxygen layer and for the calcite surface, the reference (z = 0) corresponds to the top plane of the substrate. Data on calcite are from literature (see text).

In Figure A.2, we present the PMF for ethanol molecules as a function of the vertical distance from the C-plane (blue solid curve) and the R-plane ($1\bar{1}02$) (red solid curve) of α-Al_2O_3. Results are compared to those for ethanol on the ($10\bar{1}4$) plane of calcite (green dash curve) reported by Cooke et al. [126]. The results in Figure A.2 are obtained from the density profiles of the ethanol center of mass, using standard statistical mechanics derivations [126, 136].

A.4. Structural Properties

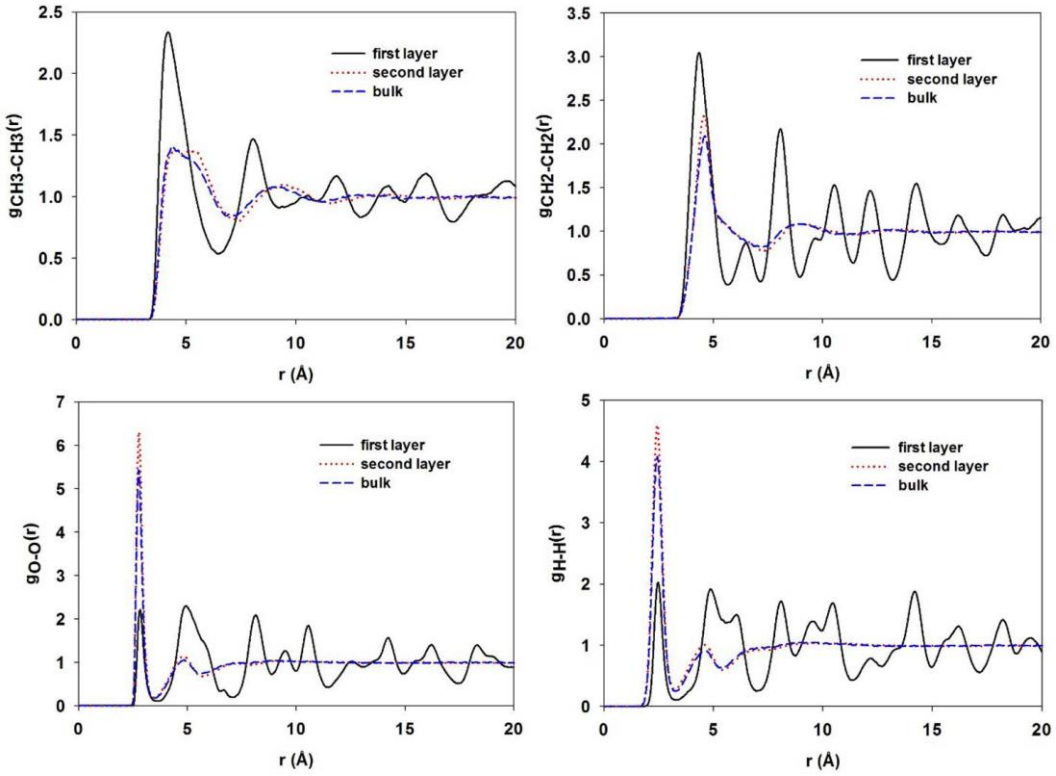

Figure A.3. In plane CH_3 – CH_3 (top left), CH_2 – CH_2 (top right), oxygen-oxygen (bottom left), and hydrogen-hydrogen (bottom right) radial distribution functions for ethanol molecules within various layers on the R-plane.

In Figure A.3, results are presented for in-plane CH_3 – CH_3 (top left), CH_2 – CH_2 (top right), oxygen-oxygen (bottom left), and hydrogen-hydrogen (bottom right) RDFs for ethanol in the first and second layers on the R-plane. Results are also compared to those obtained in the bulk (i.e., far from the surfaces).

As discussed in the text, the RDF results are indicative of pronounced order within the first adsorbed layer. To document such order we calculated the in-plane density distributions of methyl (top left), methylene (top right), oxygen (bottom left), and hydrogen (bottom right) of ethanol molecules within the first adsorbed layer on the C- and R-plane surfaces. The results are reported in Figure A.4 and Figure A.5, respectively.

To further visualize the organization of ethanol molecules within the first adsorbed layer, in Figure A.6 we present top and side views of representative simulation snapshots obtained for ethanol within the first adsorbed layer on the C- (left) and on the R-plane (right) surface.

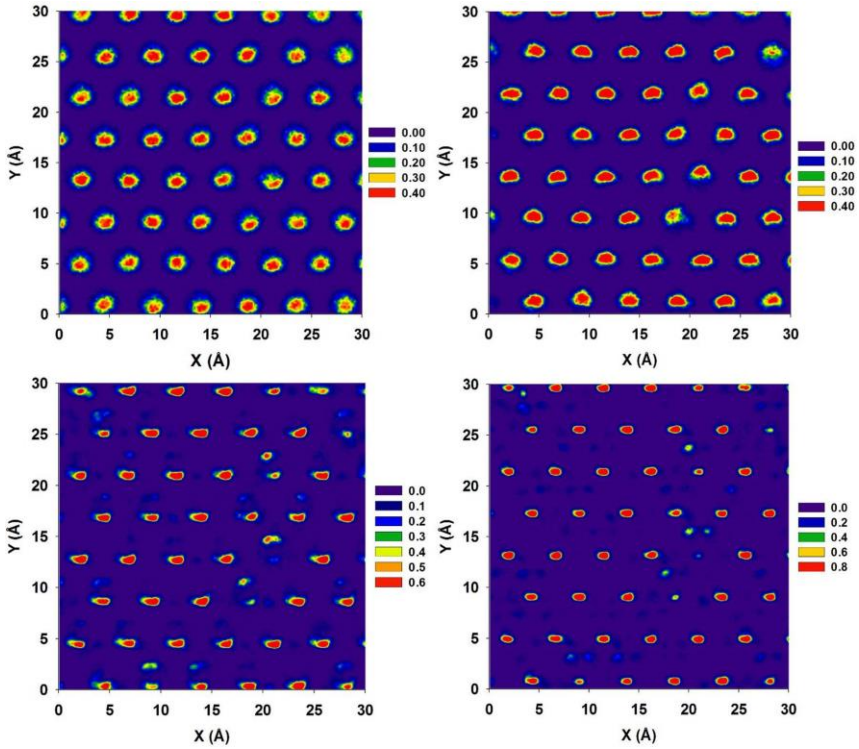

Figure A.4. In-plane density distributions of CH_3 groups (top left), CH_2 (top right), oxygen atoms (bottom left), and hydrogen (bottom right) of ethanol molecules within the first adsorbed layer on C-plane α-Al_2O_3 (0001). Densities are expressed in $1/\dot{A}^3$.

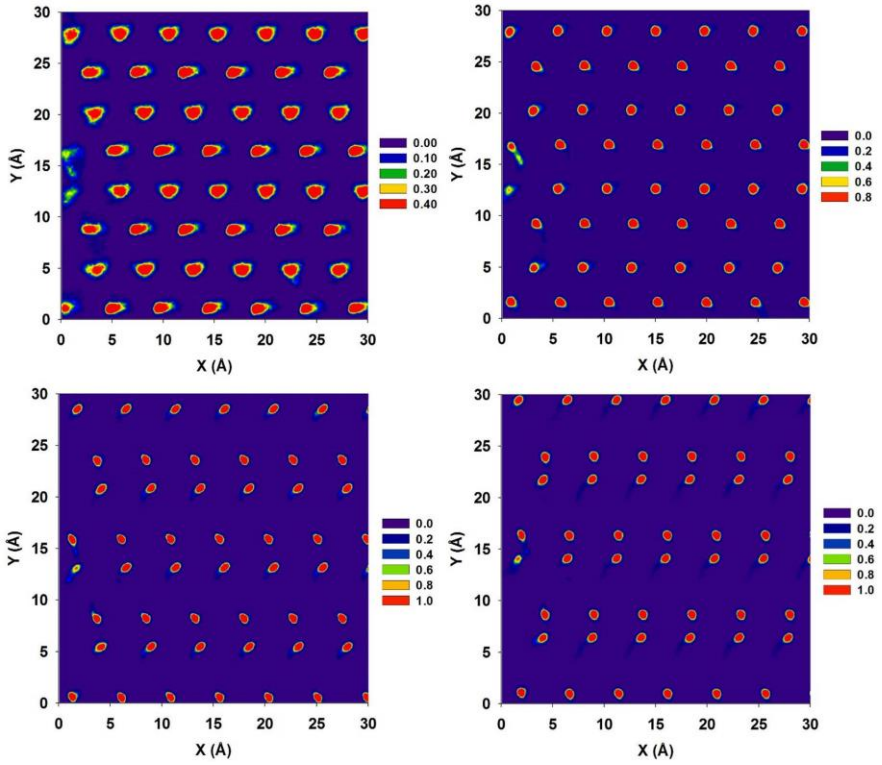

Figure A.5. Same as Figure S4, but for ethanol on R-plane α-Al_2O_3 ($1\bar{1}02$).

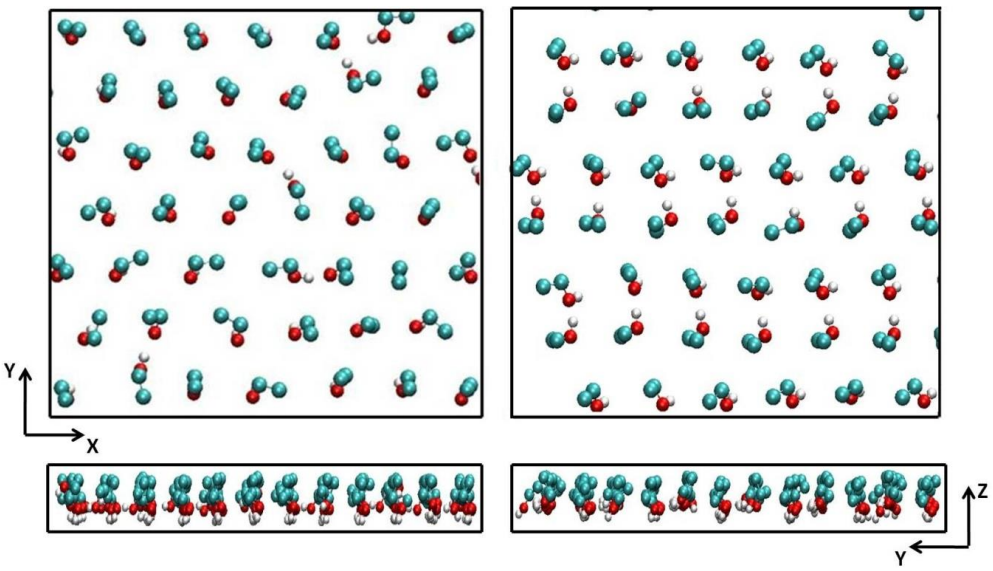

Figure A.6. Top and side views of the first adsorbed ethanol layer on the C- (left) and R-planes (right panel). Ethanol molecules are illustrated using cyan for methyl and methylene groups, red for oxygen, and white for hydrogen atoms.

A.5. Calculation Methods for Ethanol Orientation

We report in Figure A.7 a schematic diagram representing azimuthal and polar angles of the symmetric axis of the methyl group of ethanol and of the OH group with respect to the $(1\bar{1}0\bar{1})$ direction and the surface normal (R-plane), or the (1100) direction and the surface normal (0001) (C-plane). Both all-atom and united-atom representations are used to represent ethanol.

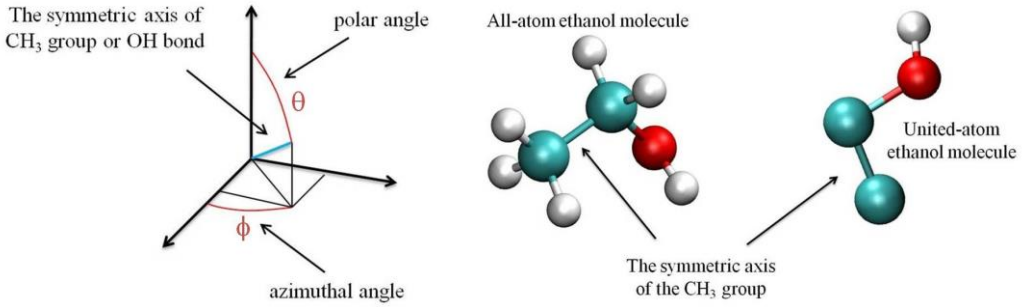

Figure A.7. Left: Schematic diagram representing azimuthal and polar angles of the symmetric axis of methyl group of ethanol or OH group with respect to the $(1\bar{1}0\bar{1})$ direction and the surface normal (R-plane), or the (1100) direction and the surface normal (0001) (C-plane). Right: The symmetric axis of methyl group of ethanol, in all-atom and united atom representations.

B. Supporting Information for Chapter 5

B.1. Algorithms

B.1.1. Algorithm to Calculate the Isosteric Heat of Adsorption at Infinite Dilution

The isosteric heat of adsorption at infinite dilution in the canonical (NVT) ensemble was calculated as [238, 239] $-q = \Delta H = \langle U_1 \rangle_1 - \langle U_0 \rangle_0 - \langle U_g \rangle - RT$, where U_1 is the total energy of the alumina surface with one guest (water or ethanol) molecule present, U_0 is the total energy of only the alumina surface without the guest molecules, $\langle ... \rangle$ refers to an ensemble average at constant volume, temperature and

number of guest molecules, $\langle U_g \rangle$ is the average energy of an isolated guest molecule (without the alumina surface present) and R is gas constant.

B.1.2. Method for Potential of Mean Force Calculations

To construct the PMF as a function of the distance between one molecule and the α-Al_2O_3 (0001) surface, we implemented the umbrella sampling algorithm [72, 240]. The center of mass of molecule was forced to remain at given distances from the substrate using harmonic springs of various elastic constants. For one molecule, 30 independent simulations were conducted, imposing that the equilibrium molecule−surface distance changes by 0.05 nm from one simulation to another. At any separation distance the simulation was conducted for up to 8 ns, during which time the histogram representing the distances between the center of mass of molecule and the substrate was populated [241]. The WHAM algorithm was then used to reconstruct the PMF from combining the histograms obtained at various molecule−surface separations [72].

B.2. Results

B.2.1. Heat of Adsorption of Pure Water and Ethanol on Surface

System	Heat of Adsorption (kJ/mol)
Pure Water on Surface	52.12
Pure Ethanol on Surface	29.17

The calculated heat of adsorption for water on alumina at 298K (52.12 kJ/mol) is much higher than that obtained for ethanol (29.17 kJ/mol), confirming that the alumina surface effectively attracts water molecules much more strongly than it does ethanol molecules.

B.2.2. Potential of Mean Force – Adsorption on a Freestanding Surface

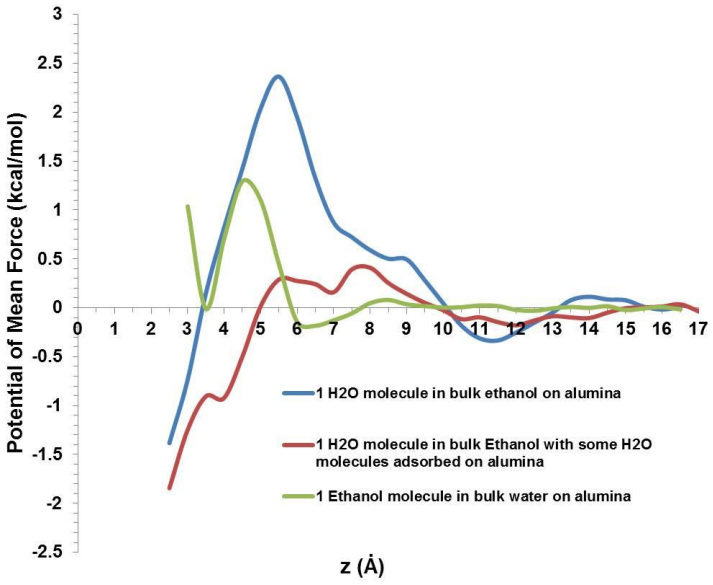

Figure B.1. Simulated potential of mean force as a function of the distance between the center of mass of one water or ethanol molecule and alumina substrate. Results were obtained by umbrella sampling calculations for the system of one water molecule in bulk ethanol (blue curve); one water molecule in bulk ethanol with some water molecules already adsorbed (red curve) and one ethanol molecule in bulk water (green curve) on α-Al_2O_3 (0001) surface.

In Figure B.1, we report the PMF as function of the distance between one molecule and a flat freestanding alumina surface. We considered one water molecule as it approaches the alumina surface covered by ethanol (system A); one water molecule as it approaches the alumina surface covered by ethanol and a few water molecules already adsorbed on alumina (system B), and one ethanol molecule as it approaches the alumina surface covered by water (system C). The PMF results for systems A and C indicate that as the various molecules approach the surface they encounter a relatively large free-energy barrier before they adsorb on the surface. Once they adsorb on the surface, the PMF results show a minimum, which depends on the system. The effective attractive PMF obtained for system A and B is much larger than that obtained for system C. This indicates that water is preferentially

adsorbed on alumina. The large energy barrier encountered for the molecules to adsorb suggests that once water molecules are adsorbed on alumina, they will experience some difficulty to desorb.

B.2.3. Density Profiles in the Pore

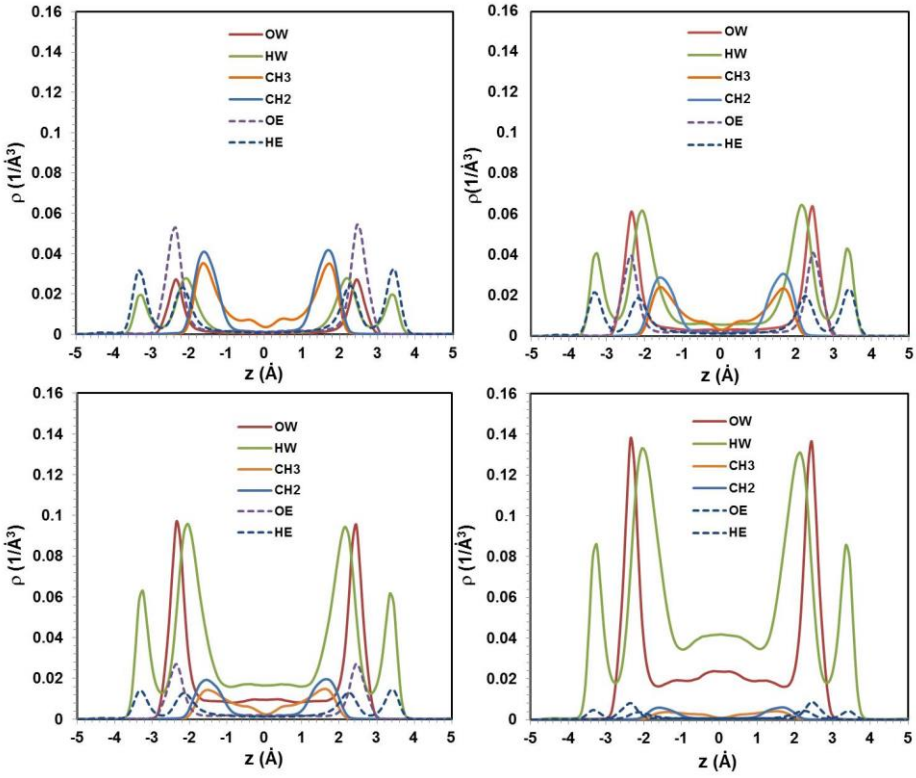

Figure B.2. Density profiles of water oxygen (red solid curve), water hydrogen (green solid curve), methyl ethanol (orange solid curve), methylene ethanol (blue solid curve), oxygen ethanol (purple dash curve) and hydrogen ethanol (dark blue dash curve) as a function of distance z across the alumina pore for simulated systems I (top left), II (top right), III (bottom left), and IV (bottom right). The reference (z = 0) corresponds to the center of the pore.

In Figure B.2, the results of water oxygen (red solid curve), water hydrogen (green solid curve), methyl ethanol (orange solid curve), methylene ethanol (blue solid curve), oxygen ethanol (purple dash curve) and hydrogen ethanol (dark blue dash curve) density profiles as a function of distance z across the alumina pore are shown for simulated systems I (top left), II (top right), III (bottom left), and IV

(bottom right). The reference (z = 0) corresponds to the center of the pore. The density profiles indicate the formation of two well-defined adsorbed layers formed by water and ethanol, respectively, in contact with the pore surfaces. This suggests that few ethanol hydroxyl groups are present near the pore center at all pore compositions considered. The ethanol density profiles suggest that ethanol molecules mostly orient their symmetric axis of methyl groups parallel to the pore surfaces while they project their OH groups toward the surfaces or parallel to it. Water molecules also point their OH groups in the same manner. This preferential orientation allows water and ethanol molecules to form hydrogen bonds with the surface OH groups, as well as between water and ethanol or themselves. The orientation of the symmetric axis of methyl groups in the pore is not consistent with that found in the first layer on the flat freestanding alumina substrate as reported in the previous works [37, 145].

B.2.4. In-plane Radial Distribution Functions

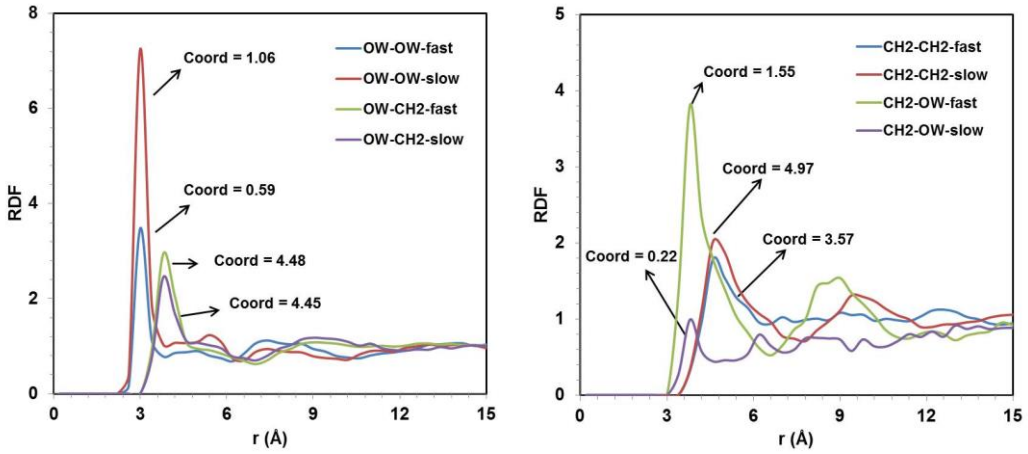

Figure B.3. Left: In-plane water oxygen – water oxygen and water oxygen – methylene group RDFs for the cases of fast and slow movement of the representative water molecule. Right: In-plane methylene – methylene and methylene – water oxygen RDFs for the cases of fast and slow motion of the representative ethanol molecule.

We calculate in-plane RDFs for representative water and ethanol molecules with the surrounding fluid molecules. In the left panel of Figure B.3 we report the results for fast and slow water molecules, while in the right panel of Figure B.3 we consider fast and slow ethanol molecules. We report water oxygen – water oxygen, water oxygen – ethanol methylene RDFs for water and ethanol methylene – methylene, methylene – water oxygen RDFs for ethanol. Our results suggest that slow and fast water and ethanol molecules do not pack differently with respect to neighbouring ethanol molecules. However, regarding neighbouring water molecules, water molecules diffuse fast when surrounded by fewer water molecules, while ethanol molecules diffuse fast when surrounded by many water molecules.

B.2.5. Ethanol Orientation within the Pore for the Cases of Fast and Slow Movement

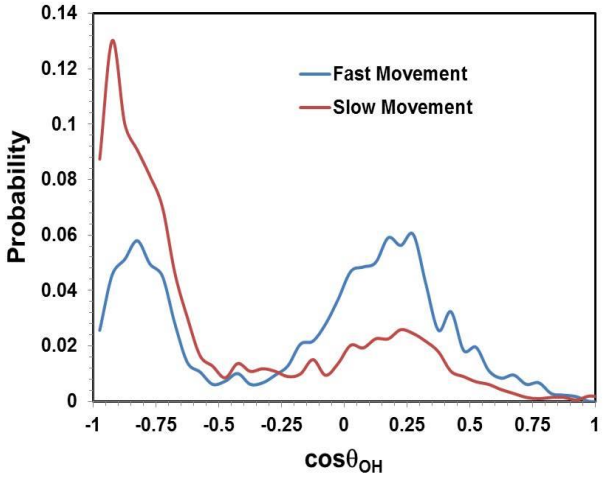

Figure B.4. Probability distribution for θ_{OH} of the representative ethanol molecules within the pore (system I) for the cases of fast (blue curve) and slow (red curve) movement. θ_{OH} is the polar angle of the OH groups with respect to the pore surface normal.

In Figure B.4, we report the probability distribution of polar angles for the OH groups of the representative fast (blue curve) and slow (red curve) ethanol molecule within the pore. The results suggest that ethanol molecules move faster as their OH

groups mostly orient parallel to the surfaces than when their OH groups point toward the surfaces.

B.2.6. Dynamical Properties for Water and Ethanol Molecules in the Bulk Phase

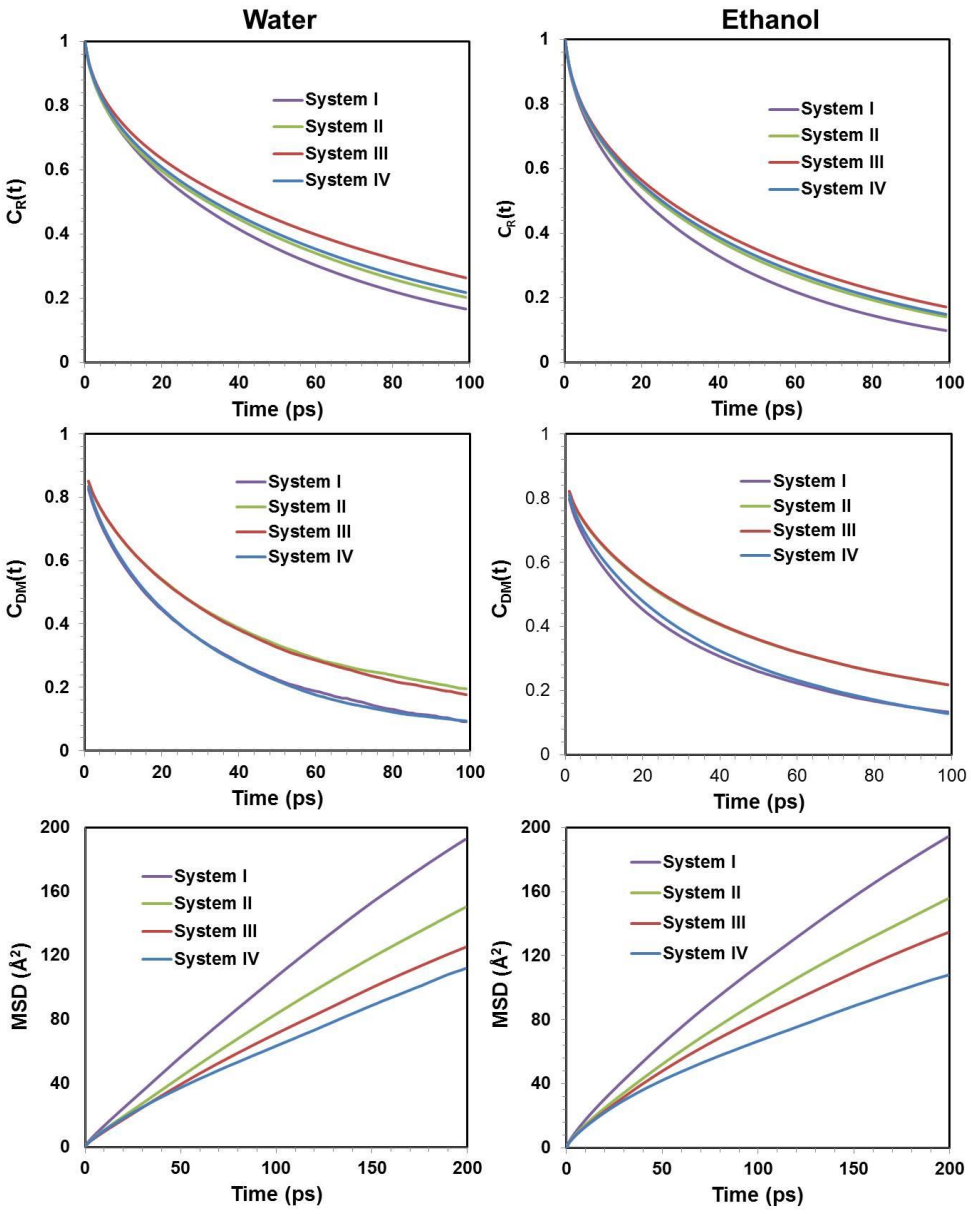

Figure B.5. Top: Residence autocorrelation functions $C_R(t)$ for water (left) and ethanol (right) molecules. Middle: Dipole moment autocorrelation functions for water (top left) and ethanol (top right) molecules. Bottom: 3-D MSD parallel to the alumina pore surfaces for water (left) and ethanol (right) molecules in the bulk phase.

In Figure B.5, the results of the residence autocorrelation function $C_R(t)$ (top), the dipole moment autocorrelation function (middle), and the 3-D MSD (bottom) for water and ethanol molecules outside of the pore, as a function of the fluid composition, are shown. The results for C_R and C_{DM} show strong dependency on composition. Both water and ethanol molecules move more slowly at compositions near the azeotrope. The MSD data suggest that the self-diffusion coefficient of both ethanol and water decreases monotonically with the water mole fraction.

C. Supporting Information for Chapter 6

C.1. Algorithms

C.1.1. Algorithm to Calculate Density Profiles for Confined Methane Molecules in the Direction Perpendicular to the Methane – Water Interface.

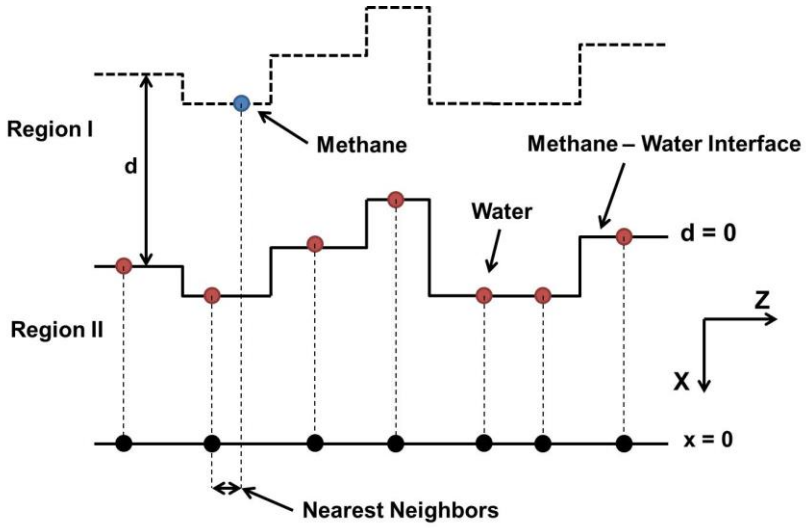

Figure C.1. Schematic diagram describing the algorithm for the calculation of the distance of a methane molecule from a rugged methane – water interface.

Implementing the algorithm proposed Berkowitz et al. [207], we calculated the perpendicular distance ***d*** between one methane molecule in Region I and II and the rough methane – water interface through these steps:

a. The coordinates of the water oxygen atoms at the interface are projected onto the X = 0 plane.
b. The coordinates of the methane molecules are projected onto the X = 0 plane.
c. A methane molecule is associated with the closest water oxygen atom at the interface.
d. The distance ***d*** perpendicular from the rough interface is the distance between the X coordinate of the methane molecule and that of its associated water oxygen atom.

C.1.2. Methane Solubility in Liquid Water

The methane solubility in water in Region I is defined as the ratio of the density of CH_4 molecules in the direction perpendicular to the methane/water interface as Figure 2 (d = ~-29 to ~-15 Å) to the density of water oxygen atoms in the X direction through silica pore, as shown in Figure S2 (x = 15 to 29 Å) . The following equation is used:

$$\boldsymbol{CH_4\ Solubility \times 10^3} = \frac{\left\langle \rho_{CH_4} \right\rangle}{\left\langle \rho_{H_2O} \right\rangle}_{RegionI} \times 10^3 \qquad \text{(C.1)}$$

C.1.3. Pressure Tensor in the Pore

To evaluate the local pressure tensor inside the slit-pore, we calculated the local tangential component of the pressure tensor P_{xx} perpendicular to the methane-water interface. We conducted these calculations in the region ‘deep’ into the pore, far

from both the pore-bulk and methane-water interfaces. The following equation is derived by Walton et al. [242] for an infinite interface in the x-y plane:

$$P_{xx} = P_{T,IK}(z) = \rho(z)k_BT - \frac{1}{4A}\left\langle \sum_{i \neq j} \frac{x_{ij}^2 + y_{ij}^2}{r_{ij}} \frac{1}{|z_{ij}|} \frac{du(r_{ij})}{dr_{ij}} \times \theta\left(\frac{z - z_i}{z_{ij}}\right)\theta\left(\frac{z_j - z}{z_{ij}}\right)\right\rangle \quad \text{(C.2)}$$

In this equation A is the surface area within which averages are computed, $\theta(x)$ is the unit step function, and x_{ij}, y_{ij}, z_{ij} are components of the intermolecular separation vector r_{ij}. We computed the pressure tensor every 0.1 Å along the z-axis of the slit-pore. We point out that Long et al. [217] recently employed this method for calculating the pressure tensor for argon within slit-shaped carbon pores.

C.1.4. Excess Chemical Potential

Initially, we conducted simulations at 300 K for bulk liquid water and liquid water confined in the silica pore without methane to create configurations for the Widom insertion method [204]. In the Widom insertion method, after inserting a methane molecule at a random position in the systems, we calculated $\exp(-\beta\Delta U)$, where ΔU is the potential energy difference between the systems before and after adding a CH_4 molecule, $\Delta U = U(N_{tot} + N_{CH4}) - U(N_{tot})$, with $N_{CH4} = 1$. The excess chemical potential is an average over all the configurations, defined as:

$$\Delta\mu_{ex} = -kT\, ln\frac{\left\langle V \int ds_{N+1}\, exp(-\beta\Delta U)\right\rangle}{\langle V\rangle} \quad \text{(C.3)}$$

In the prior equation k_B is the Boltzmann constant, T is the absolute temperature of the system, $\beta = 1/k_BT$, V is the volume of the system, and $\langle \ldots \rangle$ indicates an ensemble average.

C.1.5. F4 Structural Order Parameter

The F4 structural order parameter developed by Rodger et al. [219] is used to describe the local arrangement of water molecules at different positions during our simulations. The F4 order parameter is based on the H-O…O-H torsion angle, ϕ, for two next-neighbouring water molecules $F_4 = \langle \cos 3\phi \rangle$, where ϕ is the dihedral angle between the vector OH of a given water molecule and the vector OH of another water molecule found within 3.5 Å from the first water molecule [243]. Note that all the water molecules considered for this calculation are found within 5.45 Å from a methane molecule (they belong to the methane hydration shell). The hydrogens considered are the outer-most ones for each water dimer. The distance of 3.5 Å is consistent with the first minimum in the water oxygen – water oxygen radial distribution functions $g_{OO}(r)$ in liquid water [194]. The order parameters were obtained as averaged over all possible angles correlated with a given water, and then over all water molecules in a hydration shell.

C.2. Results

C.2.1. Water Density Profiles in the X direction inside the Pore

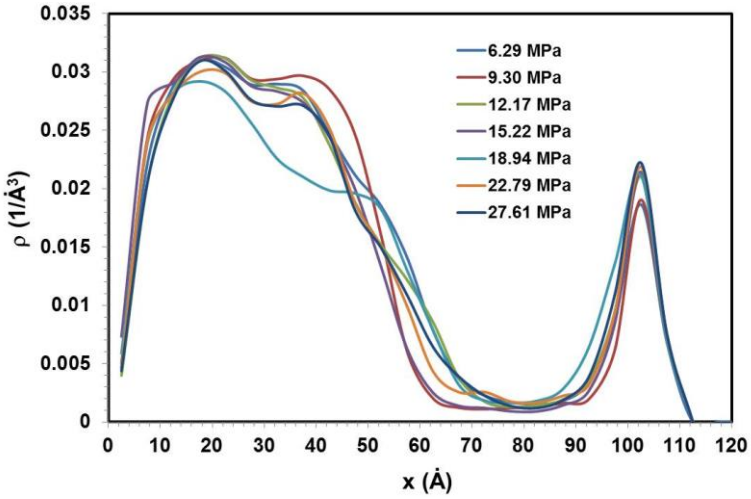

Figure C.2. Density profiles of water oxygen atoms as a function of distance x through the silica pore. The results are obtained from seven simulation systems. The reference (x =0) is the plane located at the position of the pore entrance (left side).

In Figure C.2, we report the results of water oxygen density profiles as a function of distance x through the silica pore when the bulk pressure increases. The reference (x = 0) corresponds to the plane located at the pore entrance (left side). The results in Figure C.2 indicate that generally the increase of the bulk pressure of the system does not impact the structural properties of water molecules.

C.2.2. Pressure Tensor in the Pore

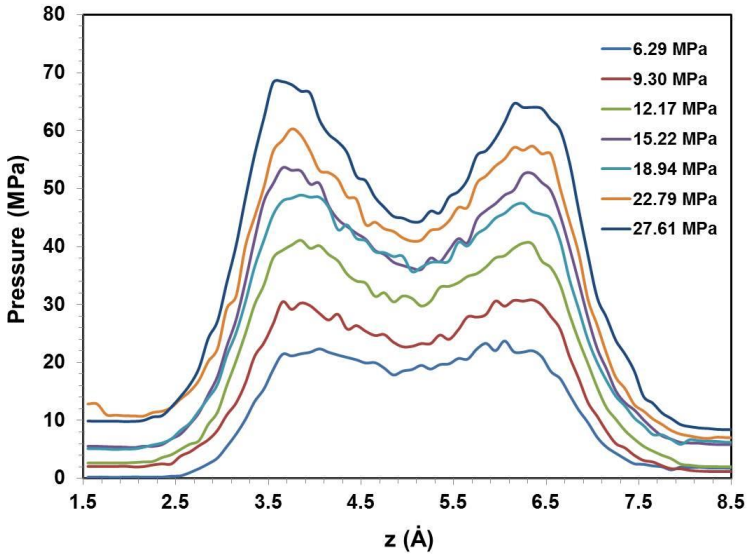

Figure C.3. Tangential pressure tensor profiles for seven methane-water systems confined in the silica pore at 300K.

In Figure C.3, the results for tangential pressure tensor P_{xx} as a function of the distance z across the silica pore are shown for seven simulated systems. Generally, as the bulk pressure increases, the tangential pressure tensor P_{xx} inside the pore also increases. Our results show that, unexpectedly, as the bulk pressure increases from 18.94 to 22.79 MPa, the tangential pressure tensor P_{xx} decreases slightly.

C.2.3. Excess Chemical Potential

In Table C.1 we report the results of the excess chemical potential for methane in bulk liquid water and in confined liquid water. Our calculations in bulk water are in good agreement with literature simulation data [203, 204]. Our data show that the excess free energy for methane in bulk liquid water is higher than that for methane in confined liquid water, which is consistent with higher solubility predicted for methane in confined versus in bulk water.

Table C.1. Excess chemical potential for methane in bulk and confined liquid water at 300K.

System	Excess Chemical Potential (kJ/mol)
CH_4 in Bulk Water	9.31
CH_4 in Water confined in SiO_2 Pore	8.77

Bibliography

1. Argyris D, Cole DR, Striolo A (2010) Ion-Specific Effects under Confinement: The Role of Interfacial Water. *Acs Nano* 4(4):2035-2042.

2. Fornasiero F, Park HG, Holt JK, Stadermann M, Grigoropoulos CP, Noy A, et al. (2008) Ion exclusion by sub-2-nm carbon nanotube pores. *P Natl Acad Sci USA* 105(45):17250-17255.

3. Hille B (2001) *Ion Channels of Excitable Membranes*. Sinauer Asscociates: Sunderland, MA.

4. (2004) *Evaluation of Impacts to Underground Sources of Drinking Water by Hydraulic Fracturing of Coalbed Methane Resevoirs*. Office of Ground Water and Drinking Water, Office of Water.

5. Barnette AL, Asay DB, Janik MJ, Kim SH (2009) Adsorption Isotherm and Orientation of Alcohols on Hydrophilic SiO2 under Ambient Conditions. *J Phys Chem C* 113(24):10632-10641.

6. Anderson RL, Greenwell HC, Suter JL, Jarvis RM, Coveney PV (2010) Towards the design of new and improved drilling fluid additives using molecular dynamics simulations. *Anais Da Academia Brasileira De Ciencias* 82(1):43-60.

7. Greathouse JA, Hart DB, Ochs ME (2012) Alcohol and Thiol Adsorption on (Oxy)hydroxide and Carbon Surfaces: Molecular Dynamics Simulation and Desorption Experiments. *J Phys Chem C* 116(51):26756-26764.

8. Metz S, Anderson RL, Geatches DL, Suter JL, Lines R, Greenwell HC (2015) Understanding the Swelling Behavior of Modified Nanoclay Filler Particles in Water and Ethanol. *J Phys Chem C* 119(22):12625-12642.

9. Jiang YX, Lee A, Chen JY, Cadene M, Chait BT, MacKinnon R (2002) Crystal structure and mechanism of a calcium-gated potassium channel. *Nature* 417(6888):515-522.

10. Ho TA, Argyris D, Cole DR, Striolo A (2012) Aqueous NaCl and CsCl Solutions Confined in Crystalline Slit-Shaped Silica Nanopores of Varying Degree of Protonation. *Langmuir* 28(2):1256-1266.

11. Gates BC (1992) *Catalytic Chemistry*. John Wiley and Sons: New York.

12. Henrich VE, Cox PA (1994) *The Surface Science of Metal Oxides*. Cambridge University Press: Cambridge, UK.

13. Greenland DJ, Hayes MHB (1978) *The Chemistry of Soil Constituents*. John Wiley and Sons: New York.

14. Hochella MF, White AF (1990) *Mineral-Water Interface Geochemistry*. Mineralogical Society of America: Washington DC.

15. Spostio G (1984) *The Surface Chemistry of Soils*. Oxford University Press: Oxford, UK.

16. Stumm W (1992) *Chemistry of the Solid-Water Interface: Processes at the Mineral-Water and Particle-Water Interface in Natural Systems*. John Wiley and Sons: New York.

17. Argyris D, Cole DR, Striolo A (2009) Dynamic Behavior of Interfacial Water at the Silica Surface. *J Phys Chem C* 113(45):19591-19600.

18. Argyris D, Cole DR, Striolo A (2009) Hydration Structure on Crystalline Silica Substrates. *Langmuir* 25(14):8025-8035.

19. Argyris D, Ho TA, Cole DR, Striolo A (2011) Molecular Dynamics Studies of Interfacial Water at the Alumina Surface. *J Phys Chem C* 115(5):2038-2046.

20. Ho TA, Argyris D, Papavassiliou DV, Striolo A, Lee LL, Cole DR (2011) Interfacial water on crystalline silica: a comparative molecular dynamics simulation study. *Mol Simulat* 37(3):172-195.

21. Skelton AA, Fenter P, Kubicki JD, Wesolowski DJ, Cummings PT (2011) Simulations of the Quartz(10(1)over-bar1)/Water Interface: A Comparison of Classical Force Fields, Ab Initio Molecular Dynamics, and X-ray Reflectivity Experiments. *J Phys Chem C* 115(5):2076-2088.

22. Fitter J, Lechner RE, Dencher NA (1999) Interactions of hydration water and biological membranes studied by neutron scattering. *J Phys Chem B* 103(38):8036-8050.

23. Mamontov E, Vlcek L, Wesolowski DJ, Cummings PT, Wang W, Anovitz LM, et al. (2007) Dynamics and structure of hydration water on rutile and cassiterite

nanopowders studied by quasielastic neutron scattering and molecular dynamics simulations. *J Phys Chem C* 111(11):4328-4341.

24. Bruni F, Ricci MA, Soper AK (1998) Water confined in Vycor glass. I. A neutron diffraction study. *J Chem Phys* 109(4):1478-1485.

25. Mamontov E, Wesolowski DJ, Vlcek L, Cummings PT, Rosenqvist J, Wang W, et al. (2008) Dynamics of hydration water on rutile studied by backscattering neutron spectroscopy and molecular dynamics simulation. *J Phys Chem C* 112(32):12334-12341.

26. Malikova N, Cadene A, Marry V, Dubois E, Turq P (2006) Diffusion of water in clays on the microscopic scale: Modeling and experiment. *J Phys Chem B* 110(7):3206-3214.

27. Barnette AL, Asay DB, Kim SH (2008) Average molecular orientations in the adsorbed water layers on silicon oxide in ambient conditions. *Phys Chem Chem Phys* 10(32):4981-4986.

28. Zhang Z, Fenter P, Cheng L, Sturchio NC, Bedzyk MJ, Predota M, et al. (2004) Ion adsorption at the rutile-water interface: Linking molecular and macroscopic properties. *Langmuir* 20(12):4954-4969.

29. Fenn EE, Wong DB, Fayer MD (2009) Water dynamics at neutral and ionic interfaces. *P Natl Acad Sci USA* 106(36):15243-15248.

30. Catalano JG (2011) Weak interfacial water ordering on isostructural hematite and corundum (001) surfaces. *Geochimica Et Cosmochimica Acta* 75(8):2062-2071.

31. Argyris D, Tummala NR, Striolo A, Cole DR (2008) Molecular structure and dynamics in thin water films at the silica and graphite surfaces. *J Phys Chem C* 112(35):13587-13599.

32. Kerisit S, Liu CX, Ilton ES (2008) Molecular dynamics simulations of the orthoclase (001)- and (010)-water interfaces. *Geochimica Et Cosmochimica Acta* 72(6):1481-1497.

33. Giovambattista N, Rossky PJ, Debenedetti PG (2009) Effect of Temperature on the Structure and Phase Behavior of Water Confined by Hydrophobic, Hydrophilic, and Heterogeneous Surfaces. *J Phys Chem B* 113(42):13723-13734.

34. Wang JW, Kalinichev AG, Kirkpatrick RJ (2009) Asymmetric Hydrogen Bonding and Orientational Ordering of Water at Hydrophobic and Hydrophilic Surfaces: A Comparison of Water/Vapor, Water/Talc, and Water/Mica Interfaces. *J Phys Chem C* 113(25):11077-11085.

35. Kalra A, Garde S, Hummer G (2003) Osmotic water transport through carbon nanotube membranes. *P Natl Acad Sci USA* 100(18):10175-10180.

36. Skelton AA, Wesolowski DJ, Cummings PT (2011) Investigating the Quartz (10(1)over-bar0)/Water Interface using Classical and Ab Initio Molecular Dynamics. *Langmuir* 27(14):8700-8709.

37. Sung J, Waychunas GA, Shen YR (2011) Surface-Induced Anisotropic Orientations of Interfacial Ethanol Molecules at Air/Sapphire(1(1)over-bar02) and Ethanol/Sapphire(1(1)over-bar02) Interfaces. *J Phys Chem Lett* 2(14):1831-1835.

38. Enders S, Kahl H (2008) Interfacial properties of water plus alcohol mixtures. *Fluid Phase Equilibr* 263(2):160-167.

39. Atamas AA, Atamas NA, Bulavin LA (2005) Structure correlations of water molecules in a concentrated aqueous solution of ethanol. *Journal of Molecular Liquids* 120(1-3):15-17.

40. Guo JH, Luo Y, Augustsson A, Kashtanov S, Rubensson JE, Shuh DK, et al. (2003) Molecular structure of alcohol-water mixtures. *Phys Rev Lett* 91(15).

41. Scott RPW (2000) The thermodynamic properties of methanol-water association and its effect on solute retention in liquid chromatography. *Analyst* 125(9):1543-1547.

42. Chum HL, Overend RP (2001) Biomass and renewable fuels. *Fuel Process Technol* 71(1-3):187-195.

43. Goldemberg J (2007) Ethanol for a sustainable energy future. *Science* 315(5813):808-810.

44. Treybal RE (1980) *Mass-Transfer Operations*. ed. r, editor. McGraw-Hill Book Co: Singapore.

45. Ivanova E, Damgaliev D, Kostova M (2009) Adsorption separation of ethanol-water liquid mixtures by natural clinoptiloinite. *J Univ Chem Technol Metall* 44:267-274.

46. Kumar S, Singh N, Prasad R (2010) Anhydrous ethanol: A renewable source of energy. *Renewable & Sustainable Energy Reviews* 14(7):1830-1844.

47. Simo M, Sivashanmugam S, Brown CJ, Hlavacek V (2009) Adsorption/Desorption of Water and Ethanol on 3A Zeolite in Near-Adiabatic Fixed Bed. *Ind Eng Chem Res* 48(20):9247-9260.

48. Nomura M, Yamaguchi T, Nakao S (1998) Ethanol/water transport through silicalite membranes. *J Membrane Sci* 144(1-2):161-171.

49. Sano T, Yanagishita H, Kiyozumi Y, Mizukami F, Haraya K (1994) Separation of Ethanol-Water Mixture by Silicalite Membrane on Pervaporation. *J Membrane Sci* 95(3):221-228.

50. Vane LM, Namboodiri VV, Bowen TC (2008) Hydrophobic zeolite-silicone rubber mixed matrix membranes for ethanol-water separation: Effect of zeolite and silicone component selection on pervaporation performance. *J Membrane Sci* 308(1-2):230-241.

51. Chen SH, Yu KC, Lin SS, Chang DJ, Liou RM (2001) Pervaporation separation of water/ethanol mixture by sulfonated polysulfone membrane. *J Membrane Sci* 183(1):29-36.

52. Nguyen QT, Blanc LL, Neel J (1985) Preparation of Membranes from Polyacrylonitrile Polyvinylpyrrolidone Blends and the Study of Their Behavior in the Pervaporation of Water Organic Liquid-Mixtures. *J Membrane Sci* 22(2-3):245-255.

53. Yethiraj A, Striolo A (2013) Fracking: What Can Physical Chemistry Offer? *J Phys Chem Lett* 4(4):687-690.

54. King GE (2012) Hydraulic Fracturing 101: What Every Representative, Environmentalist, Regulator, Reporter, Investor, University Researcher, Neighbor and Engineer Should Know About Estimating Frac Risk and Improving Frac Performance in Unconventional Gas and Oil Wells. SPE Hydraulic Fracturing Technology Conference, February 6-8, The Woodlands, Texas, U.S.A: The Woodlands, Texas, U.S.A, 1-80.

55. Scott HP, Hemley RJ, Mao HK, Herschbach DR, Fried LE, Howard WM, et al. (2004) Generation of methane in the Earth's mantle: In situ high pressure-temperature measurements of carbonate reduction. *P Natl Acad Sci USA* 101(39):14023-14026.

56. Kolesnikov A, Kutcherov VG, Goncharov AF (2009) Methane-derived hydrocarbons produced under upper-mantle conditions. *Nature Geoscience* 2(8):566-570.

57. Liu YY, Wilcox J (2012) Molecular simulation of CO2 adsorption in micro- and mesoporous carbons with surface heterogeneity. *International Journal of Coal Geology* 104:83-95.

58. Liu YY, Wilcox J (2013) Molecular Simulation Studies of CO2 Adsorption by Carbon Model Compounds for Carbon Capture and Sequestration Applications. *Environ Sci Technol* 47(1):95-101.

59. Quar H, Cha SB, Wildeman TR, Sloan ED (1992) The Formation of Natural-Gas Hydrates in Water-Based Drilling-Fluids. *Chemical Engineering Research & Design* 70(1):48-54.

60. Aspenes G, Dieker LE, Aman ZM, Hoiland S, Sum AK, Koh CA, et al. (2010) Adhesion force between cyclopentane hydrates and solid surface materials. *J Colloid Interf Sci* 343(2):529-536.

61. Guggenheim S, van Groos AFK (2003) New gas-hydrate phase: Synthesis and stability of clay-methane hydrate intercalate. *Geology* 31(7):653-656.

62. Uchida T, Ebinuma T, Takeya S, Nagao J, Narita H (2002) Effects of pore sizes on dissociation temperatures and pressures of methane, carbon dioxide, and propane hydrates in porous media. *J Phys Chem B* 106(4):820-826.

63. Meller J-a. (2001) Molecular Dynamics. eLS. John Wiley and Sons: New York, pp.

64. Allen MP, Tildesley DJ (2004) *Computer Simulation of Liquids*. Oxford University Press: Oxford, UK.

65. Cygan RT, Liang JJ, Kalinichev AG (2004) Molecular models of hydroxide, oxyhydroxide, and clay phases and the development of a general force field. *J Phys Chem B* 108(4):1255-1266.

66. Jorgensen WL (1986) Optimized Intermolecular Potential Functions for Liquid Alcohols. *J Phys Chem-Us* 90(7):1276-1284.

67. Berendsen HJC, Grigera JR, Straatsma TP (1987) The Missing Term in Effective Pair Potentials. *J Phys Chem-Us* 91(24):6269-6271.

68. Van der Spoel D, Lindahl E, Hess B, Groenhof G, Mark AE, Berendsen HJC (2005) GROMACS: Fast, flexible, and free. *J Comput Chem* 26(16):1701-1718.

69. Hess B, Bekker H, Berendsen HJC, Fraaije JGEM (1997) LINCS: A linear constraint solver for molecular simulations. *J Comput Chem* 18(12):1463-1472.

70. Miyamoto S, Kollman PA (1992) Settle - an Analytical Version of the Shake and Rattle Algorithm for Rigid Water Models. *J Comput Chem* 13(8):952-962.

71. Kastner J (2011) Umbrella sampling. *Wires Comput Mol Sci* 1(6):932-942.

72. Kumar S, Bouzida D, Swendsen RH, Kollman PA, Rosenberg JM (1992) The Weighted Histogram Analysis Method for Free-Energy Calculations on Biomolecules .1. The Method. *J Comput Chem* 13(8):1011-1021.

73. Souaille M, Roux B (2001) Extension to the weighted histogram analysis method: combining umbrella sampling with free energy calculations. *Comput Phys Commun* 135(1):40-57.

74. Weltoncook MR, Prutton M (1978) Simple Shell-Model Calculation of Differential Ionic Relaxation of Mgo(100) Surface. *Surface Science* 74(1):276-284.

75. Causa M, Dovesi R, Pisani C, Roetti C (1986) Abinitio Hartree-Fock Study of the Mgo(001) Surface. *Surface Science* 175(3):551-560.

76. Martin AJ, Bilz H (1979) Charge Deformation and Geometric Relaxation at the (001) Mgo Surface. *Phys Rev B* 19(12):6593-6600.

77. Urano T, Kanaji T, Kaburagi M (1983) Surface-Structure of Mgo(001) Surface Studied by Leed. *Surface Science* 134(1):109-121.

78. Karolewski MA, Cavell RG (1992) Coadsorption of Cesium and Water on Mgo(100). *Surface Science* 271(1-2):128-138.

79. Knozinger E, Jacob KH, Singh S, Hofmann P (1993) Hydroxyl-Groups as Ir Active Surface Probes on Mgo Crystallites. *Surface Science* 290(3):388-402.

80. Peng XD, Barteau MA (1990) Characterization of Oxide Layers on Mg(0001) and Comparison of H2o Adsorption on Surface and Bulk Oxides. *Surface Science* 233(3):283-292.

81. Peng XD, Barteau MA (1991) Acid-Base Properties of Model Mgo Surfaces. *Langmuir* 7(7):1426-1431.

82. Wu MC, Estrada CA, Corneille JS, Goodman DW (1992) Model Surface Studies of Metal-Oxides - Adsorption of Water and Methanol on Ultrathin Mgo Films on Mo(100). *J Chem Phys* 96(5):3892-3900.

83. Wu MC, Goodman DW (1992) Acid-Base Properties of Mgo Studied by High-Resolution Electron-Energy Loss Spectroscopy. *Catalysis Letters* 15(1-2):1-11.

84. Langel W, Parrinello M (1994) Hydrolysis at Stepped Mgo Surfaces. *Phys Rev Lett* 73(3):504-507.

85. Nada R, Hess AC, Pisani C (1995) Topological Defects at the (001) Surface of Mgo - Energetics and Reactivity. *Surface Science* 336(3):353-361.

86. Picaud S, Hoang PNM, Girardet C (1992) Geometry of (Nh3)N and (H2o)N Aggregates Adsorbed on Well Characterized Mgo(100) and Si(111)-(1x1)H Substrates. *Surface Science* 278(3):339-352.

87. Refson K, Wogelius RA, Eraser DG, Payne MC, Lee MH, Milman V (1995) Water Chemisorption and Reconstruction of the Mgo Surface. *Phys Rev B* 52(15):10823-10826.

88. Scamehorn CA, Hess AC, Mccarthy MI (1993) Correlation Corrected Periodic Hartree-Fock Study of the Interactions between Water and the (001) Magnesium-Oxide Surface. *J Chem Phys* 99(4):2786-2795.

89. Minot C (2004) Water molecule dissociation at ice/MgO(100) interface. *Surface Science* 562(1-3):237-246.

90. McCarthy MI, Schenter GK, Scamehorn CA, Nicholas JB (1996) Structure and dynamics of the water/MgO interface. *J Phys Chem-Us* 100(42):16989-16995.

91. Legg KO, Prutton M, Kinniburgh C (1974) Leed Study of Mgo(100) .1. Experiment. *Journal of Physics C-Solid State Physics* 7(23):4236-4246.

92. Kinniburgh CG (1975) Leed Study of Mgo(100) .2. Theory at Normal Incidence. *Journal of Physics C-Solid State Physics* 8(15):2382-2394.

93. Kinniburgh CG (1976) Leed Study of Mgo(100) .3. Theory at Off-Normal Incidence. *Journal of Physics C-Solid State Physics* 9(14):2695-2708.

94. Essmann U, Perera L, Berkowitz ML, Darden T, Lee H, Pedersen LG (1995) A Smooth Particle Mesh Ewald Method. *J Chem Phys* 103(19):8577-8593.

95. Hoover WG (1985) Canonical Dynamics - Equilibrium Phase-Space Distributions. *Phys Rev A* 31(3):1695-1697.

96. Nose S (1984) A Molecular-Dynamics Method for Simulations in the Canonical Ensemble. *Mol Phys* 52(2):255-268.

97. Hockney RW, Goel SP, Eastwood JW (1974) Quiet High-Resolution Computer Models of a Plasma. *J Comput Phys* 14(2):148-158.

98. Tobbens DM, Stusser N, Knorr K, Mayer HM, Lampert G (2001) E9: The new high-resolution neutron powder diffractometer at the Berlin neutron scattering center. *Epdic 7: European Powder Diffraction, Pts 1 and 2* 378-3:288-293.

99. Jamadagni SN, Godawat R, Garde S (2011) Hydrophobicity of Proteins and Interfaces: Insights from Density Fluctuations. *Annual Review of Chemical and Biomolecular Engineering, Vol 2* 2:147-171.

100. Striolo A (2011) From Interfacial Water to Macroscopic Observables: A Review. *Adsorpt Sci Technol* 29(3):211-258.

101. Gao LC, McCarthy TJ (2008) Teflon is hydrophilic. Comments on definitions of hydrophobic, shear versus tensile hydrophobicity, and wettability characterization. *Langmuir* 24(17):9183-9188.

102. Wang JH, Bratko D, Luzar A (2011) Probing surface tension additivity on chemically heterogeneous surfaces by a molecular approach. *P Natl Acad Sci USA* 108(16):6374-6379.

103. Ho TA, Papavassiliou DV, Lee LL, Striolo A (2011) Liquid water can slip on a hydrophilic surface. *P Natl Acad Sci USA* 108(39):16170-16175.

104. Giovambattista N, Debenedetti PG, Rossky PJ (2007) Effect of surface polarity on water contact angle and interfacial hydration structure. *J Phys Chem B* 111(32):9581-9587.

105. Gonzalez-Martin ML, Labajos-Broncano L, Janczuk B, Bruque JM (1999) Wettability and surface free energy of zirconia ceramics and their constituents. *Journal of Materials Science* 34(23):5923-5926.

106. Marti J (1999) Analysis of the hydrogen bonding and vibrational spectra of supercritical model water by molecular dynamics simulations. *J Chem Phys* 110(14):6876-6886.

107. Wang CL, Lu HJ, Wang ZG, Xiu P, Zhou B, Zuo GH, et al. (2009) Stable Liquid Water Droplet on a Water Monolayer Formed at Room Temperature on Ionic Model Substrates. *Phys Rev Lett* 103(13).

108. Lutzenkirchen J, Zimmermann R, Preocanin T, Filby A, Kupcik T, Kuttner D, et al. (2010) An attempt to explain bimodal behaviour of the sapphire c-plane electrolyte interface. *Adv Colloid Interfac* 157(1-2):61-74.

109. Thomas AC, Richardson HH (2008) Growth of Thin Film Water on alpha-Al2O3 (0001): An FTIR Study. *J Phys Chem C* 112(50):20033-20037.

110. Giovambattista N, Debenedetti PG, Rossky PJ (2009) Enhanced surface hydrophobicity by coupling of surface polarity and topography. *P Natl Acad Sci USA* 106(36):15181-15185.

111. Saiz L, Padro JA, Guardia E (1997) Structure and dynamics of liquid ethanol. *J Phys Chem B* 101(1):78-86.

112. Gao JL, Habibollazadeh D, Shao L (1995) A Polarizable Intermolecular Potential Function for Simulation of Liquid Alcohols. *J Phys Chem-Us* 99(44):16460-16467.

113. Saiz L, Guardia E, Padro JA (2000) Dielectric properties of liquid ethanol. A computer simulation study. *J Chem Phys* 113(7):2814-2822.

114. Wensink EJW, Hoffmann AC, van Maaren PJ, van der Spoel D (2003) Dynamic properties of water/alcohol mixtures studied by computer simulation. *J Chem Phys* 119(14):7308-7317.

115. Noskov SY, Lamoureux G, Roux B (2005) Molecular dynamics study of hydration in ethanol-water mixtures using a polarizable force field. *J Phys Chem B* 109(14):6705-6713.

116. Wang SH, Cann NM (2007) Polarizable and flexible model for ethanol. *J Chem Phys* 126(21).

117. Gonzalez MA, Enciso E, Bermejo FJ, Bee M (1999) Ethanol force fields: A molecular dynamics study of polarization effects on different phases. *J Chem Phys* 110(16):8045-8059.

118. Smith BD, Srivastava R (1986) *Thermodynamic Data for Pure Compounds*. Elsevier: Amsterdam, The Netherlands.

119. Meckl S, Zeidler MD (1988) Self-Diffusion Measurements of Ethanol and Propanol. *Mol Phys* 63(1):85-95.

120. Marti J, Guardia E, Padro JA (1994) Dielectric-Properties and Infrared-Spectra of Liquid Water - Influence of the Dynamic Cross Correlations. *J Chem Phys* 101(12):10883-10891.

121. Svishchev IM, Kusalik PG, Wang J, Boyd RJ (1996) Polarizable point-charge model for water: Results under normal and extreme conditions. *J Chem Phys* 105(11):4742-4750.

122. Lamoureux G, Roux B (2003) Modeling induced polarization with classical Drude oscillators: Theory and molecular dynamics simulation algorithm. *J Chem Phys* 119(6):3025-3039.

123. Rullmann JAC, Vanduijnen PT (1988) A Polarizable Water Model for Calculation of Hydration Energies. *Mol Phys* 63(3):451-475.

124. Rick SW, Stuart SJ, Berne BJ (1994) Dynamical Fluctuating Charge Force-Fields - Application to Liquid Water. *J Chem Phys* 101(7):6141-6156.

125. Andoh Y, Kurahashi K, Sakuma H, Yasuoka K, Kurihara K (2007) Anisotropic molecular clustering in liquid ethanol induced by a charged fully hydroxylated silicon dioxide (SiO2) surface. *Chem Phys Lett* 448(4-6):253-257.

126. Cooke DJ, Gray RJ, Sand KK, Stipp SLS, Elliott JA (2010) Interaction of Ethanol and Water with the {10(1)over-bar4} Surface of Calcite. *Langmuir* 26(18):14520-14529.

127. Rossetto HL, Bowen J, Kendall K (2012) Adhesion of Alumina Surfaces through Confined Water Layers Containing Various Molecules. *Langmuir* 28(10):4648-4653.

128. Coustet V, Jupille J (1994) High-Resolution Electron-Energy-Loss Spectroscopy of Isolated Hydroxyl-Groups on Alpha-Al2o3(0001). *Surface Science* 307:1161-1165.

129. Sung JH, Zhang LN, Tian CS, Waychunas GA, Shen YR (2011) Surface Structure of Protonated R-Sapphire (1(1)over-bar02) Studied by Sum-Frequency Vibrational Spectroscopy. *J Am Chem Soc* 133(11):3846-3853.

130. Trainor TP, Eng PJ, Brown GE, Robinson IK, De Santis M (2002) Crystal truncation rod diffraction study of the alpha-Al2O3 (1(1)over-bar-0 2) surface. *Surface Science* 496(3):238-250.

131. Hess B, Kutzner C, van der Spoel D, Lindahl E (2008) GROMACS 4: Algorithms for highly efficient, load-balanced, and scalable molecular simulation. *J Chem Theory Comput* 4(3):435-447.

132. Mezei M, Beveridge DL (1981) Theoretical-Studies of Hydrogen-Bonding in Liquid Water and Dilute Aqueous-Solutions. *J Chem Phys* 74(1):622-632.

133. Kumar R, Schmidt JR, Skinner JL (2007) Hydrogen bonding definitions and dynamics in liquid water. *J Chem Phys* 126(20).

134. Auer BM, Skinner JL (2009) Water: Hydrogen bonding and vibrational spectroscopy, in the bulk liquid and at the liquid/vapor interface. *Chem Phys Lett* 470(1-3):13-20.

135. Lange NA, Dean JA (1967) *Lange's Handbook of Chemistry*. ed. t, editor. McGraw-Hill: New York.

136. Marrink SJ, Berendsen HJC (1994) Simulation of Water Transport through a Lipid-Membrane. *J Phys Chem-Us* 98(15):4155-4168.

137. Catalano JG, Park C, Zhang Z, Fenter P (2006) Termination and water adsorption at the alpha-Al2O3 (012) - Aqueous solution interface. *Langmuir* 22(10):4668-4673.

138. Catalano JG (2010) Relaxations and Interfacial Water Ordering at the Corundum (110) Surface. *J Phys Chem C* 114(14):6624-6630.

139. Catalano JG, Fenter P, Park C (2007) Interfacial water structure on the (012) surface of hematite: Ordering and reactivity in comparison with corundum. *Geochimica Et Cosmochimica Acta* 71(22):5313-5324.

140. Yang JZ, Liu QL, Wang HT (2007) Analyzing adsorption and diffusion behaviors of ethanol/water through silicalite membranes by molecular simulation. *J Membrane Sci* 291(1-2):1-9.

141. Kuhn J, Castillo-Sanchez JM, Gascon J, Calero S, Dubbeldam D, Vlugt TJH, et al. (2010) Adsorption and Diffusion of Water, Methanol, and Ethanol in All-Silica DD3R: Experiments and Simulations (vol 113C, pg 14290, 2009). *J Phys Chem C* 114(14):6877-6878.

142. Zhang J, Liu W (2011) Thin porous metal sheet-supported NaA zeolite membrane for water/ethanol separation. *J Membrane Sci* 371(1-2):197-210.

143. Mejia SM, Mills MJL, Shaik MS, Mondragon F, Popelier PLA (2011) The dynamic behavior of a liquid ethanol-water mixture: a perspective from quantum chemical topology. *Phys Chem Chem Phys* 13(17):7821-7833.

144. Rao MB, Sircar S (1993) Liquid-phase adsorption of bulk ethanol-water mixtures by alumina. *Adsorpt Sci Technol* 10:93-104.

145. Phan A, Cole DR, Striolo A (2013) Liquid Ethanol Simulated on Crystalline Alpha Alumina. *J Phys Chem B* 117(14):3829-3840.

146. Deboer JH, Lippens BC (1964) Studies on Pore Systems in Catalysts .2. The Shapes of Pores in Aluminum Oxide Systems. *Journal of Catalysis* 3(1):38-43.

147. Wefers K, Misra C. Oxides and Hydroxides of Aluminum. Alcoa Techical Paper 19. 1987:54-58.

148. Pierre AC (1998) *Introduction to Sol-Gel Processing*. Springer: New York.

149. Kittaka S, Yamaguchi K, Takahara S (2012) High physisorption affinity of water molecules to the hydroxylated aluminum oxide (001) surface. *J Colloid Interf Sci* 368:552-557.

150. Matranga KR, Myers AL, Glandt ED (1992) Storage of Natural-Gas by Adsorption on Activated Carbon. *Chem Eng Sci* 47(7):1569-1579.

151. Sircar S, Myers AL, Novosad J (1972) Adsorption from Liquid Mixtures on Solids - Thermodynamics of Excess Properties and Their Temperature Coefficients. *Ind Eng Chem Fund* 11(2):249-&.

152. Yasuhara M, Tatsuki Y, Nakamura M, Vaughn F, inventorsReacting phenols with amination agent in presence of low alkali and weakly acidic alumina catalyst to form desired anilines in high yields and selectivity1996.

153. Myers AL. (2004) Thermodynamics of adsorption. In: Letcher TM, editor. Thermodynamics for Industry. Royal Society of Chemistry: London, pp. 243-253.

154. Auerbach SM, Carrado KA, Dutta PK (2003) *Handbook of Zeolite Science and Technology*. Marcel Dekker, Inc.: New York.

155. Shah D, Kissick K, Ghorpade A, Hannah R, Bhattacharyya D (2000) Pervaporation of alcohol-water and dimethylformamide-water mixtures using hydrophilic zeolite NaA membranes: mechanisms and experimental results. *J Membrane Sci* 179(1-2):185-205.

156. Ho TA, Striolo A (2013) Polarizability effects in molecular dynamics simulations of the graphene-water interface. *J Chem Phys* 138(5).

157. Bermejo JS, Ugarte CM (2008) Influence of water content on structure and mobility of polyvinyl alcohol: A molecular dynamics simulation. *J Chem Phys* 129(15).

158. Easteal AJ, Woolf LA (1985) Pressure and Temperature-Dependence of Tracer Diffusion-Coefficients of Methanol, Ethanol, Acetonitrile, and Formamide in Water. *J Phys Chem-Us* 89(7):1066-1069.

159. Harris KR, Newitt PJ, Derlacki ZJ (1998) Alcohol tracer diffusion, density, NMR and FTIR studies of aqueous ethanol and 2,2,2-trifluoroethanol solutions at 25 degrees C. *Journal of the Chemical Society-Faraday Transactions* 94(14):1963-1970.

160. Price WS, Ide H, Arata Y (2003) Solution dynamics in aqueous monohydric alcohol systems. *J Phys Chem A* 107(24):4784-4789.

161. Sholl DS (2011) Metal-Organic Frameworks: A Porous Maze. *Nat Chem* 3(6):429-430.

162. Hong M, Falconer JL, Noble RD (2005) Modification of zeolite membranes for H-2 separation by catalytic cracking of methyldiethoxysilane. *Ind Eng Chem Res* 44(11):4035-4041.

163. Jackson RB, Vengosh A, Darrah TH, Warner NR, Down A, Poreda RJ, et al. (2013) Increased stray gas abundance in a subset of drinking water wells near Marcellus shale gas extraction. *P Natl Acad Sci USA* 110(28):11250-11255.

164. Berndt C, Feseker T, Treude T, Krastel S, Liebetrau V, Niemann H, et al. (2014) Temporal Constraints on Hydrate-Controlled Methane Seepage off Svalbard. *Science* 343(6168):284-287.

165. Englezos P (1993) Clathrate Hydrates. *Ind Eng Chem Res* 32(7):1251-1274.

166. Collett TS (2002) Energy resource potential of natural gas hydrates. *Aapg Bulletin* 86(11):1971-1992.

167. Brown TD, Taylor CE, Bernardo MP (2010) Rapid Gas Hydrate Formation Processes: Will They Work? *Energies* 3(6):1154-1175.

168. Staykova DK, Kuhs WF, Salamatin AN, Hansen T (2003) Formation of porous gas hydrates from ice powders: Diffraction experiments and multistage model. *J Phys Chem B* 107(37):10299-10311.

169. Buch V, Devlin JP, Monreal IA, Jagoda-Cwiklik B, Uras-Aytemiz N, Cwiklik L (2009) Clathrate hydrates with hydrogen-bonding guests. *Phys Chem Chem Phys* 11(44):10245-10265.

170. Devlin JP, Monreal IA (2010) Instant Conversion of Air to a Clathrate Hydrate: CO2 Hydrates Directly from Moist Air and Moist CO2(g). *J Phys Chem A* 114(50):13129-13133.

171. Davies SR, Lachance JW, Sloan ED, Koh CA (2010) High-Pressure Differential Scanning Calorimetry Measurements of the Mass Transfer Resistance

across a Methane Hydrate Film as a Function of Time and Subcooling. *Ind Eng Chem Res* 49(23):12319-12326.

172. Bauer M, Tobbens DM, Mayer E, Loerting T (2011) Pressure-amorphized cubic structure II clathrate hydrate: crystallization in slow motion. *Phys Chem Chem Phys* 13(6):2167-2171.

173. Chialvo AA, Houssa M, Cummings PT (2002) Molecular dynamics study of the structure and thermophysical properties of model sI clathrate hydrates. *J Phys Chem B* 106(2):442-451.

174. Yezdimer EM, Cummings PT, Chialvo AA (2002) Determination of the Gibbs free energy of gas replacement in SI clathrate hydrates by molecular simulation. *J Phys Chem A* 106(34):7982-7987.

175. Moon C, Taylor PC, Rodger PM (2003) Molecular dynamics study of gas hydrate formation. *J Am Chem Soc* 125(16):4706-4707.

176. Vatamanu J, Kusalik PG (2006) Unusual crystalline and polycrystalline structures in methane hydrates. *J Am Chem Soc* 128(49):15588-15589.

177. Liang S, Kusalik PG (2011) The Mobility of Water Molecules through Gas Hydrates. *J Am Chem Soc* 133(6):1870-1876.

178. Walsh MR, Koh CA, Sloan ED, Sum AK, Wu DT (2009) Microsecond Simulations of Spontaneous Methane Hydrate Nucleation and Growth. *Science* 326(5956):1095-1098.

179. Jacobson LC, Hujo W, Molinero V (2010) Amorphous Precursors in the Nucleation of Clathrate Hydrates. *J Am Chem Soc* 132(33):11806-11811.

180. Jacobson LC, Molinero V (2011) Can Amorphous Nuclei Grow Crystalline Clathrates? The Size and Crystallinity of Critical Clathrate Nuclei. *J Am Chem Soc* 133(16):6458-6463.

181. Tung YT, Chen LJ, Chen YP, Lin ST (2010) The Growth of Structure I Methane Hydrate from Molecular Dynamics Simulations. *J Phys Chem B* 114(33):10804-10813.

182. Hawtin RW, Quigley D, Rodger PM (2008) Gas hydrate nucleation and cage formation at a water/methane interface. *Phys Chem Chem Phys* 10(32):4853-4864.

183. Sarupria S, Debenedetti PG (2012) Homogeneous Nucleation of Methane Hydrate in Microsecond Molecular Dynamics Simulations. *J Phys Chem Lett* 3(20):2942-2947.

184. Jacobson LC, Hujo W, Molinero V (2010) Nucleation Pathways of Clathrate Hydrates: Effect of Guest Size and Solubility. *J Phys Chem B* 114(43):13796-13807.

185. Vatamanu J, Kusalik PG (2010) Observation of two-step nucleation in methane hydrates. *Phys Chem Chem Phys* 12(45):15065-15072.

186. Liang S, Kusalik PG (2013) Nucleation of Gas Hydrates within Constant Energy Systems. *J Phys Chem B* 117(5):1403-1410.

187. Guo GJ, Rodger PM (2013) Solubility of Aqueous Methane under Metastable Conditions: Implications for Gas Hydrate Nucleation. *J Phys Chem B* 117(21):6498-6504.

188. Park SH, Sposito G (2003) Do montmorillonite surfaces promote methane hydrate formation? Monte Carlo and molecular dynamics simulations. *J Phys Chem B* 107(10):2281-2290.

189. Cygan RT, Guggenheim S, van Groos AFK (2004) Molecular models for the intercalation of methane hydrate complexes in montmorillonite clay. *J Phys Chem B* 108(39):15141-15149.

190. Botan A, Rotenberg B, Marry V, Turq P, Noetinger B (2010) Carbon Dioxide in Montmorillonite Clay Hydrates: Thermodynamics, Structure, and Transport from Molecular Simulation. *J Phys Chem C* 114(35):14962-14969.

191. Bai DS, Chen GJ, Zhang XR, Wang WC (2011) Microsecond Molecular Dynamics Simulations of the Kinetic Pathways of Gas Hydrate Formation from Solid Surfaces. *Langmuir* 27(10):5961-5967.

192. Bai DS, Chen GJ, Zhang XR, Wang WC (2012) Nucleation of the CO2 Hydrate from Three-Phase Contact Lines. *Langmuir* 28(20):7730-7736.

193. Liang S, Rozmanov D, Kusalik PG (2011) Crystal growth simulations of methane hydrates in the presence of silica surfaces. *Phys Chem Chem Phys* 13(44):19856-19864.

194. Bagherzadeh SA, Englezos P, Alavi S, Ripmeester JA (2012) Influence of Hydrated Silica Surfaces on Interfacial Water in the Presence of Clathrate Hydrate Forming Gases. *J Phys Chem C* 116(47):24907-24915.

195. Riedel M, Collett T, Malone MJ, Scientists IE (2009) Gas hydrate drilling transect across northern Cascadia margin - IODP Expedition 311. *Sediment-Hosted Gas Hydrates: New Insights on Natural and Synthetic Systems* 319:11-19.

196. Kalluri RK, Konatham D, Striolo A (2011) Aqueous NaCl Solutions within Charged Carbon-Slit Pores: Partition Coefficients and Density Distributions from Molecular Dynamics Simulations. *J Phys Chem C* 115(28):13786-13795.

197. Golebiowska M, Roth M, Firlej L, Kuchta B, Wexler C (2012) The reversibility of the adsorption of methane-methyl mercaptan mixtures in nanoporous carbon. *Carbon* 50(1):225-234.

198. Worthington PF (2010) Petrophysical evaluation of gas-hydrate formations. *Petroleum Geoscience* 16(1):53-66.

199. Paschek D (2004) Temperature dependence of the hydrophobic hydration and interaction of simple solutes: An examination of five popular water models. *J Chem Phys* 120(14):6674-6690.

200. Docherty H, Galindo A, Vega C, Sanz E (2006) A potential model for methane in water describing correctly the solubility of the gas and the properties of the methane hydrate. *J Chem Phys* 125(7).

201. Prini RF, Crovetto R (1989) Evaluation of Data on Solubility of Simple Apolar Gases in Light and Heavy-Water at High-Temperature. *Journal of Physical and Chemical Reference Data* 18(3):1231-1243.

202. Wagner W, Pruss A (2002) The IAPWS formulation 1995 for the thermodynamic properties of ordinary water substance for general and scientific use. *Journal of Physical and Chemical Reference Data* 31(2):387-535.

203. Konrad O, Lankau T (2005) Solubility of methane in water: The significance of the methane-water interaction potential. *J Phys Chem B* 109(49):23596-23604.

204. Lee J, Aluru NR (2013) Water-solubility-driven separation of gases using graphene membrane. *J Membrane Sci* 428:546-553.

205. Kanatani K (2010) Interfacial instability induced by lateral vapor pressure fluctuation in bounded thin liquid-vapor layers. *Physics of Fluids* 22(1).

206. Koga T, Wong J, Endoh MK, Mahajan D, Gutt C, Satija SK (2010) Hydrate Formation at the Methane/Water Interface on the Molecular Scale. *Langmuir* 26(7):4627-4630.

207. Pandit SA, Bostick D, Berkowitz ML (2003) An algorithm to describe molecular scale rugged surfaces and its application to the study of a water/lipid bilayer interface. *J Chem Phys* 119(4):2199-2205.

208. Mosher K, He JJ, Liu YY, Rupp E, Wilcox J (2013) Molecular simulation of methane adsorption in micro- and mesoporous carbons with applications to coal and gas shale systems. *International Journal of Coal Geology* 109:36-44.

209. Cole DR, Ok S, Striolo A, Anh P (2013) Hydrocarbon Behavior at Nanoscale Interfaces. *Carbon in Earth* 75:495-545.

210. Sakamaki R, Sum AK, Narumi T, Ohmura R, Yasuoka K (2011) Thermodynamic properties of methane/water interface predicted by molecular dynamics simulations. *J Chem Phys* 134(14).

211. Culberson OL, Mcketta JJ (1951) Phase Equilibria in Hydrocarbon-Water Systems .3. The Solubility of Methane in Water at Pressures to 10,000 Psia. *Transactions of the American Institute of Mining and Metallurgical Engineers* 192:223-226.

212. Chapoy A, Mohammadi AH, Richon D, Tohidi B (2004) Gas solubility measurement and modeling for methane-water and methane-ethane-n-butane-water systems at low temperature conditions. *Fluid Phase Equilibr* 220(1):113-121.

213. Yang SO, Cho SH, Lee H, Lee CS (2001) Measurement and prediction of phase equilibria for water plus methane in hydrate forming conditions. *Fluid Phase Equilibr* 185(1-2):53-63.

214. Luzar A, Bratko D (2005) Gas solubility in hydrophobic confinement. *J Phys Chem B* 109(47):22545-22552.

215. Miachon S, Syakaev VV, Rakhmatullin A, Pera-Titus M, Caldarelli S, Dalmon JA (2008) Higher gas solubility in nanoliquids? *Chemphyschem* 9(1):78-82.

216. Diaz Campos M, Akkutlu IY, Sigal RF (2009) A Molecular Dynamics Study on Natural Gas Solubility Enhancement in Water Confined to Small Pores SPE Annual Technical Conference and Exhibition, Oct 4-7, New Orleans, LA. Society of Petroleum Engineers: New Orleans, LA.

217. Long Y, Palmer JC, Coasne B, Sliwinska-Bartkowiak M, Gubbins KE (2011) Pressure enhancement in carbon nanopores: a major confinement effect. *Phys Chem Chem Phys* 13(38):17163-17170.

218. Guo GJ, Li M, Zhang YG, Wu CH (2009) Why can water cages adsorb aqueous methane? A potential of mean force calculation on hydrate nucleation mechanisms. *Phys Chem Chem Phys* 11(44):10427-10437.

219. Rodger PM, Forester TR, Smith W (1996) Simulations of the methane hydrate methane gas interface near hydrate forming conditions. *Fluid Phase Equilibr* 116(1-2):326-332.

220. Guo GJ (2011) Cage Adsorption Hypothesis on Hydrate Nucleation Mechanisms Proceedings of the 7th International Conference on Gas Hydrate (ICGH 2011), Jan 17-21, Edinburgh, Scotland, UK: Edinburgh, Scotland, UK.

221. Phan A, Cole DR, Striolo A (2014) Aqueous Methane in Slit-Shaped Silica Nanopores: High Solubility and Traces of Hydrates. *J Phys Chem C* 118(9):4860-4868.

222. Godawat R, Jamadagni SN, Garde S (2009) Characterizing hydrophobicity of interfaces by using cavity formation, solute binding, and water correlations. *P Natl Acad Sci USA* 106(36):15119-15124.

223. Limmer DT, Willard AP, Madden P, Chandler D (2013) Hydration of metal surfaces can be dynamically heterogeneous and hydrophobic. *P Natl Acad Sci USA* 110(11):4200-4205.

224. Phan A, Cole DR, Striolo A (2014) Preferential Adsorption from Liquid Water-Ethanol Mixtures in Alumina Pores. *Langmuir* 30(27):8066-8077.

225. Phan A, Ho TA, Cole DR, Striolo A (2012) Molecular Structure and Dynamics in Thin Water Films at Metal Oxide Surfaces: Magnesium, Aluminum, and Silicon Oxide Surfaces. *J Phys Chem C* 116(30):15962-15973.

226. Huang LP, Durandurdu M, Kieffer J (2006) Transformation pathways of silica under high pressure. *Nat Mater* 5(12):977-981.

227. Tsuchida Y, Yagi T (1990) New Pressure-Induced Transformations of Silica at Room-Temperature. *Nature* 347(6290):267-269.

228. Coppari F, Smith RF, Eggert JH, Wang J, Rygg JR, Lazicki A, et al. (2013) Experimental evidence for a phase transition in magnesium oxide at exoplanet pressures. *Nature Geoscience* 6(11):926-929.

229. Duffy TS, Hemley RJ, Mao HK (1995) Equation of State and Shear-Strength at Multimegabar Pressures - Magnesium-Oxide to 227gpa. *Phys Rev Lett* 74(8):1371-1374.

230. Jephcoat AP, Hemley RJ, Mao HK (1988) X-Ray-Diffraction of Ruby (Al2o3-Cr3+) to 175 Gpa. *Physica B & C* 150(1-2):115-121.

231. Funamori N, Jeanloz R (1997) High-pressure transformation of Al2O3. *Science* 278(5340):1109-1111.

232. Lin JF, Degtyareva O, Prewitt CT, Dera P, Sata N, Gregoryanz E, et al. (2004) Crystal structure of a high-pressure/high-temperature phase of alumina by in situ X-ray diffraction. *Nat Mater* 3(6):389-393.

233. Thomson KT, Wentzcovitch RM, Bukowinski MST (1996) Polymorphs of alumina predicted by first principles: Putting pressure on the ruby pressure scale. *Science* 274(5294):1880-1882.

234. Setny P, Baron R, Kekenes-Huskey PM, McCammon JA, Dzubiella J (2013) Solvent fluctuations in hydrophobic cavity-ligand binding kinetics. *P Natl Acad Sci USA* 110(4):1197-1202.

235. Woolf TB, Roux B (1994) Conformational Flexibility of O-Phosphorylcholine and O-Phosphorylethanolamine - a Molecular-Dynamics Study of Solvation Effects. *J Am Chem Soc* 116(13):5916-5926.

236. Hummer G (2005) Position-dependent diffusion coefficients and free energies from Bayesian analysis of equilibrium and replica molecular dynamics simulations. *New J Phys* 7.

237. Witherspoon PA, Saraf DN (1965) Diffusion of Methane Ethane Propane and N-Butane in Water from 25 to 43 Degrees. *J Phys Chem-Us* 69(11):3752-3755.

238. Smit B, Siepmann JI (1994) Computer-Simulations of the Energetics and Siting of N-Alkanes in Zeolites. *J Phys Chem-Us* 98(34):8442-8452.

239. Woods GB, Panagiotopoulos AZ, Rowlinson JS (1988) Adsorption of Fluids in Model Zeolite Cavities. *Mol Phys* 63(1):49-63.

240. Torrie GM, Valleau JP (1974) Monte-Carlo Free-Energy Estimates Using Non-Boltzmann Sampling - Application to Subcritical Lennard-Jones Fluid. *Chem Phys Lett* 28(4):578-581.

241. Argyris D, Phan A, Striolo A, Ashby PD (2013) Hydration Structure at the alpha-Al2O3 (0001) Surface: Insights from Experimental Atomic Force Spectroscopic Data and Atomistic Molecular Dynamics Simulations. *J Phys Chem C* 117(20):10433-10444.

242. Walton JPRB, Tildesley DJ, Rowlinson JS, Henderson JR (1983) The Pressure Tensor at the Planar Surface of a Liquid. *Mol Phys* 48(6):1357-1368.

243. Liang S, Kusalik PG (2011) Exploring nucleation of H2S hydrates. *Chem Sci* 2(7):1286-1292.